

**VOID EVOLUTION AND DEFECT INTERACTIONS IN
SILICON AND SILICON GERMANIUM**

VOID EVOLUTION AND DEFECT INTERACTIONS IN
SILICON AND SILICON GERMANIUM

By

MOHAMMAD HASANUZZAMAN, B.Sc., M.Sc., M.A.Sc.

A Thesis
Submitted to the School of Graduate Studies
in Partial Fulfillment of the Requirements for the Degree
Doctor of Philosophy

McMaster University © Copyright by Mohammad Hasanuzzaman,
April 2012

DOCTOR OF PHILOSOPHY (2012)
(Electrical and Computer Engineering)

McMASTER UNIVERSITY
Hamilton, Ontario, Canada

TITLE: Void Evolution and Defect Interactions in Silicon and Silicon Germanium

AUTHOR: Mohammad Hasanuzzaman, B.Sc., M.Sc. (Bangladesh University of Engineering and Technology, Dhaka, Bangladesh), M.A.Sc. (McMaster University)

SUPERVISOR: Dr. Yaser M. Haddara

CO-SUPERVISOR Dr. Andrew P. Knights

NUMBER OF PAGES: xvii, 158

ABSTRACT

We propose a physically based model that describes the density and size of voids in silicon introduced via high dose helium ion implantation and subsequent annealing. The model takes into account interactions between vacancies, interstitials, small vacancy clusters, and voids. Void evolution in silicon occurs mainly by a migration and coalescence process. Various factors such as implantation energy and dose, anneal temperature, atmospheric pressure, and impurity level in silicon can influence the migration and coalescence mechanism and thus play a role in the void evolution process. Values for model parameters are consistent with known values for point defect parameters and assumed diffusion limited reaction rates. A single “fitting parameter” represents the rate of bubble migration and coalescence and is therefore related to surface diffusion of adatoms. Results obtained from simulations based upon the model were compared to our experimental results and to previously reported experimental results obtained over a wide range of conditions.

Our own experiments involved the implantation of silicon samples and samples with a thin $\text{Si}_{1-x}\text{Ge}_x$ ($x = 0.05, 0.09$) epilayer on silicon with 30 keV, $5 \times 10^{16} \text{ cm}^{-2}$ helium. Anneals were done in the range 960-1110°C for 15-30 minutes in nitrogen and dry oxygen. Void size distributions were measured from transmission electron microscopy images. Average void diameter and void density values and void size distribution did not show any significant differences between the samples annealed in nitrogen and dry oxygen. However, the presence of $\text{Si}_{1-x}\text{Ge}_x$ epilayer on silicon resulted in increased

average void diameter and reduced average void density when compared with Si samples as well as more selective void size distribution.

Data from the literature included experiments with helium ion implantation energies in the range 30 - 300 keV, doses of 1×10^{16} - 1×10^{17} cm⁻², subsequent annealing temperatures in the range 700 - 1200°C, and annealing duration in the range 15 minutes - 2 hours. Excellent agreement is found between the simulated results and those from reported experiments. The extracted migration and coalescence rate parameter shows an activation energy consistent with surface diffusivity of silicon. It shows a linear dependence on helium dose, and increases with decreased implantation energy, decreased ambient pressure, decreased substrate impurities, increased temperature ramp rate, or increased Ge fraction in cavity layer, all consistent with the proposed physical mechanism. Our mathematical model specifically ignores the long time saturation in void size, although we propose a simple explanation consistent with the physical picture. Similarly, we give physical reasons for a threshold implant dose resulting in the formation of small vacancy clusters during implant. But in modeling void growth we simply show that when such clusters exist voids will evolve according to our model.

In our experiments, the presence of a Si_{0.95}Ge_{0.05} epilayer on silicon resulted in retarded B diffusion when compared with Si samples. This phenomenon is correlated to the role of the Si_{0.95}Ge_{0.05} epilayer on silicon in the void evolution mechanism and both are attributed to Ge interdiffusing from the epilayer into the Si bulk. The B diffusion data also allows us to predict conditions for the SiGe epilayer to modify the injection of interstitials from surface during dry oxidizing anneal.

ACKNOWLEDGEMENT

I would like to extend my sincere gratitude to my supervisors Dr. Yaser M. Haddara and Dr. Andrew P. Knights for giving the opportunity to work with them. Their support, suggestion and cooperation made it possible to finish this work. I would like to thank my PhD supervisory committee members Dr. Rafael N. Kleiman and Dr. Shiva Kumar for their comments and thoughtful suggestions during the progress of the work. I would like to extend my gratitude to Dr. Ian V. Mitchell for giving his valuable time as an external examiner and providing thoughtful comments.

I would like to thank the staffs of the Canadian Centre for Electron Microscope (CCEM) for giving me the opportunity to extensively use the facility. I am grateful to Mr. Fred Pearson who shared his valuable time to train me to prepare transmission electron microscopy (TEM) samples and to train me to operate electron microscope. Despite his busy schedule, Fred was always welcoming to clarify any questions I had related to TEM sample preparation or operating the electron microscope. Thanks are also due to Ms. Julia Huang who also helped me in providing training on TEM sample preparation during my initial days of working at CCEM. Valuable suggestions from Mr. W. N. Gong at the TEM sample preparation laboratory also helped to fast track the TEM sample preparation process. I am also grateful to Dr. Carmen Andrei for her help in doing the electron energy loss spectroscopy measurements and energy dispersive x-ray analysis on my samples.

I would also like to extend my thanks to Ms. Doris V. Stevanovic and Mr. Graham Pearson at the Centre for Emerging Device Technologies (CEDT) at McMaster University for providing me several safety trainings and providing trainings on operating

different tools those I needed to carry out my research work. Thanks are also due to Mr. Cosmin Coroiu and Mr. Terry Greenlay for providing solutions on computing related issues. Thanks to Ms. Cheryl Gies, the Graduate Administrative Assistant of the Department of Electrical and Electronic Engineering at McMaster University for her continuous support and encouragement to finish the work.

I would like to extend my thanks to all of my friends and relatives who continuously encouraged me during the course of this long journey. I am immensely indebted to my wife Farhana Rahman Khan for her endless support and encouragement, without which it could become very difficult to finish this work. She almost single handedly took care of our daughter Zahia Tazmeen Zaman, who was born while I was busy with my research works.

Finally I would like to extend my sincere gratitude to my parents Dr. A.F.M. Akhtaruzzaman and Mrs. Hasina Zaman and to my sister Ms. Afreen Zaman for their unconditional love and support in my entire life and for extending their continuous encouragement in finishing up this work.

LIST OF CONTENTS

LIST OF FIGURES	ix
LIST OF TABLES.....	xiii
LIST OF COMMON ABBREVIATIONS AND SYMBOLS	xiv
Chapter 1	1
Introduction	1
1.1 Background.....	1
1.1.1 Material Properties of $\text{Si}_{1-x}\text{Ge}_x$	3
1.2 Motivation Behind the Study.....	8
1.3 Process Simulator: FLOOPS-ISE	10
1.4 Organization of the Thesis	12
Chapter 2	14
Point Defects and Dopant Diffusion Mechanisms	14
2.1 Point Defects.....	15
2.2 Dopant Diffusion Mechanisms	17
2.3 The Ion Implantation Process and Transient Enhanced Diffusion of Dopants	20
2.4 Point Defect Injection and Effect on Dopant Diffusion Process	25
Chapter 3	28
Factors Influencing Void Formation in Silicon by Helium Implantation.....	28
3.1 Void Formation Mechanism.....	29
3.2 Role of He^+ Implantation Dose.....	31
3.2.1 Why Voids Grow Above “Critical Dose”?.....	34
3.3 Which Process Dominates: Migration and Coalescence or Ostwald Ripening?	40
3.4 keV versus MeV Implantation Energy.....	44
3.5 Role of Implantation Temperature.....	46
3.6 Effect of Pressure	50
3.7 Effect of Anneal Ramp Rate.....	51
3.8 Cavity Formation by Hydrogen Implantation	51
Chapter 4	53
Void Formation in Si and $\text{Si}_{1-x}\text{Ge}_x/\text{Si}$ by He^+ Implantation.....	53
4.1 Experimental Details	53
4.2 Experimental Results and Discussions.....	56

Chapter 5	73
A Mathematical Model for Void Evolution in Silicon	73
5.1 Previous Attempts.....	73
5.2 Cavity Migration and Coalescence Process	76
5.3 Helium Effusion Kinetics.....	77
5.4 Mathematical Model	83
5.5 Simulation Approach, Results and Discussions	88
5.5.1 Experimental Results.....	88
5.5.2 Initial Conditions.....	89
5.5.3 Model Parameters.....	91
5.5.4 Simulation Results	93
Chapter 6	107
Boron Diffusion in Si and Si_{0.95}Ge_{0.05} - capped Si and Correlation with Void Evolution	107
6.1 Background.....	108
6.2 Experimental Details and Discussions	114
Chapter 7	126
Conclusions	126
7.1 Contributions	126
7.2 Suggestions for Future Work.....	128
References	131
Appendix A	146
A.1 Statistical parameters.....	146
A.2 Hypothesis Test for Comparing Mean Values of Two Data Sets.....	148
A.2.1 Application to Experimental Results in Chapter 4.....	149
Appendix B	151
B.1 FLOOPS-ISE Simulation Code for Void Modeling	151

LIST OF FIGURES

Figure 1.1. The top $\text{Si}_{1-x}\text{Ge}_x$ layer is grown on Si substrate. $\text{Si}_{1-x}\text{Ge}_x$ layer is under compressive strain [6].	5
Figure 1.2. The top Si layer is grown on $\text{Si}_{1-x}\text{Ge}_x$ substrate. Si layer is under tensile strain [6].	5
Figure 1.3. Critical thickness as a function of Ge fraction in $\text{Si}_{1-x}\text{Ge}_x$, where $\text{Si}_{1-x}\text{Ge}_x$ layers are grown on bulk (100) Si [6].	6
Figure 2.1. Different types of point defects. (1) self-interstitial, (2) vacancy, (3) di-vacancy, (4) interstitial impurity, (5) substitutional impurity, (6) substitutional impurity vacancy complex [42].	16
Figure 2.2. Vacancy exchange mechanism. ● represents a host atom or a dopant atom that diffuses by the vacancy exchange mechanism [43].	17
Figure 2.3. Kick-out mechanism. ● represents an atom initially at substitutional site, which later becomes interstitial atom and diffuses through the lattice [43].	18
Figure 2.4. Interstitialcy diffusion mechanism. ● represents a dopant atom and ○ represents a Si atom [44].	19
Figure 2.5. Recombination mechanism. ● represents a host or a dopant atom. [43].	19
Figure 3.1. TDS spectrum of He for different He^+ implantation doses [115].	37
Figure 3.2. Ostwald ripening mechanism.	41
Figure 3.3. Migration and coalescence mechanism.	41
Figure 4.1. XTEM image of as-implanted Si sample implanted with 30 keV, $5 \times 10^{16} \text{ cm}^{-2}$ He^+ . Images taken with JEOL 2010 electron microscope operating at 200 kV.	56
Figure 4.2. XTEM images for Si samples annealed in RTA at 1050°C for 15 min in (a) N_2 and (b) dry O_2 .	58

Figure 4.3. XTEM images for Si _{0.95} Ge _{0.05} /Si samples annealed in RTA at 1050°C for 15 min in (a) N ₂ and (b) dry O ₂	59
Figure 4.4. XTEM images for Si samples annealed in FA at 1080°C for 30 min in (a) N ₂ and (b) dry O ₂	60
Figure 4.5. XTEM images for Si _{0.95} Ge _{0.05} /Si samples annealed in FA at 1080°C for 30 min in (a) N ₂ and (b) dry O ₂	61
Figure 4.6. XTEM image showing dislocation associated with a void. Image taken with JEOL 2010 electron microscope operating at 200 kV.....	62
Figure 4.7. Variation of average void diameter and average void density in Si and Si _{1-x} Ge _x /Si (x = 0.05, 0.09) samples as a function of annealing temperature. Solid lines through the data point act as guide to the eyes.	64
Figure 4.8. Ge interdiffusion after annealing for 30 min at 1050°C taking into account the damage created during 30 keV, 5 × 10 ¹⁶ cm ⁻² He ⁺ implantation.	67
Figure 4.9. Void size distribution for annealing done in RTA at 1050°C for 15 min. Si samples annealed in (a) N ₂ and (b) dry O ₂ . Si _{0.95} Ge _{0.05} /Si samples annealed in (c) N ₂ and (d) dry O ₂	69
Figure 4.10. Void size distribution for annealing done in FA at 1080°C for 30 min. Si samples annealed in (a) N ₂ and (b) dry O ₂ . Si _{0.95} Ge _{0.05} /Si samples annealed in (c) N ₂ and (d) dry O ₂	70
Figure 5.1. Schematic representation of cavity migration by (1) surface diffusion, (2) volume diffusion, and (3) vapour transport [155]......	76
Figure 5.2. (a) void diameter and (b) void density as a function of anneal temperature for our experiments. Samples were implanted with 30 keV, 5 × 10 ¹⁶ cm ⁻² He ⁺ . Symbols refer to experimental data, lines refer to simulation.	94
Figure 5.3. (a) void diameter and (b) void density as a function of anneal temperature. Si samples were implanted with different doses of He ⁺ at 40 keV. Experimental data were reported by Raineri <i>et al.</i> [99]. Symbols refer to experimental data, lines refer to simulation.	95

Figure 5.4. (a) void diameter and (b) void density as a function of anneal temperature. Si samples were implanted with different doses of He ⁺ at 300 keV. Experimental data were reported by Raineri <i>et al.</i> [99]. Symbols refer to experimental data, lines refer to simulation.	96
Figure 5.5. (a) void diameter and (b) void density as a function of anneal time. Si samples were implanted with 40 keV, 5×10 ¹⁶ cm ⁻² He ⁺ . Experimental data were reported by Raineri <i>et al.</i> [99]. Symbols refer to experimental data, lines refer to simulation.	97
Figure 5.6. Void diameter as a function of anneal temperature. Si samples were implanted with 30 keV, 1×10 ¹⁷ cm ⁻² He ⁺ . Experimental data were reported by Follstaedt <i>et al.</i> [11]. Symbols refer to experimental data, line refers to simulation.	98
Figure 5.7. Void diameter as a function of anneal time at 800°C. Si samples were implanted with 40 keV, 5×10 ¹⁶ cm ⁻² He ⁺ ions. Experimental data were reported by Roqueta <i>et al.</i> [92] and Kaschny <i>et al.</i> [156]. Symbols refer to experimental data, line refers to simulation.	98
Figure 5.8. Values of (a) k_{bulk} and (b) k_{SV} used in the simulations. Lines refer to the theoretical trend, symbols refer to the values used in the simulations.	100
Figure 5.9. Variation of k_I as a function of inverse temperature. Symbols are the values used in the simulations, lines represent the Arrhenius fits.	102
Figure 5.10. Variation of k_I as a function of dose. Symbols are the values used in the simulations, lines represent the linear fits.	103
Figure 6.1. B SIMS profiles in Si and Si _{0.95} Ge _{0.05} /Si samples annealed at 1090°C in RTA in N ₂ for 15 min followed by FA done at 970°C for 1 hour in N ₂ or dry O ₂	115
Figure 6.2. B SIMS profiles in Si and Si _{0.95} Ge _{0.05} /Si samples annealed at 1000°C in RTA in N ₂ for 15 min followed by RTA done at 1050°C for 30 min in N ₂ or dry O ₂	116

Figure 6.3. FLOOPS-ISE simulation of Ge interdiffusion after annealing for 15 min at 1000°C and 1090°C taking into account the damage created during 60 keV, $1 \times 10^{13} \text{ cm}^{-2} \text{ B}^+$ implantation. 121

Figure 6.4. Ge interdiffusion after annealing for 30 min at 1000°C taking into account the damage created during 30 keV, $5 \times 10^{16} \text{ cm}^{-2} \text{ He}^+$ implantation. 123

LIST OF TABLES

Table 3.1. Minimum He ⁺ dose requirements to form bubbles in Si with varying He ⁺ implantation energies [99]-[100], [102].	32
Table 4.1. Standard deviation (SD) in nm for void size distribution	71
Table 5.1: Experimental data available from literature	90

LIST OF COMMON ABBREVIATIONS AND SYMBOLS

As	Arsenic
B	Boron
CMOS	Complementary metal oxide semiconductor
C-RBS	Rutherford backscattering in channelling conditions
C_I	Concentration of interstitials
C_{SV}	Concentration of vacancies in small vacancy clusters
C_V	Concentration of vacancies
CVD	Chemical vapour deposition
C_{void}	Concentration of vacancies in voids
CZ	Czochraslski
D_I	Interstitial diffusivity
D_V	Vacancy diffusivity
D_{void}	Density of voids
EDX	Energy dispersive x-ray
EELS	Electron energy loss spectroscopy
ERD	Elastic recoil detection
FA	Furnace annealer
FLOOPS	Florida object oriented process simulator
FZ	Float-zone
Ga	Gallium
Ge	Germanium

He	Helium atom
He ⁺	Helium ion
I	Interstitial
IC	Integrated circuit
In	Indium
ISE	Integrated system engineering
keV	Kilo electron volts
M&C	Migration and Coalescence
MBE	Molecular beam epitaxy
MeV	Mega electron volts
MOS	Metal oxide semiconductor
N ₂	Nitrogen
NREBS	Non Rutherford elastic backscattering
NTRS	National technology roadmap for semiconductors
O ₂	Oxygen
OED	Oxidation enhanced diffusion
OR	Ostwald ripening
ORD	Oxidation retarded diffusion
P	Phosphorus
PAS	Positron annihilation spectroscopy
RT	Room temperature
RTA	Rapid thermal annealer

Si	Silicon
Si _{1-x} Ge _x	Silicon Germanium
Si _{1-x} Ge _x /Si	Si with a Si _{1-x} Ge _x epilayer
SiO ₂	Silicon dioxide
Si ₃ N ₄	Silicon nitride
SEM	Scanning electron microscopy
SIMS	Secondary ion mass spectroscopy
Sb	Antimony
TDS	Thermal desorption spectroscopy
TEM	Transmission electron microscope
XTEM	Cross section transmission electron microscopy
V	Vacancy
V _c	Cavity velocity
<i>b</i>	Covolume
<i>k_l</i>	Fitting parameter
<i>k_{bulk}</i>	Bulk recombination rate
<i>k_{SV}, k_{SI}, k_{void_V}, k_{void_I}</i>	Diffusion limited reaction rates
n	Size of a void
<i>N_o</i>	Number of cavities per unit area
<i>r</i>	Cavity radius
<i>r_b</i>	Capture radius of bulk recombination process

r_o	Vacancy radius
v_o	Mean cavity volume
μ_o	Chemical potential of He in cavities
μ_{ψ}	Chemical potential of interstitial He

Chapter 1

Introduction

1.1 Background

Silicon (Si) is the dominant material used in the semiconductor industry for the last many years. Though the first transistor was made with Germanium (Ge), and other materials offer higher carrier mobilities, higher energy band gap and higher carrier saturation velocities, Si has some advantageous properties compared to other materials. This has made Si to dominate the semiconductor industry. One obvious reason for Si to dominate is it being cheap and the raw material to produce Si wafers is abundantly available in nature. However, this is not the main reason that solely worked for Si to rule the world of semiconductor industry. Larger bandgap of Si compared to Ge reduces leakage current in Si devices compared to Ge devices. Si also has high thermal conductivity, which allows Si devices to operate at higher temperature. This facilitates to increase the packing density of Si based integrated circuits (IC) and may reduce the complexity in designing the cooling features for an IC system. Si also allows thermal growth of two insulators: silicon dioxide (SiO_2) and silicon nitride (Si_3N_4). These insulators are frequently used in isolation and passivation purposes in the device fabrication process. With the development of the device fabrication technologies, it is

possible to precisely control the growth and the etching of Si, SiO₂ and Si₃N₄. This results in very high uniformity in the device structure and results in high yield. Complementary metal oxide semiconductor (CMOS) is the dominant structure of the current Si based IC industry. CMOS structure provides properties like power dissipation only at the switching mode, low leakage current, and high frequency response. SiO₂ is used as the dielectric material in CMOS structure. Low leakage current is achieved due to SiO₂ offering excellent insulating properties against carrier transport. SiO₂ can be thermally grown over Si, the interface between Si and SiO₂ has low defect density and is stable.

Though Si based devices are dominating the semiconductor industry, Si also has several limitations. Si having an indirect bandgap restricts its use in photonic applications. Low carrier mobility and low carrier saturation velocity also restrict using Si in high frequency applications. III-V compound semiconductors, such as, gallium arsenide (GaAs), indium phosphide (InP) have direct energy bandgaps and provide both high carrier mobilities and high carrier saturation velocities making these compound semiconductors as ideal candidates to use in devices for photonic and high frequency applications. However, III-V compound semiconductors are fragile, have interfaces with lots of defects, have lower thermal conductivity compared to Si and lacks in forming reliable thermally grown oxide, all which increase the cost of device fabrication to a great extent.

In 1965, Intel co-founder Gordon Moore described his observation on the growth of the semiconductor industry by “the number of transistors that can be fit into a square

inch of silicon doubles every 12 months”, which is known as Moore’s law [1]. The pace of incorporating the number of transistors have however been decreased at present and the trend is to achieve this goal approximately in every 2 years [2]. The Semiconductor Industry Association has set the National Technology Roadmap for Semiconductors (NTRS), which works as the strategic plan for the semiconductor industry [3]. As the minimum feature size in device is decreasing, it has now been apparent that, Si itself has reached its limit in terms of being capable to meet the targets set in the NTRS. Thus, it is necessary to incorporate other materials in the standard CMOS processing steps to be able to continue meeting the requirements.

In recent years, incorporating silicon germanium (SiGe) in the CMOS processing steps has shown potential to meet some of the requirements set by NTRS. SiGe can be easily incorporated in the mature Si processing steps. SiGe offers higher electron mobility compared to Si, thus facilitates in meeting the high frequency operating requirements set in the NTRS roadmap.

1.1.1 Material Properties of $\text{Si}_{1-x}\text{Ge}_x$

$\text{Si}_{1-x}\text{Ge}_x$ crystallizes in diamond crystal structure and is composed of completely miscible Si and Ge with x ranging from 0 to 1. The lattice constant of Ge is 4.2% bigger than Si. The lattice constant of $\text{Si}_{1-x}\text{Ge}_x$ is always bigger than Si and depends on Ge fraction present in the structure. A very close approximation for $\text{Si}_{1-x}\text{Ge}_x$ lattice constant is given by Vegard’s law [4], which is,

$$a_{Si_{1-x}Ge_x} = xa_{Ge} + (1-x)a_{Si} \quad (1.1)$$

where, $a_{Si_{1-x}Ge_x}$ is the lattice constant of $Si_{1-x}Ge_x$, x is the fraction of Ge, a_{Ge} is the lattice constant of Ge, and a_{Si} is the lattice constant of Si.

Equation (1.1) shows that the lattice constant of $Si_{1-x}Ge_x$ varies linearly between the lattice constant of Si and Ge. The approximated values of $Si_{1-x}Ge_x$ lattice constant given by Vegard's law is very close to its actual value, which is given by Equation (1.2) [5]. The difference between the approximate and the actual value is only $1.8 \times 10^{-4}\%$.

$$a_{Si_{1-x}Ge_x} = 0.0002733x^2 + 0.01992x + 0.5431 \text{ (nm)} \quad (1.2)$$

Due to the lattice difference between Si and $Si_{1-x}Ge_x$, when $Si_{1-x}Ge_x$ is grown on Si substrate, lattice distortion is created in $Si_{1-x}Ge_x$ epilayer. In this case, $Si_{1-x}Ge_x$ epilayer remains under compressive strain as shown in Figure 1.1. On the other hand, if Si epilayer is grown on $Si_{1-x}Ge_x$ substrate, Si epilayer is under tensile strain, which is shown in Figure 1.2. If $Si_{1-x}Ge_x$ epilayer is grown on $Si_{1-y}Ge_y$ substrate, the amount of strain introduced in $Si_{1-x}Ge_x$ is determined by the fractions of Ge present in the epilayer and in the substrate. The epilayer will be under compressive strain if $x > y$, and will be under tensile strain if $x < y$.

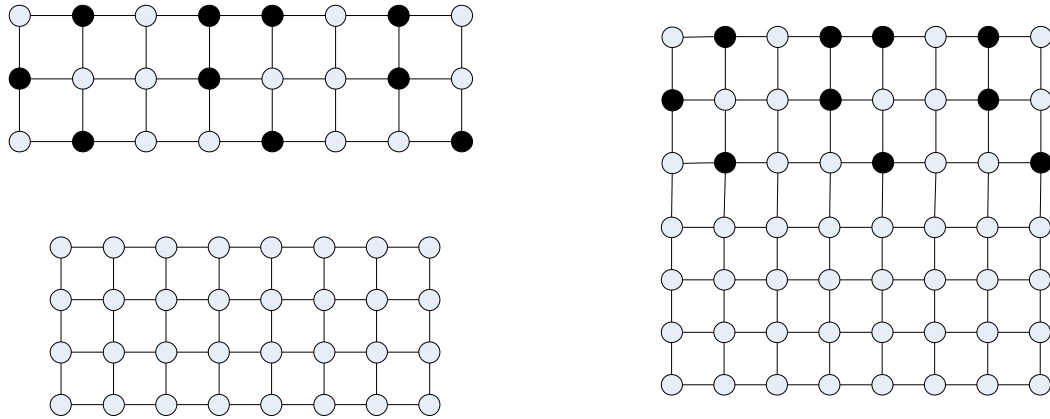


Figure 1.1. The top $\text{Si}_{1-x}\text{Ge}_x$ layer is grown on Si substrate. $\text{Si}_{1-x}\text{Ge}_x$ layer is under compressive strain [6].

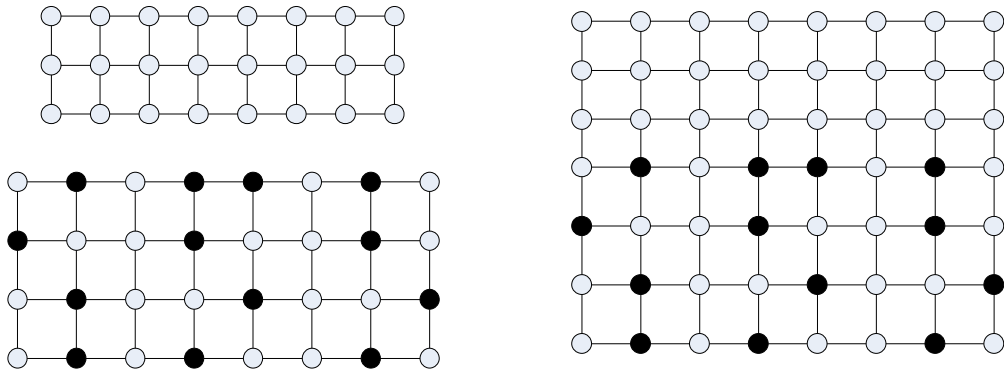


Figure 1.2. The top Si layer is grown on $\text{Si}_{1-x}\text{Ge}_x$ substrate. Si layer is under tensile strain [6].

When the epilayer in plane lattice constant is matched to the substrate in plane lattice constant, the grown film is pseudomorphic in nature. There is a limit in the epilayer thickness up to which strain can be introduced in the epilayer. The strain in the epilayer cannot be accommodated once the thickness of the epilayer exceeds a certain value, which is known as “critical thickness”. The thickness of $\text{Si}_{1-x}\text{Ge}_x$ epilayer up to which stable pseudomorphic film can be grown on Si is shown in Figure 1.3.

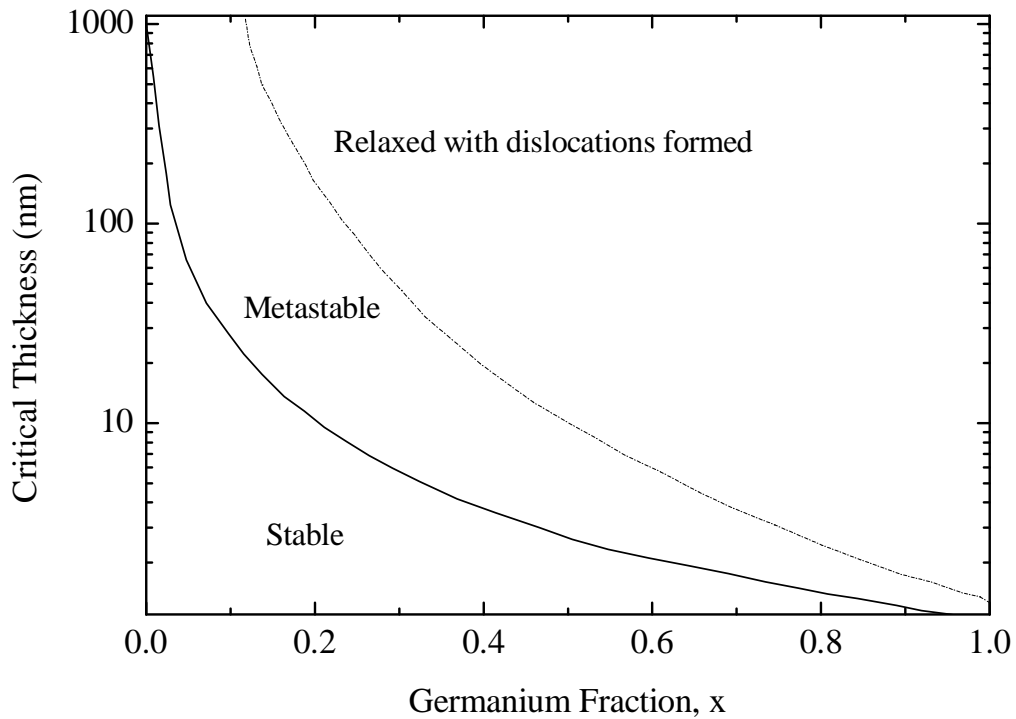


Figure 1.3. Critical thickness as a function of Ge fraction in $\text{Si}_{1-x}\text{Ge}_x$, where $\text{Si}_{1-x}\text{Ge}_x$ layers are grown on bulk (100) Si [6].

Critical thickness depends on the Ge fraction in $\text{Si}_{1-x}\text{Ge}_x$, increase in Ge fraction decreases the critical thickness. Beyond the critical thickness, the epilayer relaxes by forming misfit dislocations across the epilayer/substrate interface. Experimentally, however, it is observed that the pseudomorphic growth of as-grown $\text{Si}_{1-x}\text{Ge}_x$ epilayer is possible beyond the critical thickness as shown in Figure 1.3. In the metastable region, the as-grown film is pseudomorphic in nature, which relaxes during annealing by forming misfit dislocations.

Due to the potential of growing pseudomorphic $\text{Si}_{1-x}\text{Ge}_x/\text{Si}$ heterostructures, it is possible to get benefits from the associated bandgap and strain engineering. Tensile strain generated in Si can increase electron mobility, a feature which is applied to increase the carrier mobility in MOS channel [7]. The bandgap of $\text{Si}_{1-x}\text{Ge}_x$ is lower than that of Si. For each 10% Ge, a compressive strain further reduces the bandgap by approximately 75 meV [8]. The difference of bandgap between Si and $\text{Si}_{1-x}\text{Ge}_x$ facilitates in confining carriers in the structures containing $\text{Si}_{1-x}\text{Ge}_x/\text{Si}$ heterostructures. Strain also influences the equilibrium point defects in the structure. Equilibrium concentration of vacancies and interstitials respectively increases and decreases in the presence of compressive strain [9]. Tensile strain has an opposite affect [9]. A weaker Si-Ge bonding compared to Si-Si results in increase in the equilibrium point defect concentrations in $\text{Si}_{1-x}\text{Ge}_x$ [10]. The presence of $\text{Si}_{1-x}\text{Ge}_x$ thus may play an important role in the processes like dopant diffusion and point defect clustering.

1.2 Motivation Behind the Study

Point defects play an important role in semiconductor processing and in determining device characteristics. Point defects and their clusters can be controlled so that they can be beneficial to meet certain requirements. For example, voids, which are agglomerates of vacancies, show important technological applications. Voids are used for gettering transition metals, the process whereby metal impurities are chemisorbed to the internal dangling bonds of the voids [11]-[13]. Voids provide high binding energies to the metal impurities to work as efficient metal gettering sites. The binding energy depends on the size of the voids. For example, binding energy of gold atoms with cavities of 12 nm mean diameter has 0.13 eV higher binding energy than with cavities of 34 nm mean diameter, resulting higher gettering efficiency in smaller cavities compared to the larger ones [14]. Voids can also act as efficient interstitial sinks [15]-[16], and are thus capable of reducing transient enhanced diffusion of interstitial diffusers such as boron [16]. Other applications of voids may be in suppressing secondary defect formation [15], controlling minority carrier lifetime [13], and in the process of silicon-on-insulator fabrication using the wafer splitting technique [17]. Voids in Si can be formed by high dose implantation of helium (He^+) and subsequent anneal. Helium (He), being an inert gas, does not react with the Si lattice or other impurities present in the Si wafer. It has a high permeability in Si and effuses out from Si relatively easily upon high temperature annealing. These properties make it an attractive candidate to use in the void formation technique. The low solubility of He in Si leads to the formation of He-vacancy clusters upon implantation, creating bubbles that coarsen during subsequent annealing. For annealing done above

700°C, He effuses out from the bubbles leaving behind voids which are stable after annealing even for 5 hours at 1250°C [18]. Since the first report of void formation in Si by He⁺ implantation by Griffioen *et al.* [19] in 1987, numerous studies have been published in literature reporting different aspects of void evolution process.

The incorporation of Si_{1-x}Ge_x in Si CMOS processing is one of the ways to meet the continuous device scaling requirements [3]. Si_{1-x}Ge_x also shows an interesting potential in photonic applications, for example in producing photodetectors, photodiodes and waveguides [20]-[21]. The quantification of the effects of Si_{1-x}Ge_x on the outcome of processes normally reserved for silicon substrates remains an important area of study. It is reported that the presence of Ge affects oxidation kinetics, dopant diffusion and metallization processes [22]-[30]. Further the interdiffusion process of Si and Ge across a Si_{1-x}Ge_x/Si heterojunction can appreciably change the width of the heterojunction [31]-[41], which may also influence the device characteristics. While the role of Ge on different semiconductor processing steps has been reported, as yet there has been insufficient work on the impact of the presence of Ge on the void evolution process in Si. Considering this, one of the focuses of this thesis is to study the role of the presence of Si_{1-x}Ge_x epilayer on the void evolution process in Si. In semiconductor processing, different type of anneal ambients e.g., inert, oxidizing, nitriding are routinely used. However, the role of different anneal ambients on void evolution process is not available in literature. Thus, another focus of this thesis is to study the role of the anneal ambients on the void evolution process in Si both in the presence and without the presence of Si_{1-x}Ge_x epilayer on Si. Further, there is a lack of the availability of a physically based

mathematical model to describe void evolution under a wide range of experimental conditions. A reliable physically based mathematical model will allow a better insight into the actual processes occurring during void evolution. Developing a mathematical model to understand the physical mechanism involved in void evolution is the other focus of this study.

As the device dimension decreases, it is important to have precise control on dopant diffusion. Boron (B) is the most commonly used p-type dopant [2]. Since B has a very high diffusivity, controlling B diffusion width has always received lots of research attention. With $\text{Si}_{1-x}\text{Ge}_x$ being incorporated in fabrication steps, it has become necessary to study the role of the presence of $\text{Si}_{1-x}\text{Ge}_x$ on B diffusion process. Thus, in this study we have attempted to explore the role of the presence of $\text{Si}_{1-x}\text{Ge}_x$ epilayer on B diffusion process in Si. This also gives us the opportunity to correlate the results of void evolution and B diffusion processes and explore the phenomena which may play a role in governing the void evolution and B diffusion processes due to the presence of $\text{Si}_{1-x}\text{Ge}_x$ epilayer on Si.

1.3 Process Simulator: FLOOPS-ISE

FLorida Object Oriented Process Simulator (FLOOPS) was first developed in University of Florida and later was commercially developed by Integrated System Engineering (ISE). ISE later merged with Synopsys Inc. The commercially available version of FLOOPS is called as FLOOPS-ISE [9] and is now commercially available as a Synopsys process simulating tool. We have extensively used this commercial version of the process simulator in this study. FLOOPS-ISE is capable of simulating all common

process steps, for example, ion implantation, diffusion, oxidation, etching, and deposition. We extensively used ion implantation, diffusion and oxidation process steps of the simulator in this study.

In FLOOPS-ISE, during simulating process steps, in the region of interest, a grid is defined, where the mathematical equations are solved. The finer is the grid, the greater is the accuracy of the solution. However, the finer grid also increases the computational time. FLOOPS-ISE has a parameter database that contains the default values of material and model parameters. The simulator allows accessing the database and allows users to alter the default values if necessary. While simulating diffusion process steps by applying the “diffuse” command, the FLOOPS-ISE default diffusion model is “Fermi”, which considers that the point defects are always in equilibrium. The mathematical model proposed in this thesis however considers solving point defect equations during the diffusion process. The “Pair” diffusion model in the simulator allows solving point defect equations and we set this model in our simulations.

While solving mathematical equations in FLOOPS-ISE, it is necessary to set initial values to all the diffusing parameters. It is also required to set a boundary condition for the diffusing parameters. By default, FLOOPS-ISE sets “Honneumann” boundary condition at left, right and bottom boundary of the structure. “Honneumann” boundary condition considers no flux transfer across the boundary. We have set “Natural” boundary condition for vacancies and interstitials to allow flux transfer across the top boundary.

The simulator allows to incorporate user-defined partial differential equations by using the feature called Alagator Scripting Language. This facilitates to solve user-

defined mathematical models along with taking the advantages of using the features defined in FLOOPS-ISE. Users can also use the syntax of the programming language Tcl to apply an algorithm if necessary.

1.4 Organization of the Thesis

The thesis is organized into seven chapters. In the foregoing section, we have described the motivation behind the study and have introduced the process simulator used to apply to the developed model.

Chapter 2 provides a brief survey on point defects and dopant diffusion mechanisms. The chapter also briefly describes the ion implantation process and the point defect injection mechanisms in Si. The possible roles of these processes on the dopant diffusion mechanisms are also described.

In Chapter 3 we provide a review on void formation and evolution process by He⁺ implantation in Si. We categorize the features of the void formation and evolution process into different sections and summarize the results available in literature.

Chapter 4 describes the experimental details to study void evolution in our samples. We discuss the experimental results observed and give explanations on the role of the change of anneal ambients and the presence of Si_{1-x}Ge_x epilayer on void evolution in Si.

Chapter 5 presents the mathematical model proposed in this study to describe the void evolution process in Si by He⁺ implantation and subsequent high temperature annealing. We discuss the physical justifications behind developing the model equations and describe the approaches taken to apply the model in the process simulator. The

chapter also discusses different parameters considered in the model and provides comparison between the simulated results with the experimental results reported in this study and in the previously reported studies.

In Chapter 6 the role of the presence of $\text{Si}_{0.95}\text{Ge}_{0.05}$ epilayer on the B diffusion process in Si is reported. We describe the experimental details to study B diffusion process in presence of $\text{Si}_{1-x}\text{Ge}_x$. The experimental results are then correlated with the void evolution results in the samples with $\text{Si}_{1-x}\text{Ge}_x$ epilayer present on top of Si.

Finally, in Chapter 7 we give the concluding remarks on the study and provide possible future research directions.

Chapter 2

Point Defects and Dopant Diffusion Mechanisms

Since the beginning of the IC technology, study of dopant diffusion process has become an important area of research. While exploring the details of the dopant diffusion phenomena, it became evident that the interactions of dopants with the point defects dictate the dopant diffusion process. Many reports are available in literature describing point defect properties and dopant diffusion mechanisms. At present, ion implantation is the dominant technique used in industry to introduce dopants in semiconductor materials. Ion implantation process however introduces point defects in the lattice, which can influence the dopant diffusion process. Surface reactions, for example, oxidation of Si can inject interstitials and nitridation of Si can inject vacancies [2]. These processes thus can also influence the dopant diffusion process in Si. In this chapter a brief review on the point defects is provided. We also describe the influence of the point defects on the dopant diffusion process. While reviewing these processes, due to the extent of the studies reported, we shall limit ourselves only to the topics which are relevant to this study.

2.1 Point Defects

Any entity that interrupts the periodic arrangement of lattice is known as a point defect. Point defects play an important role in semiconductor process and device physics. For example, dopant diffuses by interacting with the point defects. Thus, any change in point defect concentration may alter the dopant diffusion profile.

In general, point defects can be divided into two categories: native point defects and impurity related point defects. Imperfections in the host lattice atoms create native point defects. When an atom is missing from its lattice position, it creates a vacancy at the original lattice position. A vacancy is thus an empty lattice site. When a host atom is not in its lattice position and resides at some other position in the lattice, it is called a self-interstitial. Two vacant lattices adjacent to each other form a di-vacancy and two interstitials bound with each form a di-interstitial.

Impurity related point defects are created in the presence of impurity atoms in the lattice. Dopants, which are in fact impurities, are intentionally introduced in Si. Group III elements, boron (B), gallium (Ga), indium (In) and group V elements arsenic (As), phosphorus (P), antimony (Sb) are introduced in Si to control the device properties. The usual positions for these dopants are in the substitutional sites in Si lattice. Dopants in substitutional sites are called substitutional defects. When dopants take up host lattice positions, displaced Si atoms become self-interstitial defects. When dopants take up any position in the lattice other than the substitutional positions, they are called interstitial impurities. Figure 2.1 shows a schematic representation of different types of point defects commonly seen.

There is another type of defect available, which is known as interstitialcy. This consists of two silicon atoms arranged together in non-substitutional positions. The combination of atoms is located around a substitutional lattice site. Interstitialcy can also be defined as an entity where there is an additional atom sitting together with an atom at the substitutional site. In literature, difference between self-interstitial and self-interstitialcy is usually ignored since both refer to an extra atom in Si lattice and are simply referred as interstitials.

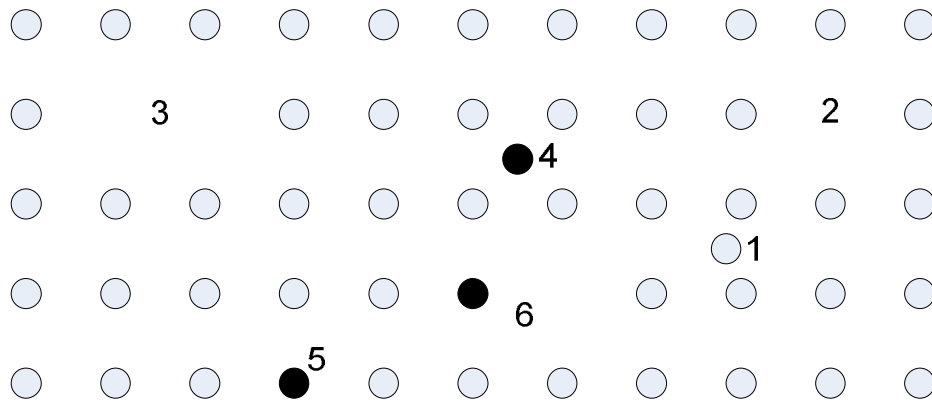


Figure 2.1. Different types of point defects. (1) self-interstitial, (2) vacancy, (3) di-vacancy, (4) interstitial impurity, (5) substitutional impurity, (6) substitutional impurity vacancy complex [42].

Point defects can form large defect aggregates. Interstitials can form $\{311\}$ defects, dislocation loops, whereas vacancies can form platelets, small vacancy clusters and voids. The formation and the dissociation of these defect aggregates can play a role in the dopant diffusion process.

2.2 Dopant Diffusion Mechanisms

Atoms diffuse in the crystal lattice by interacting with the point defects. One of the mechanisms by which atoms diffuse is called the vacancy exchange mechanism. In this process, the basic requirement is the presence of a vacancy adjacent to the atom sitting at a substitutional site. The substitutional atom diffuses by exchanging its position with the adjacent vacancy. Figure 2.2 shows a schematic representation of the process. The number of vacancies available adjacent to substitutional atoms plays a significant role in the atomic diffusion process. Usually the amount of diffusion increases with the increase in the number of available vacancies adjacent to the substitutional atomic sites. Now, if the atom keeps interchanging its position with the same vacancy back and forth, there will be effectively no diffusion occurring. After exchanging the position with an atom, vacancy must diffuse away some distance from the substitutional atom it has exchanged position with to prevent any back and forth exchange process happening. This vacancy can however come adjacent to the same substitutional atom later by following a different diffusion path and can again interchange its position with the atom.

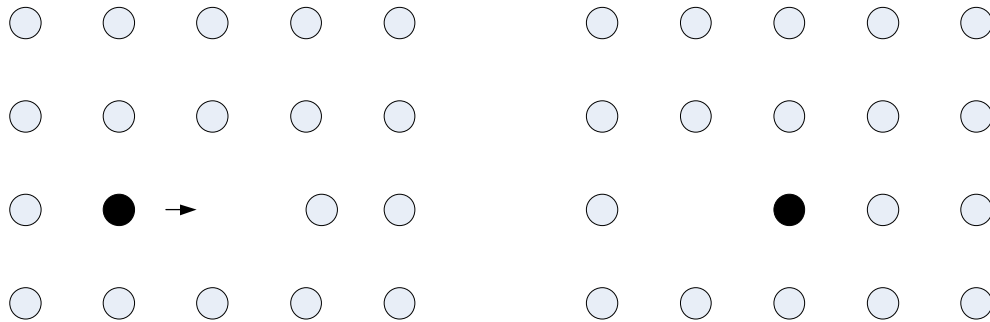


Figure 2.2. Vacancy exchange mechanism. ● represents a host atom or a dopant atom that diffuses by the vacancy exchange mechanism [43].

In another mechanism, an atom at interstitial site kicks out an atom sitting at the substitutional site and takes the substitutional position. The atom that is kicked out from the substitutional position now becomes an interstitial atom. This atom now diffuses through the interstitial sites until it knocks off another substitutional atom to take its position. This process is dependent on the availability of interstitials. The process is known as the “kick-out” mechanism. Figure 2.3 shows a schematic representation of the process.

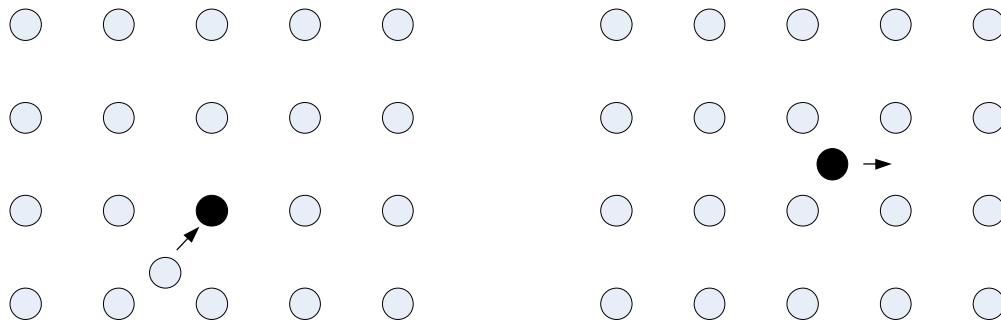


Figure 2.3. Kick-out mechanism. ● represents an atom initially at substitutional site, which later becomes interstitial atom and diffuses through the lattice [43].

In the interstitialcy diffusion mechanism, a silicon interstitialcy atom moves towards the adjacent lattice site where it can form a new interstitialcy defect. In this process silicon interstitialcy can form a dopant interstitialcy where the interstitialcy defect is formed with a silicon and a dopant atom. Dopant interstitialcy can diffuse in a similar way as shown in Figure 2.4. The “kick-out” mechanism and dopant interstitialcy diffusion mechanism are mathematically equivalent, and both are considered as “kick-out” reactions.

Another mechanism commonly observed is known as a “recombination process”. In this process, an atom diffusing through the interstitial sites comes close to a vacancy and recombines with the vacancy. This process thus results in annihilation of an interstitial atom and a vacancy. Figure 2.5 schematically shows this process.

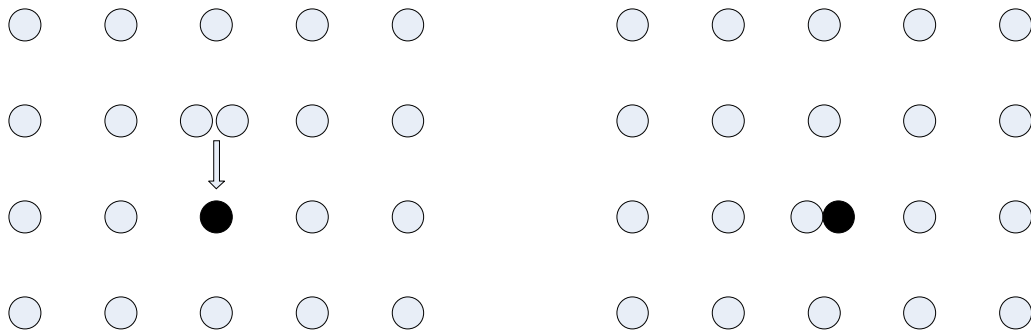


Figure 2.4. Interstitialcy diffusion mechanism. ● represents a dopant atom and ○ represents a Si atom [44].

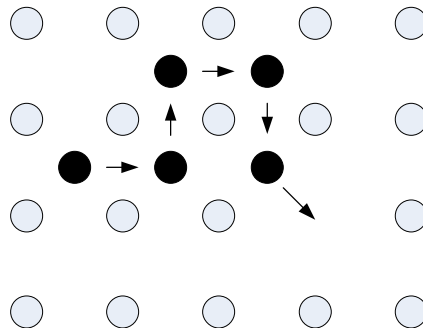


Figure 2.5. Recombination mechanism. ● represents a host or a dopant atom. [43].

Dopants usually diffuse either by a vacancy exchange mechanism, or by an interstitial assisted mechanism, or by combination of both processes. For example, B and P diffuse by the interstitial assisted mechanism, Sb diffuses by the vacancy exchange mechanism [2]. Arsenic on the other hand diffuses by both interacting with vacancies and interstitials [2]. Interdiffusion of host lattice atoms, for example, Si and Ge interdiffusion across a $\text{Si}_{1-x}\text{Ge}_x/\text{Si}$ heterojunction is also governed by the presence of point defects [40]-[41].

2.3 The Ion Implantation Process and Transient Enhanced Diffusion of Dopants

Ion implantation is the most popular technique to introduce dopants into Si during the CMOS processing steps. At present, in a typical CMOS chip fabrication, many individual ion implantation steps are necessary. Dopants can be introduced by diffusion from the surface as well. However, much more precise control in the dopant profile can be achieved by the ion implantation process [45]. In the ion implantation process, dopants are accelerated to high energy (from a few keV to several MeV) to put the dopants at a desired depth inside the sample. The projected range of implantation depends on the ion implantation energy. The higher the implantation energy is, the deeper is the range. Since the individual ion trajectories can be different in shape, some ions can stop at a shallower depth than the others. However, due to the statistical nature of the process, most of the implanted ions reach the projected range. The implanted profile thus shows a distribution of implanted ions. The distribution is quantified by a term called “straggle”. The spread of

the ions depends on the implantation energy since higher implantation energy allows the ions to travel to deep inside the samples, which results in increased amount of random stopping events. When the accelerated dopants enter Si, the dopants start interacting with the Si lattice atoms, give the energy to the Si atoms by nuclear and electronic stopping processes and come to rest inside the lattice. In the nuclear stopping process, the incoming energetic dopant atoms can knock off Si host atoms from their lattice positions. Si atoms thus knocked off can acquire sufficient energy and can displace other Si atoms from their lattice positions. The damage production during ion implantation process is therefore a cascade process. The incident atom is referred as the primary atom, which can produce secondary atoms. These secondary atoms having sufficient energy can produce damage like the primary atom. The process continues until the energetic atoms lose all the energy and come to rest. This collision cascade process produces lots of vacancies and interstitials. To produce damage, the transferred energy however must be greater than the displacement threshold energy, the minimum energy that is required to knock off an atom from its lattice position. The minimum energy required to form Frenkel pairs in Si is 15-20 eV [46]. Maximum amount of defects are usually formed near the projected range of the implantation, where the majority of energetic atoms come to rest by exchanging energy with the lattice atoms. In electronic stopping process, energy exchange occurs between the electrons of the atoms and the electrons in Si, and does not involve in any knock off of the host Si atom.

Each collision cascade usually occurs in the time span of about 10^{-11} sec [47]. The exact value is however dependent on parameters such as, dose, dose rate, mass of the ion

implanted. The total number of ions implanted is referred as dose of the ion implantation process. During the implantation process, within and around the collision cascade, the temperature increases for a very short time ($< \text{ps}$) [48]. Local heating usually occurs due to energy transfer that is lower than the energy required to form Frenkel pairs. The increase in heat results in recombination between vacancies and interstitials, a process that is commonly referred as “dynamic annealing” [49]. The amount and the type of damage accumulated depend on the dynamic annealing process to a great extent. Due to the dynamic annealing process, estimates show that 90-99% of interstitials and vacancies recombine with each other, i.e, 1-10% of the interstitials and vacancies created during the cascade collisions remain in the lattice [50].

During the ion implantation process, besides interstitial and vacancy formation, vacancy clusters, interstitial clusters, dopant defect clusters, amorphous pockets, etc. are formed. At room temperature, vacancies and interstitials are mobile [51]-[52]. However, due to having high value of migration energy, the defect clusters remain immobile at room temperature [53]. Also high binding energy prevents defect clusters from dissociating at room temperature [53]. Defect clusters are however capable of recombining with opposite type of point defects. As the ion implantation process progresses, the generated defects and defect clusters in the lattice can affect the trajectories of the oncoming dopants and thus can change the implanted dopant profile.

The damage production process is statistical in nature. The shape of the damage cluster depends on many factors, for example, mass of the incident and target atoms, implantation dose, implantation energy, dose rate, and implantation temperature. With the

increase in dose, the overlap between the damage cascades becomes more significant. As the amount of damage increases, clustering of point defects dominates over the dynamic annealing process [54]. Eisen and Welch [55] reported the role of dose during ^{11}B implantation in Si at room temperature. At a dose below $4 \times 10^{15} \text{ cm}^{-2}$, the point defects created during the implantation process are mobile and can recombine with each other. At a dose higher than $4 \times 10^{15} \text{ cm}^{-2}$, due to the presence of high defect densities, mobilities of vacancies and interstitials are reduced, and defect cluster formation is more favourable. Eisen and Welch [55] suggested that the defect clusters limit the motion of vacancies and interstitials by capturing those and thus vacancies and interstitials are not able to recombine with each other. Increase in dose rate decreases the time interval between the collision cascades. Thus less time is available for the dynamic annealing process. This leads to an increase in the amount of damage created. Implantation temperature also plays an important role in damage creation process. Increased implantation temperature increases the dynamic annealing process, thus reducing the amount of damage remaining in the lattice.

Implantation done with light ions like B usually creates Frenkel pairs and small defect clusters. On the other hand, implantation done with heavy ions like In and Sb creates amorphous pockets and large defect clusters [48]. For heavy ions, a higher fraction of their energy is transferred to Si lattice by the nuclear collision process, resulting in greater amount of damage production. Defects created by light ion implantation are easier to remove upon annealing compared to those in heavy ion implantation. The temperature required to remove defects depends on the type of the

defects present. For example, interstitials and vacancies are mobile even below room temperature and can recombine with each other, or can diffuse to the surface, or can recombine with other complex type defects [56]. Di-vacancies anneal out at 250°C [57] and di-interstitials anneal out at 150°C [58]. Other complex type defects such as {311} defects, dislocation loops, vacancy clusters require much higher temperature to anneal out.

The concentrations of point defects created during ion implantation process are very large compared to the equilibrium point defect concentrations. Also, the dopants introduced are in interstitial positions and are electrically inactive. To activate the dopants and to anneal out the point defects generated during the ion implantation process, high temperature annealing is required, which at the same time broadens the as-implanted dopant profile. This enhancement of the as-implanted dopant profile is known as transient enhanced diffusion (TED) [2]. Dopants can also form pairs with defects, which do not take part in the dopant activation process and thus reduce the number of electrically active dopants [59]. The enhancement in dopant diffusion persists until all the excess defects created during ion implantation process are annealed out. Typically when annealing is done, vacancies and vacancy related clusters decay first resulting in interstitial type defects to remain in the lattice [2]. {311} defects are the dominant type of interstitial clusters which are produced at the very initial stage of annealing. For example, {311} defects are reported to be visible even after annealing done at 600°C for 1 sec [2]. These interstitial clusters act as storage of interstitials, which start to emit interstitials during high temperature annealing. Since B diffuses by an interstitial assisted mechanism, these

dissolved interstitials can contribute to the B diffusion process [60]. Once all the interstitial clusters dissolve, B diffusivity reduces to its intrinsic value. Eaglesham *et al.* [60] reported that the amount of interstitials released from {311} defects during annealing is related to the flux of the interstitials that drives the TED process of B. TED is reported to be dependent on ion implantation energy as well [2]. For high energy implants, the surface does not appear to be a dominant sink for the damage produced. This typically causes increase in TED of dopants. The implant dose also plays a role in TED process. Increase in implant dose increases the lattice damage which then results in increase in TED of dopants.

2.4 Point Defect Injection and Effect on Dopant Diffusion Process

Annealing Si in oxidizing and nitriding ambients can respectively inject interstitials and vacancies into the bulk and thus can affect the dopant diffusion process. Oxidation of Si is routinely carried out during CMOS processing steps. As there is no way to track point defects directly, indirect approaches are taken to track the point defects injected in Si. By looking at the dopant diffusion behaviour, injection of point defects in Si can be observed. For example, B diffuses only by interstitial assisted mechanism and Sb diffuses only by vacancy assisted mechanism. Thus during interstitial injection, enhanced B diffusion and suppressed Sb diffusion occurs. On the other hand, during vacancy injection, enhanced Sb diffusion and suppressed B diffusion occurs. During Si oxidation process, any increase in dopant diffusion is commonly known as oxidation

enhanced diffusion (OED) and any reduction in dopant diffusion is known as oxidation retarded diffusion (ORD). Suppressed diffusion of Sb during annealing Si in oxidizing ambient suggests that due to interstitial injection occurring during oxidation process, there is a corresponding suppression in vacancy concentration.

One of the earliest reports available in literature that mentions enhanced B and P diffusion during oxidation of Si dates back to 1966 [61]. Later, Masetti *et al.* [62] reported enhanced P diffusion in $\langle 111 \rangle$ CZ Si when annealed in the temperature range 1000-1200°C in oxidizing ambient. Injection of interstitials during oxidation of Si was reported the reason behind enhanced diffusion of B and P. B diffusivity in $\langle 100 \rangle$ Si during dry O₂ annealing at 850°C has been reported to increase by a factor of 100 [63]. The rate of oxidation and thus the amount of interstitials injected depends on the crystallographic index of the Si crystal surface. The rate of dry oxidation increases in the sequence of Si orientations of $\langle 111 \rangle$, $\langle 110 \rangle$, and $\langle 100 \rangle$ [64]. The enhancement of B diffusion in Si under dry oxidation also increases in the same sequence of Si orientations [64]. Francis and Dobson [65] however reported retarded diffusion of B and P in $\langle 111 \rangle$ oriented Si when oxidation was done above 1150°C. The authors also reported enhanced Sb diffusion for similar experimental conditions, suggesting injection of vacancies occurring in this case. Vacancy injection process during oxidation of $\langle 111 \rangle$ Si for annealing done above 1150°C has also been confirmed by Hill [64] and Tan and Ginsberg [66].

Hu [67] proposed that during oxidation of Si, a portion of Si is displaced from the regular lattice position and is not oxidized. This displaced Si diffuses towards the SiO₂/Si

interface and is injected inside Si as interstitials. Dunham and Plummer [68] proposed that interstitials are created during the formation of SiO₂ and are accumulated at the SiO₂/Si interface. The amount of interstitials injected in Si is determined by the difference between the interstitial creation rate and the amount of interstitials diffused towards SiO₂. Dobson [69] on the other hand described that the compressive stress generated in the grown SiO₂ layer leads to the observed interstitial injection phenomenon. Dobson mentioned that interstitial injection occurs since it facilitates the volume expansion process which is required for SiO₂ layer to grow.

Vacancy injection mechanism is observed during nitridation of Si. Enhanced diffusion of Sb [70]-[75] and suppressed diffusion of P and B [25], [44], [71], [76]-[77] during nitridation of Si suggests vacancy injection phenomenon taking place. During the nitridation of Si, the nitride layer is pinned to a 50Å thickness [78]. Continuation of annealing in nitriding ambient keeps vacancies injected in Si, though the nitride layer thickness is pinned. With nitride layer present if annealing is done in inert ambient, vacancy injection continues to occur. Vacancy injection however stops if the nitride layer is removed and annealing is done in inert ambient [79]. Frenkel defect generation at the Si/Si₃N₄ interface is a possible source of injected vacancies as reported by Ahn *et al.* [80]. However, a more plausible mechanism behind vacancy injection during nitridation of Si is the presence of the tensile strain in Si₃N₄ layer that tries to relax during annealing [81]. To assist the relaxation process, Si from the bulk diffuses towards the Si/Si₃N₄ interface and results in vacancy supersaturation in the Si bulk.

Chapter 3

Factors Influencing Void Formation in Silicon by Helium Implantation

Voids in Si have many important technological applications which we have mentioned in Section 1.2. Given the range of applications, there has been significant interest in the study of void formation in Si by He⁺ implantation in recent years. There are reports available that mention attempts to form voids in Si by implanting with other inert gases, neon (Ne⁺), argon (Ar⁺) and krypton (Kr⁺) [82]-[88]. However, the voids formed by implanting Ne⁺, Ar⁺ and Kr⁺ are found to be partially or fully filled with these gases, which puts limitations on using voids in their practical applications. On the other hand, He effuses out of the sample upon annealing, leaving behind empty voids. Several studies have been published that describe different aspects of void formation in Si by He⁺ implantation. Void size and density can be altered by changing the implant and anneal conditions. In this chapter, we present a summary of published work on void growth and evolution in Si by He⁺ implantation. We follow the same definitions used in the literature to define different void related entities. A vacancy cluster filled with He is referred to as a “bubble”. An empty vacancy cluster is defined as “void”. The term “cavity” represents

both “bubble” and “void”. Throughout the thesis, we extensively use the term “cavity”, where the appropriate meaning of the term is set in context of the relevant discussion.

3.1 Void Formation Mechanism

Voids in Si can be formed by high dose implantation of He^+ and subsequent anneal. He is an inert gas and does not react with Si lattice or with any impurity present in the Si wafer. He has a high permeability in Si and effuses out from Si quite easily upon high temperature annealing. It neither reacts chemically with Si nor remains in the lattice after the semiconductor processing steps are finished. These properties of He make it an attractive candidate for use in void formation technique.

The first report on void formation in Si by He^+ implantation dates back to 1987 [19]. Since then, numerous papers have been published reporting theoretical and experimental aspects of the growth and evolution of voids. The most common way of forming voids in Si is by implanting with high-energy He^+ ions and performing subsequent high temperature ($> 700^\circ\text{C}$) annealing. The low solubility of He in Si leads to the formation of He-vacancy clusters, creating bubbles that coarsen during subsequent annealing. For annealing done above 700°C , He effuses out from the bubbles leaving behind voids.

During He^+ implantation, due to the cascade collision process, vacancies and interstitials are created at concentrations several orders of magnitude above their equilibrium concentrations. Molecular dynamics calculations show that He is strongly repelled by mono vacancies and the most stable position for He in the Si lattice is the

interstitial position far away from mono vacancies [89]-[90]. The repulsion energy between He and mono vacancy is reported to be 1.2 eV, which is slightly greater than the activation energy of 0.84 eV for He interstitials to diffuse [90]. This results in a separation between vacancies and He interstitials in the lattice, and He interstitials are pushed into the bulk due to the incoming flux of vacancies from the surface during He implantation process. During the implantation process, along with mono vacancies, divacancies and small vacancy clusters are also created. To minimize the free energy of the system, divacancies and the small vacancy clusters capture He [90]. This stabilizes the divacancies and small vacancy clusters against recombining with interstitials. These He filled structures can then evolve into more complex He_mV_n bubbles. Cerofolini *et al.* [91] reported that vacancy clusters tend to form tensile displacement field in the neighbouring region. This tensile field attracts He, thus forming a He atmosphere around vacancy clusters, which assists the process of vacancy clusters to be filled with He. Further, relatively weak He-He repulsive potential along with low solution enthalpy of ~ 1 eV leads to segregation of He inside cavities to a very high concentration [91]. The cavity layer can also contain $\{311\}$ defects and dislocation loops [92]. For anneals at temperatures $\geq 800^\circ\text{C}$, $\{311\}$ defects are only observed for very short time (less than a minute). $\{311\}$ defects dissolve either forming dislocation loops [93]-[94] or releasing free interstitials that diffuse towards the surface or recombine with vacancies and voids in the bulk. However, we must consider that during the dissolution of the $\{311\}$ defects, cavities are still filled with He. He tends to stabilize the cavities, thus reducing any possibility of interstitials to recombine with cavities. As the high temperature annealing

progresses, bubbles coarsen to grow in size and at the same time He effuses out from Si leaving behind empty bubbles i.e., voids. In addition, the number of interstitials required to reduce the radius (r) of a cavity increases as a function of r^2 . Thus, large voids may coexist with $\{311\}$ defects and dislocation loops. Any recombination of voids with interstitials dissolved from the interstitial type defects will not reduce the void radius significantly. Thus, stable void formation occurs. The dislocations in the void band can also arise from the stress introduced into the lattice by the voids [95]-[96].

Experimental studies report a close correlation between the number of Si atoms in the step volume at the surface and the number of vacancies in the voids. Si atoms displaced during void formation accumulate at the steps in the surface [97]-[98].

3.2 Role of He⁺ Implantation Dose

The dose of He⁺ implantation plays an important role in the void formation process [98]. The minimum dose of He⁺ implantation required to form bubbles increase with the increase in implantation energy as shown in Table 3.1. It is suggested that to form bubbles, the local He concentration at the projected range of implantation should be at least $3.5(\pm 1) \times 10^{20} \text{ cm}^{-3}$ [99]-[100]. Due to the increase in straggle with the increase in implantation energy, an increased He⁺ dose is required to achieve this He concentration at the projected range [99]-[100]. The minimum dose required to form bubbles is commonly called the “critical dose”. Implantation done below the critical dose does not form any voids during high temperature annealing.

We can further refine this picture by considering three dose regimes. The values of the doses in the regimes are dependent on the He⁺ implantation energy. In the low dose

regime ($<5 \times 10^{15} \text{ cm}^{-2}$ for implantation energy of 20 keV) no voids are produced in the sample either during as a result of the implant or after annealing. In the high dose regime ($>1 \times 10^{16} \text{ cm}^{-2}$ for implantation energy of 20 keV) transmission electron microscopy (TEM) images show that bubbles are formed in as-implanted samples and high temperature annealing produces voids [101]. For doses in the medium dose regime ($5 \times 10^{15} - 1 \times 10^{16} \text{ cm}^{-2}$ for implantation energy of 20 keV), as-implanted samples do not show any voids in TEM images. However, voids are produced after high temperature annealing. Si being highly permeable to He, He escapes from Si when annealing is performed. Thus, it is believed that to produce voids after high temperature annealing, bubbles must be produced during the He^+ implantation process. In medium dose He^+ implantation cases, it is possible that the sizes of the as-implanted bubbles are smaller than the resolution of the electron microscope. Thus, the bubbles cannot be seen in the TEM images in the as-implanted sample.

Table 3.1. Minimum He^+ dose requirements to form bubbles in Si with varying He^+ implantation energies [99]-[100], [102].

Implantation Energy (keV)	Minimum Dose (cm^{-2})
20	5×10^{15}
40	1×10^{16}
300	1×10^{16}
1000	1.5×10^{16}
1600	2×10^{16}

As mentioned above, the presence of a critical dose below which no voids form has led researchers to suggest that voids are formed when the local He concentration is at least $3.5(\pm 1) \times 10^{20} \text{ cm}^{-3}$ during room temperature implantations. However, it was reported by Simpson and Mitchell [100] that increasing the anneal ramp rate can facilitate void formation for local He concentration as low as $1.5 \times 10^{20} \text{ cm}^{-3}$. In addition, Raineri *et al.* [97] have reported that after implanting Si with a low dose of He^+ , if a second implantation with Si is performed to a shallower depth, high temperature annealing can create voids. Vacancies created during the second stage Si implantation supply the vacancies necessary to form voids. Thus, the local He concentration may not be the limiting factor that determines the condition for void production in Si. Rather, the availability of vacancies limits the void production. We shall look at the factors that determine the condition of void formation in Section 3.2.1.

In high dose implant cases, during high temperature annealing, void evolution progresses by migration and coalescence of the as-implanted bubbles [103]. He effuses out from the bubbles and forms voids. Both the as-implanted bubbles and the final voids are spherical in shape.

In medium dose cases, the void evolution progresses following a different route. Annealing performed at high temperature (800°C) produces a planetary like arrangement of over pressurized gas-filled bubbles [104]-[107]. The planetary arrangement consists of a large central bubble surrounded by smaller bubbles. A strong strain field surrounds the planetary bubble arrangements. The basic bubble coarsening mechanism, which is applicable for the high dose case, is not sufficient to describe the bubble evolution in this

scenario. Thus, an alternative description has been proposed to describe the bubble evolution in the medium dose regime [106]-[107]. It is proposed that during implantation, stable He_mV_n clusters are formed. When annealing is done between 400-470°C, platelet bubbles are formed by coalescence of He_mV_n clusters. With the increase in platelet bubble size, the strain field around the platelet bubble increases, which prevents further capture of He_mV_n in the platelet. Instead, the He_mV_n clusters are captured in the strained region around the platelet. This forms a planetary like arrangement. For annealing done between 470-700°C, the bubble at the center of the planetary arrangement becomes ellipsoidal in shape. For annealing done above 800°C, the bubbles of the planetary arrangement transform into spherically shaped bubbles. The shape transformation happens to facilitate relaxation of the high pressure of He inside the bubbles. It has been reported that, under high internal pressure in bubbles, formation of clusters of bubbles is more favourable as the total energy of cluster of bubbles is less than the energy of a single large bubble [108]. Increasing the substrate temperature to 350°C during He^+ implantation in the medium dose regime changes the bubble characteristics and results in spherical bubbles with diameters of 3-5 nm surrounded by dislocation loops [109].

3.2.1 Why Voids Grow Above “Critical Dose”?

Different experimental techniques have been used to investigate the reason behind cavity formation above the critical dose. Commonly used techniques are cross section transmission electron microscopy (XTEM), Rutherford backscattering in channelling conditions (C-RBS), thermal desorption spectrometry (TDS), elastic recoil detection (ERD), and positron annihilation spectroscopy (PAS). Attempts have been made in

literature to correlate the experimental results from different techniques to formulate a theory to describe the reason behind the cavity growth above the critical dose.

While investigating the phenomenon that governs the void evolution process above critical dose, focus has been given to study the interaction of He with Si lattice. Attempts have been made to study the behaviour of He in Si during low dose and high dose He⁺ implantation conditions and subsequent high temperature annealing. ERD technique has been applied to detect He distribution in Si for low dose and high dose He⁺ implantation cases [110]-[111]. He is reported to be accumulated on bubble layer during high dose He⁺ implantation. For low dose He⁺ implantation, ERD measurements does not show He to be accumulated in any defined layer. This indicates that in high dose regime He effusion occurs from the vacancy clusters/cavities during the annealing process.

Positron annihilation spectroscopy (PAS) is capable of detecting open volume defects like voids [112] and thus has been applied to get a better understanding of the void evolution mechanism. PAS is capable to detect mono vacancies to voids, making it a strong tool to quantify the average size of vacancy clusters. However, it must be noted that the open volume defects act as positron traps only if they are empty or partially filled with He [113]. When voids are filled with He, the PAS signal decreases and leads to smaller value for S parameters compared to the same in empty voids [113]. PAS studies done for samples with low dose and high dose He⁺ implantations and annealed at 250°C gives similar values of S parameters in the defects indicating the presence of divacancies and the formation of stable voids are initiated at higher temperature [114]. Annealing done at 450°C and above temperatures show a difference between the cavity evolution

process for low dose and high dose He⁺ implantation cases. The S parameter values suggest that, for low dose case, vacancy clusters consisting of 4 vacancies are available, whereas for high dose case, vacancy cluster size progressively increases with the increase in temperature indicating clusters containing 3, 4, 6 vacancies. For annealing done above 700°C, high dose He⁺ implantation case shows stable cavity formation, however, vacancy clusters for low dose implantation case starts to disappear.

To further investigate the behaviour of He in Si, TDS technique has been used in a few studies [101], [115]-[116]. TDS is reported to be an efficient tool to study the interaction of He with the vacancy clusters. TDS shows distinct He effusion characteristics in Si for He implantation doses set below and above the critical dose. Based on the He effusion kinetics, for high dose and low dose implantation of He⁺, hypotheses are proposed on the type of vacancy clusters formed where He remains trapped. This also allows to theoretically describe why void evolution is suppressed below the critical dose of He⁺ implantation. Figure 3.1 shows TDS spectra reported by Corni *et al.* [115], where 20 keV He⁺ was implanted at room temperature in Si with different doses and annealed at a rate of 45°C min⁻¹. From the figure we find that, for low dose He⁺ implantations (1.4×10^{15} and 5×10^{15} cm⁻²), He effusion occurs only at low temperatures in the range 250-400°C. This nature is attributed to He effusing from unstable He_mV_n clusters. High temperature annealing results in the vacancy clusters to recombine with interstitials and results in disappearance of the vacancy clusters [116]. For high dose He⁺ implantations (2×10^{16} and 3.5×10^{16} cm⁻²), along with He effusion occurring at low temperatures, there is

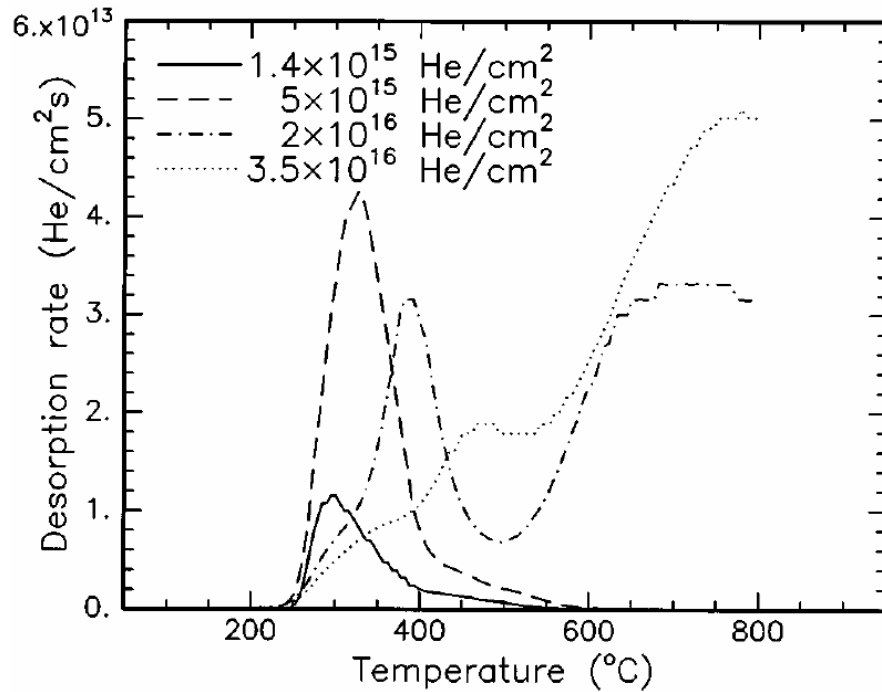


Figure 3.1. TDS spectrum of He for different He⁺ implantation doses [115].

another effusion peak occurring at high temperatures. He effusion at high temperatures occur from stable pressurized He filled bubbles. After He effuses out during high temperature annealing, these bubbles forms stable voids. For medium dose He⁺ implantation cases, similar to high dose implantation cases, He effusion peaks are observed both at low and high temperatures. Frabboni *et al.* [101] reported TDS of He effusion for medium dose implantation case where Si was implanted with 20 keV, 1×10^{16} cm⁻² He⁺. To obtain a better insight on He effusion characteristics and to correlate TDS measurements with the state of cavity evolution, Frabboni *et al.* also studied *in situ* TEM images using the same annealing ramp used for the TDS measurements. TDS spectrum shows low temperature effusion occurring for temperature less than 350°C with the

effusion peak centered at 260°C. Similar to high dose implantation case, He effusion at this temperature range occurs from unstable He_mV_n clusters. High temperature effusion of He starts from 450°C. He effusion in the range $450^\circ\text{C} < T < 570^\circ\text{C}$ occurs from He filled platelets or bubbles that upon annealing at higher temperature forms planetary like arrangement of cavities. Annealing done above 570°C results He effusion from stable cavities that form planetary like arrangement.

Brusa *et al.* [114] and Corni *et al.* [115] mentioned that the tendency of He to form clusters is the basic phenomenon that governs the bubble formation process. It was mentioned that in the region of high He concentration, He clustering mechanism is more efficient. However, to accommodate the He clusters, vacancies must be available in the lattice. With the increase in local He concentration (which can be achieved by increasing the dose), the size of the He cluster increases. To form stable bubbles, He clusters must attain a critical size. To accommodate these He, at least 4 vacancies are necessary. It was mentioned that once the critical He cluster size is reached, exothermic transformation of He atoms in solid solution into the gas phase inside the vacancy clusters creates energy to form Frenkel pairs in the neighbouring region. Vacancies thus created can accommodate the remaining He available in the lattice. For low dose He^+ implantation, on the other hand, it was mentioned that due to lower He concentration, He clustering process is less probable to occur resulting in smaller vacancy cluster size. Raineri *et al.* [97] and Simpson and Mitchell [100] showed doubt on the possibility of local He concentration to determine the condition of stable void creation. They showed that stable voids can be created even with local He concentration less than $3.5(\pm 1) \times 10^{20} \text{ cm}^{-3}$, the value which is

proposed in some reports. Rather, the availability of vacancies is the factor that plays the determining role in stable void formation process.

Later, Pivac *et al.* [110] proposed that when small vacancy clusters have more than 4 vacancies, the volume inside the vacancy clusters is large enough to facilitate an exothermic phase transformation of He atoms in solution to He in gas phase inside the vacancy clusters. The transition of He into gas phase places He at a lower energy state, thus higher temperature is required to effuse He out of Si. This leads to formation of voids during high temperature annealing. The gas phase transition of He does not occur when the number of vacancies in small vacancy clusters is less than 4 and He remains at a higher energy state. This results in He effusion from the vacancy clusters at a lower temperature. Thus for low dose He⁺ implantation cases, high temperature annealing does not produce voids.

Based on the above discussions, it is apparent that the small vacancy clusters must be composed of at least 4 vacancies to be capable to form voids upon annealing [115]. This criterion is not met during low dose He implantation situation. Corni *et al.* [115] suggested that at the initial stage of cavity formation, when the vacancy cluster sizes are small, the very high pressure of He inside the clusters leads to smaller values of He enthalpy of solution. Quantum effects arising due to confinement of He in a very small region along with repulsion force acting between closely packed He atoms and the interaction of He atoms with the inner surface of the clusters results in lower He enthalpy of solution in the smaller clusters. He gas pressure inside very small vacancy clusters can be very high, in the order of 10^9 Pa. Such a high pressure results in He

effusion at relatively lower temperature. Once He effuses out from small vacancy clusters at low temperature, the small vacancy clusters can recombine with interstitials. This inhibits the growth of large voids. For medium dose and high dose He implantation cases, the size of as-implanted vacancy cluster size increases. Thus the above mentioned effects are no longer present in the system and void evolution can proceed. In fact, He enthalpy of solution increases with the increase in vacancy cluster size, reaching maximum for large cavities.

An obvious question thus may arise, what dictates the size of the small vacancy clusters? A possible explanation can be, during low dose He⁺ implantation, the point defects produced are capable to recombine due to their rapid motion and the reduced amount of available vacancies limits the size of the small vacancy clusters. At medium and high dose He⁺ implantations, the higher amount of produced damage may restrict the recombination between the point defects and are captured by nucleation centers to form bigger sized vacancy clusters.

3.3 Which Process Dominates: Migration and Coalescence or Ostwald Ripening?

While different aspects of the void evolution process in Si have been studied for more than two decades, there has been a constant debate on the mechanism driving void evolution. Two mechanisms have been proposed to explain void coarsening: Ostwald Ripening (OR) and Migration and Coalescence (M&C). In the Ostwald ripening process, vacancies are emitted from smaller cavities (A in Figure 3.2) and are captured by the

bigger ones (B in Figure 3.2). This results in the growth of larger cavities and at the same time the shrinkage of the smaller ones. Bulk diffusivity of vacancies is the characteristic parameter in this process.

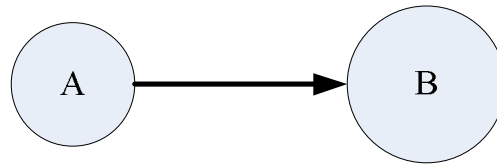


Figure 3.2. Ostwald ripening mechanism.

In a migration and coalescence process as shown in Figure 3.3, cavities migrate in random directions and coalesce when they come in contact and form larger cavities. For sub-micron sized cavities, the migration process is generally a surface diffusion process, so surface diffusivity of adatoms is the characteristic parameter for this process and smaller cavities would be expected to migrate faster than larger ones [103], [117]. Observation of void evolution by *in situ* TEM images is considered to be a reliable method to determine whether OR or M&C mechanism dominates.

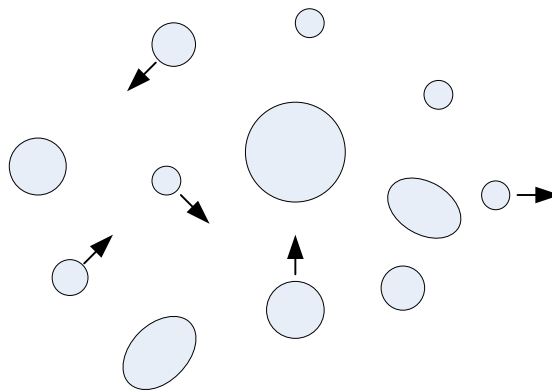


Figure 3.3. Migration and coalescence mechanism.

There are few reports available attempting to identify whether OR or M&C process acts behind the void evolution process. In the first published work of void formation by He⁺ implantation in Si by Griffioen *et al.* [19], it was reported observing *in situ* TEM images that M&C process is the mechanism working behind void coarsening. In their following work, it was reported observing *in situ* TEM images that the presence of O inhibits the M&C process [118]. Raineri *et al.* [99] further supported that the M&C process to be dominant while explaining their experimental results for void evolution. Later Follstaedt *et al.* [11] in their study looked at the void size distribution and pointed out that since the void size distribution appears to be symmetric in shape, M&C process is the dominant mechanism. TEM images frequently shows elongated voids after high temperature annealing. It is believed that elongated voids are newly merged voids formed by coalescence process.

Donnelly *et al.* [119] studied the void evolution in presence of O impurity, and noticed decrease in void diameter. It was reported that the presence of O impedes the diffusion of He and vacancies, thus reducing the diameter of the grown voids. For annealing done below 700°C, where cavities are still likely to be filled with He, migration of the cavities were not observed, and OR process has been identified as the cavity growth mechanism. For annealing done in higher temperatures as high as 850°C, the authors did not observe any motion of small cavities. Instead, for example, at 840°C, the authors reported to observe ‘jerky’ motion of large cavities. It was mentioned that the presence of nearby extended defects may be the reason behind this kind of behaviour. The cavities being threaded by dislocations can impede the motion as was later pointed out by

Vishnyakov *et al.* [120]. Raineri *et al.* [121] on the hand, argued for OR mechanism to be dominant for anneals at 800°C based on a theoretical analysis applied on experimental results reported by Roqueta *et al.* [92]. For higher temperatures Raineri *et al.* were not able to determine whether OR or M&C mechanism dominates. However, it must be noted that determination whether OR or M&C dominates was dependent just on separation of one data point. Thus the reliability of their argument is questionable. Further, it was reported by Raineri *et al.* [99] that during the void evolution process, the total void volume remains constant for annealing done at least up to 1000°C. During OR mechanism, vacancies emitted from voids can recombine at the wafer surface instead of being captured by other voids. Thus, the condition of constant void volume criteria may not be met if OR mechanism is dominant.

To get a better understanding on the role of OR and M&C mechanisms on the void evolution process, Evans [103] carried out numerical simulations to identify whether OR or M&C mechanism dominates during void evolution process for high dose He⁺ implantation. Evans reported that up to 1000°C, M&C mechanism is the dominant process. Above 1000°C, OR mechanism may play some role but only if for some reason M&C mechanism is suppressed. To simulate OR mechanism, Evans applied the equation described by Greenwood *et al.* [122], and for M&C mechanism, Evans applied the simplified form of equation described by Chandrasekhar [123]. Numerical simulations for OR mechanism resulted in much smaller average void diameter when compared with the experimental results for annealing done in the temperature range 800-1200°C. Average void diameter calculated from M&C mechanism however showed a good match with the

experimental results. Thus, based on the numerical results reported by Evans and experimental results discussed above, it is reasonable to accept that M&C process dominates when annealing is done in the temperature range 800-1200°C for high dose He⁺ implantation cases.

3.4 keV versus MeV Implantation Energy

Increase of ion straggle in MeV He⁺ implants when compared to keV He⁺ implants raises the minimum dose that is required to produce voids. For example, for 1.6 MeV He⁺ implants in Si, the minimum He⁺ dose is reported to be $2 \times 10^{16} \text{ cm}^{-2}$ [102], whereas for 20 keV He⁺ implants, the minimum dose required is $5 \times 10^{15} \text{ cm}^{-2}$ [99]. The increase of straggle in MeV implants also increases the cavity layer width. The cavity size distribution also shows different behaviours for keV and MeV He⁺ implants. For example, Godey *et al.* [102] reported that upon annealing at 800°C for 30 min, 1.6 MeV, $5 \times 10^{16} \text{ cm}^{-2}$ He⁺ implant results in almost homogeneous size distribution of spherical cavities, whereas, 40 keV, $5 \times 10^{16} \text{ cm}^{-2}$ He⁺ implant results in spherical shaped cavities that increase in size with the increase in depth, the largest cavities are produced at the end of range of He⁺ implantation. During MeV He⁺ implantation, cavities are formed deep inside the sample so the surface has less influence on the cavity formation process. Due to the increase in the distance between the surface and the cavity layer, He effusion from the bubbles is suppressed. Godey *et al.* [102] calculated the He concentration in the samples by non Rutherford elastic backscattering (NREBS) process and reported that after annealing is carried at 800°C for 1000 sec, 90% He remains in the cavities for implantation done at 1.6 MeV. The authors reported that the previous works with 40 keV

implantation energy resulted 20% He remaining in the cavities for similar annealing condition.

Cavity formation by MeV implant is always associated with the formation of dislocation loops [102], [124]-[126]. It was mentioned before that for 1.6 MeV implantation energy, a minimum He⁺ dose of $2 \times 10^{16} \text{ cm}^{-2}$ is required to form cavities. Thus, a dose of $5 \times 10^{16} \text{ cm}^{-2}$ can be considered as high dose, which forms homogeneous distribution of spherical cavities along with the presence of dislocations upon high temperature annealing [102],[126]. Annealing performed at 800°C for 1020 min, however, is capable to completely dissolve the dislocation loops [124].

A different cavity evolution route is seen for MeV He⁺ implantations done with the minimum dose required to form cavities. Oliviero *et al.* [82], [126] reported cavity formation during 1.6 MeV, $2 \times 10^{16} \text{ cm}^{-2}$ He⁺ implantation in Si. The average diameter of the as-implanted bubbles is reported to be close to 3 nm with a density of $2 \times 10^{16} \text{ cm}^{-3}$, with no extended defects observed [126]. Annealing performed at 800°C for 30 min results in formation of randomly distributed cavity clusters. The cavity clusters contain a central large cavity surrounded by smaller cavities, which is similar to the planetary arrangement of cavities found in medium dose regime of keV He⁺ implantation. The cavities in the clusters are spherical in shape. Dislocations are seen to emit from cavity clusters towards the bulk and the surface. It is believed that the high pressure of He inside the cavities is released by the loop punching process, which creates these dislocations.

The dose rate plays an important role in the cavity evolution process for the above mentioned case that forms clusters of cavities [126]. With a high dose rate

($1.3 \times 10^{13} \text{ cm}^{-2}\text{s}^{-1}$), point defects have insufficient time to recombine with each other, thus facilitating the creation of a high concentration of stable bubbles in a continuous layer. At a very low dose rate ($2.5 \times 10^{12} \text{ cm}^{-2}\text{s}^{-1}$), not enough vacancies are available to produce a continuous layer of bubbles. At an intermediate dose rate ($8.3 \times 10^{12} \text{ cm}^{-2}\text{s}^{-1}$), a relatively small amount of vacancies is produced, which results in formation of highly pressurized He_mV_n complexes. These first evolve into platelets then forms planetary arrangement of bubbles. Though the role of the dose rate has been reported for high energy He^+ implants, the same arguments can be extended to low energy He^+ implants.

3.5 Role of Implantation Temperature

Both He and vacancies are important for the formation of the initial He_mV_n clusters during the He^+ implantation process. He can effuse out from the lattice during the implantation process itself when the implantation temperature is increased. At the same time, increase in implantation temperature can increase the dynamic annealing process thus reducing the concentration of vacancies available to contribute towards the initial He_mV_n cluster formation. The decrease in He and vacancies in the lattice with the increase in implantation temperature thus increases the threshold implantation dose for void formation.

For Si implanted with 50 keV, $5 \times 10^{16} \text{ cm}^{-2} \text{ He}^+$ (high dose regime), a comprehensive study of the role of implantation temperature has been reported by David *et al.* [127]. Increase in implantation temperature from room temperature (RT) to 200°C decreases the density of as-implanted bubbles with average bubble diameters remaining constant. Increase in implantation temperature increases dynamic annealing, thus a lower

number of vacancies are available to form the initial He_mV_n clusters. This results in the decrease of the bubble density. At 300°C, He becomes mobile. At higher temperatures, He_mV_n clusters become mobile, which can interact with other clusters to form bigger clusters. This results in increased bubble diameters for implantation temperatures up to 600°C when compared with the same for implantation temperatures from RT to 200°C. It was reported that for 50 keV, $5 \times 10^{16} \text{ cm}^{-2}$ He^+ implanted at 800°C, only 0.01% He remains in the sample after the implantation is done [127]-[128]. No as-implanted bubbles were noticed and only extended interstitial type defects were formed [127]-[128]. Increasing the He^+ implantation dose and energy (190 keV, $7.5 \times 10^{16} \text{ cm}^{-2}$), however, is capable to produce as-implanted bubbles when implantation temperature is 800°C [129]. Increase in dose increases the vacancy supply and the increase in implantation energy increases the amount of He retained in the cavity layer. Both these features result in as-implanted bubble formation. Multi-energy implantation of He^+ also increases the supply of both vacancies and He, and can form as-implanted bubbles when implantation temperature is 800°C [129].

The characteristics of cavities formed in medium dose regime also strongly depend on the implantation temperature. Silva *et al.* [130] reported the role of implantation temperature in the range -196°C to 27°C for medium dose (40 keV , $1 \times 10^{16} \text{ cm}^{-2}$) He^+ implantation after a post implantation annealing at 800°C for 10 min was done. At -196°C, vacancies and interstitials are immobile, thus dynamic annealing between vacancies and interstitials is not an effective process. There is large number of vacancies available in the lattice, which contributes to the cavity formation during the post

implantation annealing. Thus, the total cavity volume after post implantation annealing done for implantation carried out at -196°C is greater than implantations done at higher temperatures, where dynamic annealing process is effective. Post implantation annealing carried out in the samples where He^+ implantation temperature was set in the range -140 to 27°C , produced plate like bubbles. The total cavity volume shows similar values in the entire implantation temperature range.

Though implantation done with medium dose He^+ at room temperature does not produce any as-implanted bubbles, increase in implantation temperature in the range 100 - 350°C is capable of doing that [131]-[132]. Increasing implantation temperature in the range 100 - 350°C increases the average diameter of as-implanted bubbles [131]-[132]. Due to the increase of dynamic annealing process with the increase in implantation temperature, the availability of vacancies to form He_mV_n clusters reduces. The formation of the as-implanted bubbles and the increase in the average bubble diameter with the increase in implantation temperature is thus a surprising finding. An alternative hypothesis for bubble formation is thus proposed to explain the nature of the as-implanted bubbles. With insufficient vacancy supply, the pressure of He inside the He_mV_n clusters increases. This may result in loop punching to relieve the pressure and at the same time bubble growth would occur. Extended defects of interstitials are thus always associated with the bubble layers. This process facilitates continuous increase in as-implanted bubble diameter with the increase in implantation temperature even with the decrease in the supply of vacancies to form the He_mV_n clusters. For implantations done up to 200°C , during post implantation annealing, He effuses out from the bubbles, extended defects of

interstitials dissociate and recombine with the voids, and this results in the annihilation of voids and extended defects of interstitials [132]. Post implantation annealing done for samples implanted at 350°C slightly decreases the size of the voids and a large network of dislocations are present in the void layer [132]. A fraction of interstitials recombine with the voids to decrease their size and the rest of the interstitial recombine at the surface of the sample. Earlier, Trinkaus [133] argued in support of bubble growth occurring by dislocation loop punching in metal during limited vacancy supply condition. Loop punching has also been reported to occur in Si during MeV implantation cases as we have discussed before. Due to suppressed He effusion for MeV implantation situation, the pressure inside the bubbles tends to build up, which is relieved by the loop punching process. Thus loop punching may occur if either of the two conditions are available: (i) limited availability of vacancies, which may result in increase in He pressure inside the bubbles or (ii) suppressed He effusion from the bubbles increasing the He pressure inside bubbles.

Surprisingly, Raineri and Saggio [134] reported that for Si implanted with 80 keV, $2 \times 10^{16} \text{ cm}^{-2} \text{ He}^+$, void formation is inhibited, when substrate temperature is between 10 and 90°C and above 150°C. This clearly contradicts the results reported in refs. [130]-[132]. Further studies are thus necessary to understand the role of implantation temperature on the void evolution process particularly in medium dose He^+ implantation conditions.

3.6 Effect of Pressure

Enhanced hydrostatic pressure applied during annealing of He⁺ implanted Si shows a significant effect on the void evolution process [135]-[137]. Enhanced pressure reduces the rate of He effusion and results in partially filled bubbles after high temperature annealing is performed. He filled cavities may remain in highly pressurized state after annealing and can create strain in the surrounding lattice [135]. When compared with cavities formed during high temperature annealing at atmospheric pressures, Misiuk *et al.* [135] reported that bubbles with smaller diameters are formed if a similar annealing schedule is applied under higher pressure. The authors, however, did not explain the reason behind getting smaller cavity diameter. To our understanding, slower He effusion from the cavity layer reduces the rate of the migration and coalescence process causing smaller sized cavity formation.

Interestingly, Bak-Misiuk *et al.* [137] later reported contradictory arguments and results. When comparing with cavities formed under atmospheric pressure, the authors reported formation of larger cavities after annealing carried out at high temperature under higher pressure and argued for the Ostwald ripening mechanism to be dominant. Due to the lower He effusion rate, He filled bubbles are in highly pressurized state. The increase in bubble diameter is then a favourable process to relieve the pressure. The authors mentioned that in presence of He, enhanced pressure decreases divacancy formation energy. The decrease in the rate of He out-diffusion thus promotes formation of a greater number of bubbles. Due to the contradictory findings, further studies are needed to study the role of enhanced pressure on the cavity evolution process.

3.7 Effect of Anneal Ramp Rate

Simpson and Mitchell [100] reported that for Si implanted with 1 MeV He⁺, ramp rate of rapid thermal annealing for annealing done for 5 min at 700°C in dry N₂ can significantly affect the void evolution process and can facilitate formation of voids for doses lower than the critical dose. We can see from Table 3.1 that for He⁺ implantation done at 1 MeV, the minimum dose required to form voids is 1.5×10^{16} cm⁻². However, Simpson and Mitchell reported that anneal ramp rate of 3°C/sec can lower the He⁺ dose to 5×10^{15} cm⁻² to form cavities. Scanning electron microscopy (SEM) images of sample cross sections show planetary like cavity formation. Increasing the anneal ramp rate to 30°C/sec increases the size of the central bubble of the planetary arrangement. Increasing the anneal ramp rate to 100°C/sec results in stable bubble formation even for He⁺ implantation dose of 3.5×10^{15} cm⁻². It was mentioned that increase in anneal ramp can lead to He retained in the samples after annealing at 700°C for He⁺ implantation dose as low as 3.5×10^{15} cm⁻². The possibility of a decrease in the dynamic annealing process due to an increase in anneal ramp rate will supply additional vacancies to form cavities for He⁺ implantation at doses lower than the critical value.

3.8 Cavity Formation by Hydrogen Implantation

Cavities can also be formed by H⁺ formation and subsequent annealing [91], [138]. While He being an inert gas does not react with the Si lattice, H₂ on the other hand forms compounds with the Si lattice. Hydrogen, in its atomic and molecular states reacts with Si surface, impurities, point defects and point defect clusters. The cavity formation

process by H^+ implantation is thus much complexed process when compared with cavity formation by He^+ implantation. The main application area of cavity formation by H^+ implantation reported in literature is in production of silicon on insulators. The principle of forming SOI is to form fractures inside Si by H^+ implantation and subsequent annealing. The fracture formed inside the wafer leads to cleavage of the wafer. Implantation with H^+ produces hydrogenated multi-vacancy structures in Si. During annealing performed in the temperature range 200-350°C, multi-vacancy structures emit hydrogen in form of H_2 and at the same time the multi-vacancy structures transform to cavity structure [138]. These cavity structures capture the formed H_2 . During annealing done above 400°C, any mono-vacancies created during the process coalesce to form platelets with H terminated internal (111) and (100) surfaces. Molecular H_2 are also accumulated inside these platelets [138]. Trapped H_2 builds up internal pressure inside the cavities which leads to crack formation and generates cleavage during SOI formation. In an unconstrained wafer surface typically blisters are formed instead of forming wafer cleavage. The governing phenomenon that leads to wafer cleavage formation is that molecular hydrogen formed during the cavity evolution process remain inside the cavities, which build the internal pressure leading to exfoliation of the wafers. If the H^+ implantation dose is lower than $2 \times 10^{16} \text{ cm}^{-2}$, the density of cavities are small to capture all the formed H_2 , thus H_2 can escape from the sample. In this situation exfoliation of the wafers do not occur.

Chapter 4

Void Formation in Si and $\text{Si}_{1-x}\text{Ge}_x/\text{Si}$ by He^+ Implantation

This chapter describes the details of the experimental studies carried out to form voids in Si and in Si with a $\text{Si}_{1-x}\text{Ge}_x$ epilayer ($\text{Si}_{1-x}\text{Ge}_x/\text{Si}$). We relied extensively on transmission electron microscope (TEM) images to study the void characteristics. We report the role of the $\text{Si}_{1-x}\text{Ge}_x$ epilayer on the void formation process in Si. We also report the influence of the annealing ambients, N_2 and dry O_2 , on the void evolution mechanism in Si and $\text{Si}_{1-x}\text{Ge}_x/\text{Si}$ samples. Similar to the previous chapter, we refer to He-filled vacancy clusters as bubbles, whereas the term “voids” refers to empty vacancy clusters. We use the term “cavity” to refer either bubble or void.

4.1 Experimental Details

He^+ implantations were performed into Czochralski grown {100} Si wafers, Si wafers having a 60 nm $\text{Si}_{0.95}\text{Ge}_{0.05}$ epilayer ($\text{Si}_{0.95}\text{Ge}_{0.05}/\text{Si}$) and Si wafer with a 20 nm $\text{Si}_{0.91}\text{Ge}_{0.09}$ epilayer ($\text{Si}_{0.91}\text{Ge}_{0.09}/\text{Si}$). The thickness of the $\text{Si}_{1-x}\text{Ge}_x$ ($x = 0.05, 0.09$) epilayer is below the critical thickness beyond which the epilayer tends to relax and forms dislocations in the structure [6]. Thus the $\text{Si}_{1-x}\text{Ge}_x$ layer remained under compressive strain even after performing high temperature annealing. He^+ implantation energy was 30

keV and the implantation dose was $5 \times 10^{16} \text{ cm}^{-2}$. According to the Monte Carlo based ion implantation simulator Crystal TRIM [9], for this He^+ implantation condition in Si, the He^+ projected range is 300 nm. The peak of the vacancy profile is at the depth of 250 nm from the sample surface. The implantation energy was set to 30 keV to ensure that He^+ projected range remains inside Si for the $\text{Si}_{1-x}\text{Ge}_x/\text{Si}$ samples. These implantation conditions place the peak of the He^+ implanted profile at a depth of approximately 240 nm from $\text{Si}_{0.95}\text{Ge}_{0.05}/\text{Si}$ interface. The implantations were done at room temperature. He^+ implantation beam was fixed 7° off to the axis to minimize the channelling during the implantation process.

After the implantations were done, samples were cleaved into small pieces of approximately 1x1 cm. Si and $\text{Si}_{0.95}\text{Ge}_{0.05}/\text{Si}$ samples were furnace annealed (FA) in the temperature range 960-1110°C for 30 min both in N_2 and dry O_2 ambients. One set of samples underwent anneals at 1050°C for 15 min in a rapid thermal annealing (RTA) chamber both in N_2 and dry O_2 ambients. To calibrate the actual anneal temperature, for anneals in oxidizing ambient we included a reference Si piece, and for anneals in inert ambient we annealed a small piece of Si in dry O_2 immediately following each anneal. We then measured the oxide thickness by ellipsometry and used the Deal and Grove model [2] for dry oxidation kinetics of Si to determine the actual anneal temperature.

For Si, annealing in dry O_2 oxidizes the surface of the sample and injects interstitials. For SiGe oxidation, the behaviour is considerably more complicated. Depending on the anneal conditions the oxide formed may be a pure SiO_2 [139]-[140], a mixed $(\text{SiGe})\text{O}_2$ [139]-[140], or a sequence of different layers [141]. In some cases a Ge-

rich layer forms at the oxidizing interface [29],[140]-[142]. In others, no such layer is formed [143]-[145]. As to the behaviour of point defects, some studies have indicated that interstitial injection is suppressed [141]-[142], [146]-[147]. However there remains ambiguity in the data regarding whether such reduction occurs. For the studies that indicate such suppression, there is no agreement on the underlying mechanism, and there is no agreement on whether interstitial injection is suppressed from the oxidizing interface or deeper as the transition from SiGe to Si takes place. Annealing Si in nitrogen is considered to be annealing in inert ambient as Si does not react with nitrogen up to 1150°C [65]. However, above 1150°C, it is reported that a silicon nitride layer is formed on top of {111} Si, and further that this nitridation process injects vacancies [65]. We performed energy dispersive x-ray (EDX) line scans on the surface of our Si_{0.95}Ge_{0.05}/Si samples after these were annealed in N₂ at 1110°C. EDX line scan results did not provide evidence for any nitride formation on the Si_{0.95}Ge_{0.05} epilayer. While this rules out vacancy injection due to nitridation, it does not eliminate the possibility of other surface mechanisms due to the strain in the structure.

To study the behaviour of voids in the samples we prepared cross-sectional transmission electron microscope (XTEM) samples following the conventional method. XTEM images were taken using a Philips CM12 electron microscope operating at 120 kV or using a JEOL 2010 electron microscope operating at 200 kV. From the XTEM images, we calculated the average void diameter and the average void density for each sample.

4.2 Experimental Results and Discussions

Previous studies available in the literature report that for high dose ($> 10^{16} \text{ cm}^{-2}$) He^+ implantation in Si, the as-implanted samples contain cavities of 2-5 nm in diameter. XTEM images taken on the as-implanted Si samples implanted with 30 keV, $5 \times 10^{16} \text{ cm}^{-2}$ He^+ in this study also show that cavities are already formed in the sample.

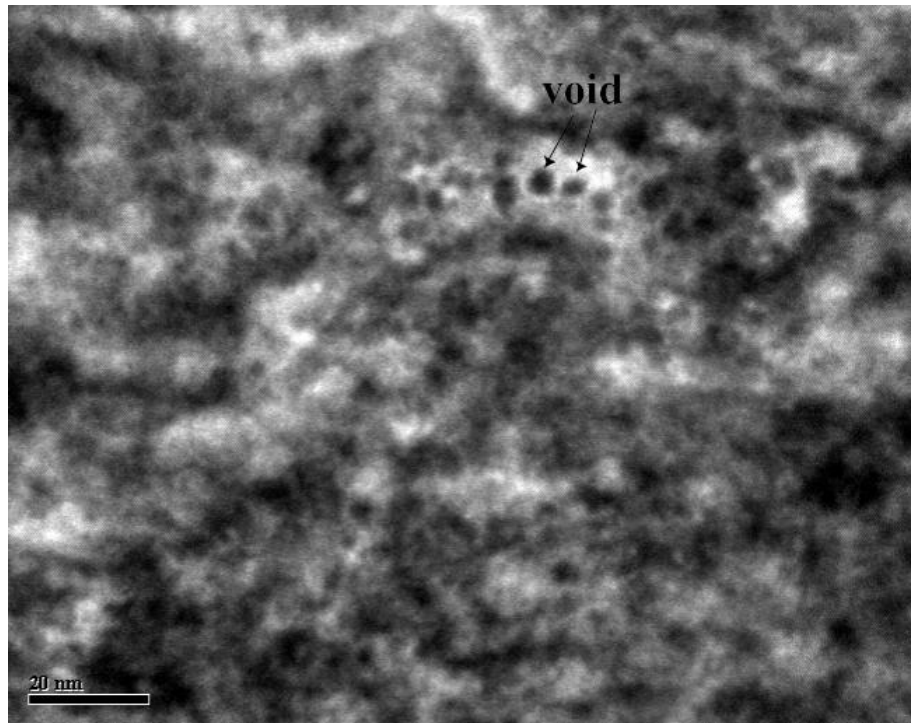
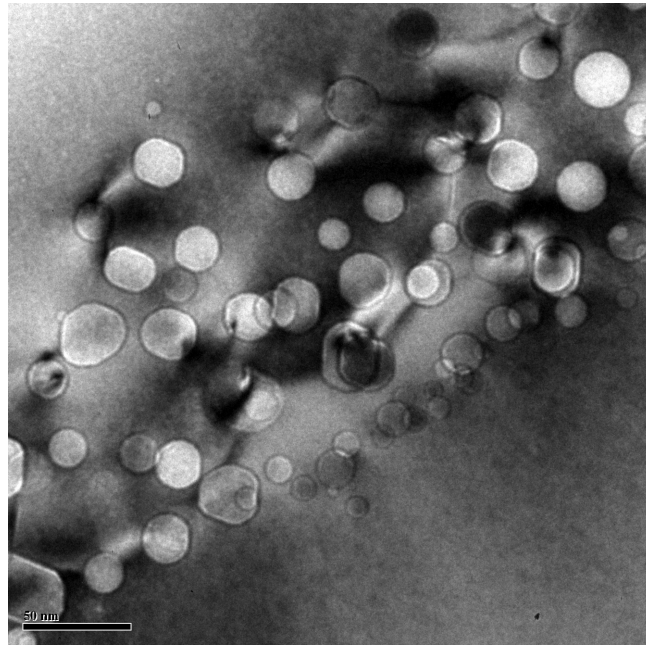


Figure 4.1. XTEM image of as-implanted Si sample implanted with 30 keV, $5 \times 10^{16} \text{ cm}^{-2}$ He^+ . Images taken with JEOL 2010 electron microscope operating at 200 kV.

From XTEM images, we observed void formation in all cases. Figures 4.2-4.5 show typical TEM images taken by the Philips CM12 electron microscope for voids formed in Si and Si_{0.95}Ge_{0.05}/Si samples for anneals done in N₂ and dry O₂ ambients. We note the presence of threading dislocations in the area where voids are formed. No dislocations are present beyond this area. This confirms that the Si_{0.95}Ge_{0.05} epilayer remains under compressive strain after the anneal. The dislocations originate and terminate on a void. Figure 4.6 shows a high-resolution XTEM image showing dislocations associated with voids. We observe dislocations associated with the void layer in all samples.

Roqueta *et al.* [92] in their study also reported the presence of dislocations and {311} defects in the void layer after high temperature annealing was done for Si implanted with 40 keV He⁺ with doses of $5 \times 10^{16} \text{ cm}^{-2}$ and $1 \times 10^{17} \text{ cm}^{-2}$. In our annealed samples, dislocations are only associated with large voids. One possible explanation of formation of dislocations in the void band can be the strain created in the lattice by the voids [95]-[96]. Since the dislocations are associated with large voids, any dissociation of interstitials from the dislocation will not make a noticeable reduction in the void diameter as the number of interstitials required to reduce the radius (r) of a void increases as a function of r^2 .

(a)



(b)

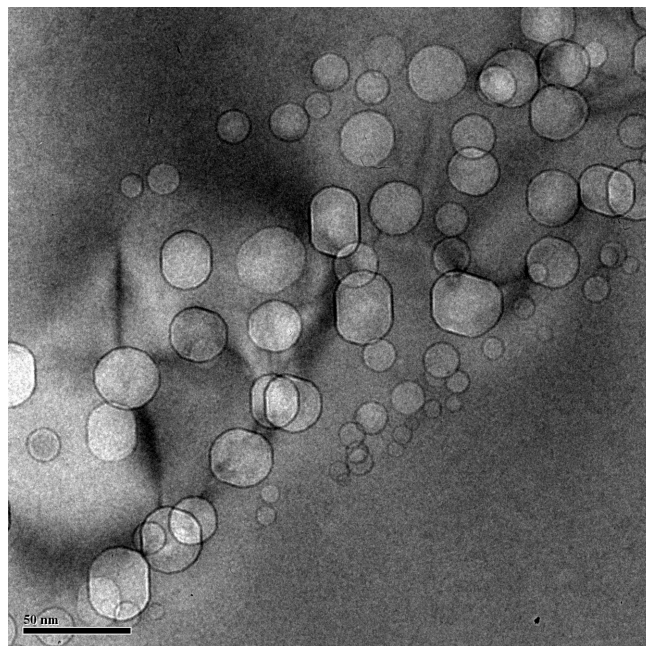
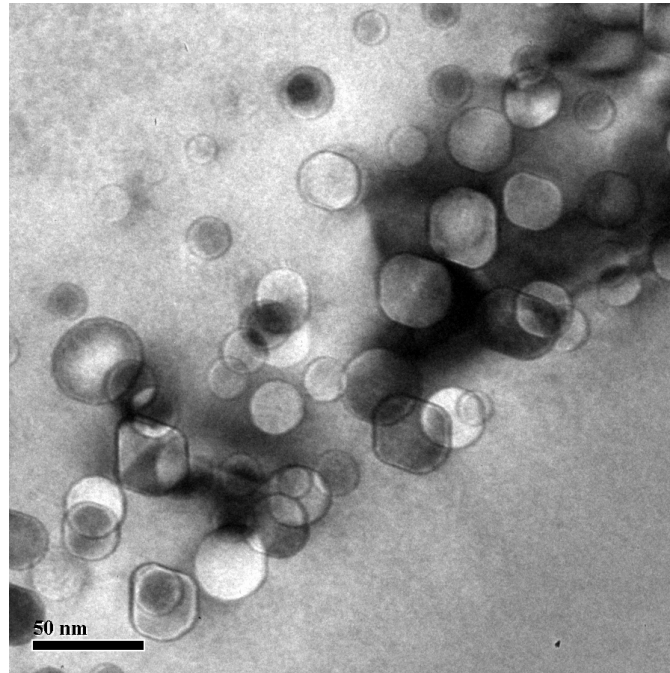


Figure 4.2. XTEM images for Si samples annealed in RTA at 1050°C for 15 min in (a) N₂ and (b) dry O₂.

(a)



(b)

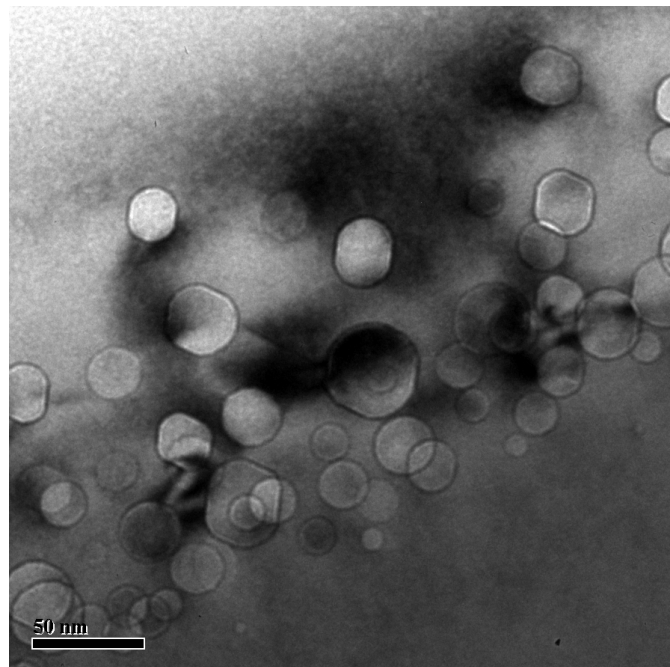
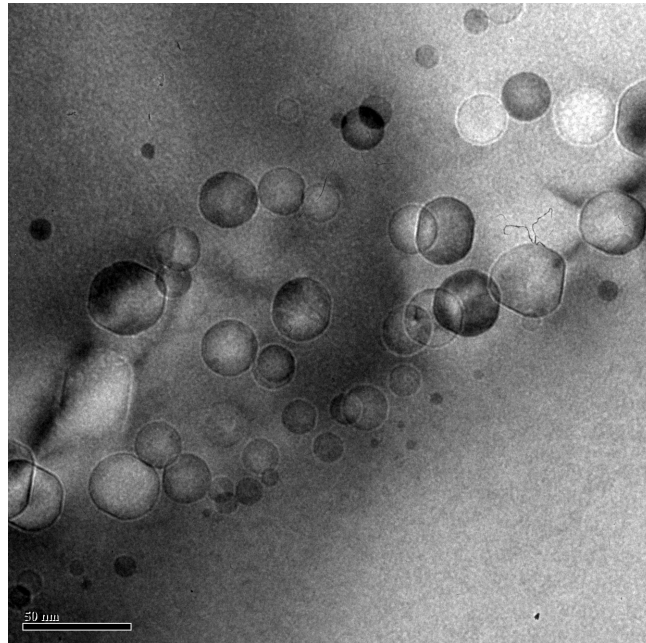


Figure 4.3. XTEM images for $\text{Si}_{0.95}\text{Ge}_{0.05}/\text{Si}$ samples annealed in RTA at 1050°C for 15 min in (a) N_2 and (b) dry O_2 .

(a)



(b)

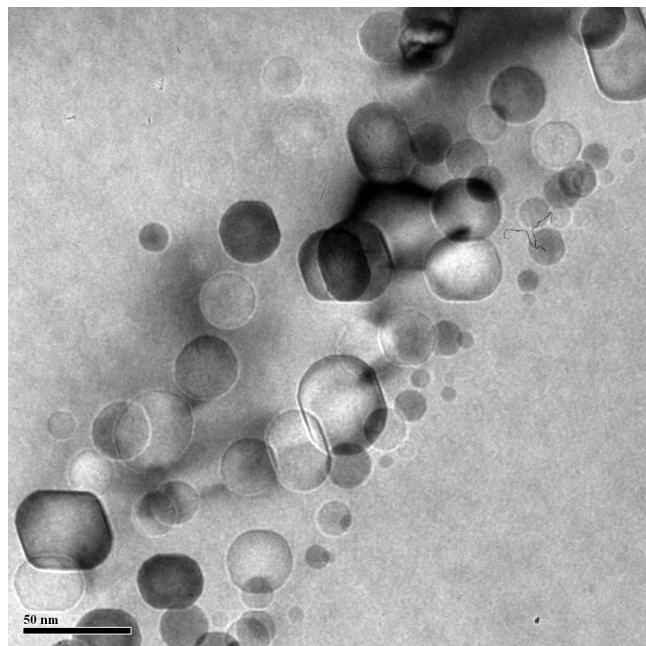
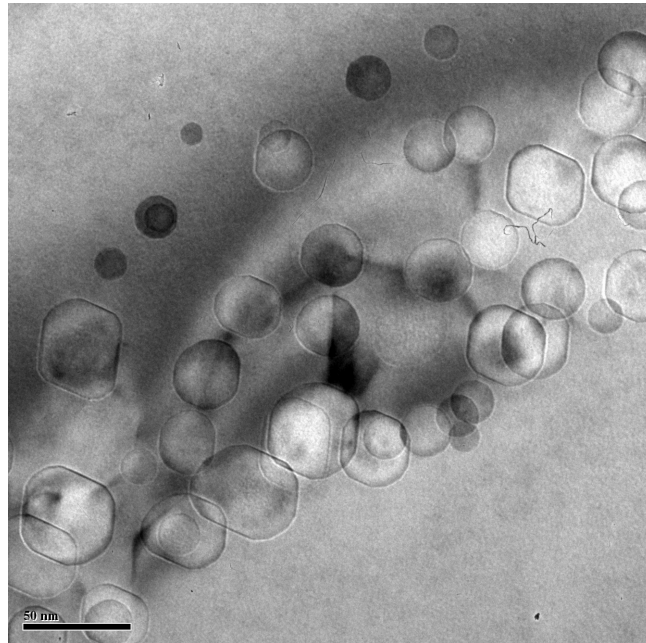


Figure 4.4. XTEM images for Si samples annealed in FA at 1080°C for 30 min in (a) N₂ and (b) dry O₂.

(a)



(b)

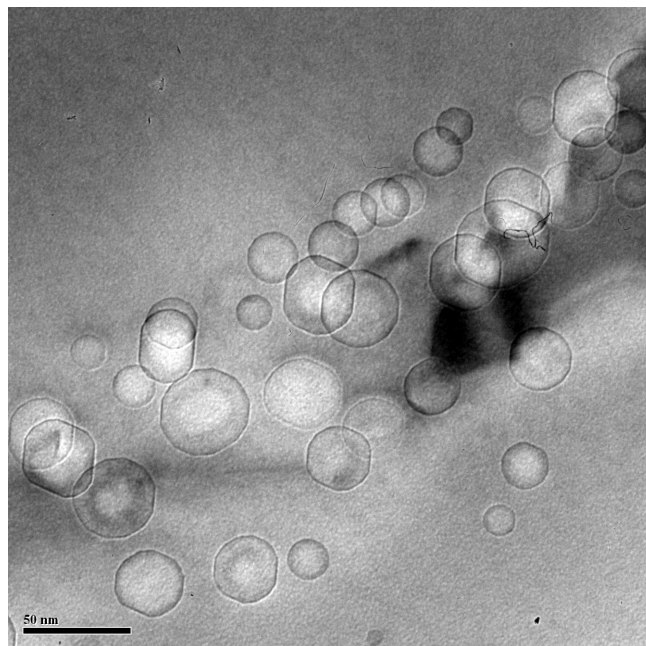


Figure 4.5. XTEM images for $\text{Si}_{0.95}\text{Ge}_{0.05}/\text{Si}$ samples annealed in FA at 1080°C for 30 min in (a) N_2 and (b) dry O_2 .

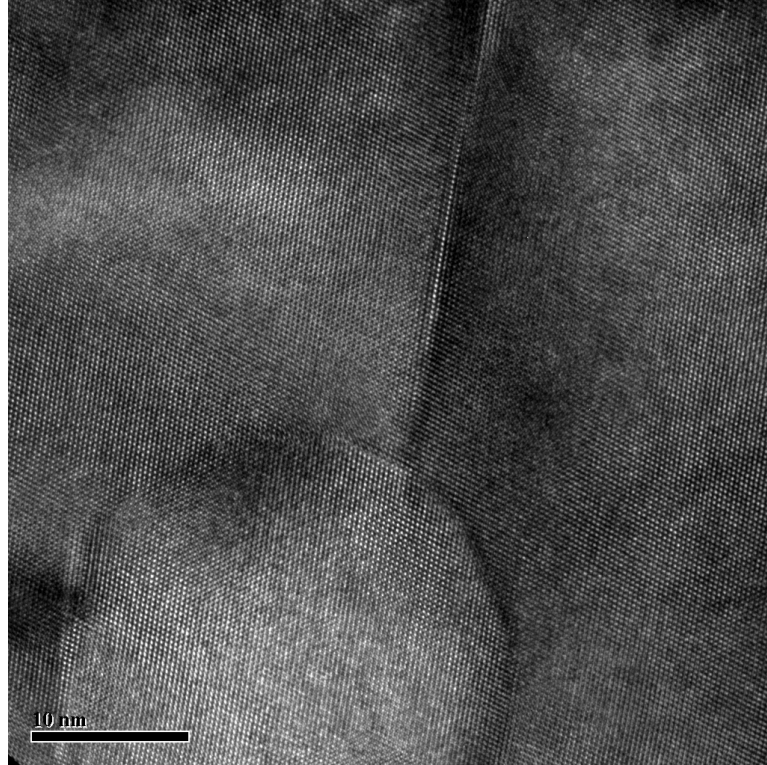


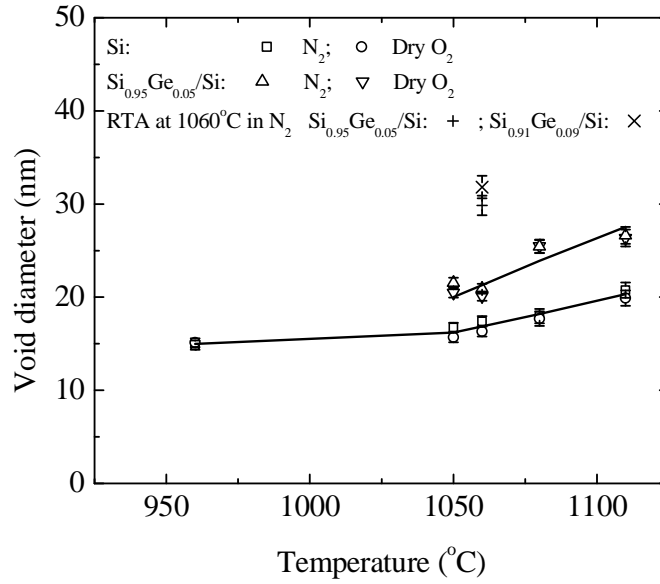
Figure 4.6. XTEM image showing dislocation associated with a void. Image taken with JEOL 2010 electron microscope operating at 200 kV.

We measured the average void diameter and average void densities for all our samples taking into account at least 650 voids in each case to ensure that our calculated values accurately reflect differences between different process conditions. The void density calculated from the TEM images is in fact an areal density (unit is cm^{-2}). We measured TEM sample thicknesses at various locations in the samples by electron energy loss spectroscopy (EELS) using a JEOL 2010 electron microscope. We calculated the average sample thickness and divided the areal density by the average sample thickness to obtain an average volume density (unit is cm^{-3}) of voids. Figure 4.7 shows the variation of

average void diameter and average void density as a function of annealing temperature for our samples. The solid lines in the figures are merely guides for the eye. Figure 4.7 includes data from the measurements described thus far plus data points for void growth in an RTA anneal, for which we give a separate discussion later in this Section (see p. 68 onwards). Void evolution is believed to be governed by a migration and coalescence process [103]. With the increase in the annealing temperature, the rate of the migration and coalescence process increases, thus increasing the average void diameter and decreasing the average void density as we have observed from our experimental results. For Si samples, similar trends have also been reported by other authors [11], [99].

From our experimental results, the values of average void diameter and average void density for annealing done in N₂ and dry O₂ ambients are similar. Annealing Si in dry O₂ injects interstitials from the Si surface towards the bulk, but this does not appear to make a difference to void evolution in our samples. We can understand this given the dynamics of the process. Conceptually we can consider two stages of growth. During the first stage, the number of free interstitials due to implant damage would overwhelm any contribution due to oxidation. The peak concentration of free interstitials in the as-implanted sample is $1.1 \times 10^{22} \text{ cm}^{-3}$, which occurs inside the cavity layer. This concentration is very high compared to the equilibrium interstitial concentration (for example, at 1080°C equilibrium interstitial concentration is $6.06 \times 10^{13} \text{ cm}^{-3}$) [9]. The presence of He in the cavities stabilizes them against recombination with interstitials. At 1080°C, we expect the free interstitial concentration to decrease very rapidly due to annealing, which causes interstitials either to diffuse to the surface and recombine or to

(a)



(b)

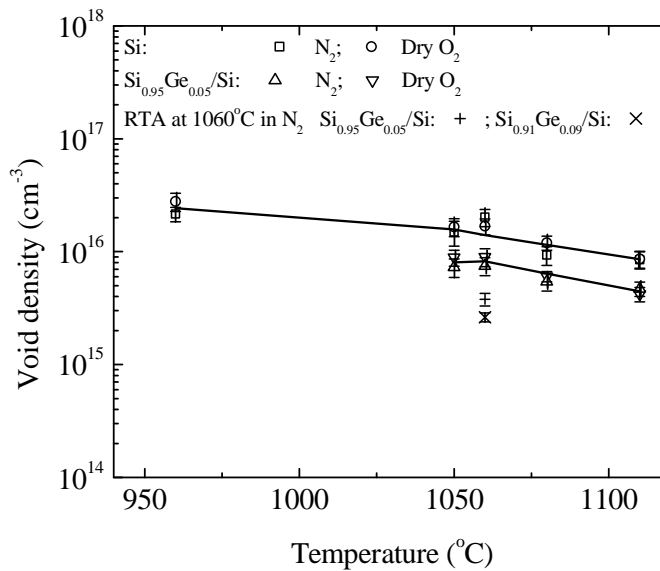


Figure 4.7. Variation of average void diameter and average void density in Si and Si_{1-x}Ge_x/Si (x = 0.05, 0.09) samples as a function of annealing temperature. Solid lines through the data point act as guide to the eyes.

form extended defects in the bulk. Simulations using FLOOPS-ISE [9] predict that the free interstitial concentration drops to nearly its equilibrium value within 30 sec.

Thus, after a very short time, there do not remain free interstitials in sufficient concentrations to cause the voids to shrink. As already pointed out, during this initial brief period, cavities are still filled up with He. In the second stage of the anneal, because the initial implant damage has been annealed out, the only free interstitials in the sample would be those supplied by oxidation. A quantitative estimate can be obtained again from FLOOPS-ISE simulation, which predicts that dry oxidizing anneal done for 30 minutes at 1080°C results in $5.13 \times 10^{14} \text{ cm}^{-3}$ interstitials reaching the cavity layer. This is approximately six orders of magnitudes lower than the number of vacancies in voids and hence is unlikely to have a significant impact on void size. The foregoing discussion applies to the Si samples. Annealing $\text{Si}_{1-x}\text{Ge}_x$ in dry O_2 suppresses the amount of interstitial injection when compared with interstitial injection during dry oxidation of Si [147]. Hence, the arguments given above in comparing anneals done in N_2 and dry O_2 ambients for $\text{Si}_{0.95}\text{Ge}_{0.05}/\text{Si}$ samples apply with even greater force.

While anneal ambient does not appear to have a significant effect, the comparison of Si and $\text{Si}_{0.95}\text{Ge}_{0.05}/\text{Si}$ samples is more interesting. For $\text{Si}_{0.95}\text{Ge}_{0.05}/\text{Si}$ samples, in all the cases, the average void diameter is greater and the average void density is lower than those in Si. This is particularly noteworthy since voids in both cases are being formed in Si. We applied the two sample t test to check the validity of the difference in the calculated average void diameter between Si and $\text{Si}_{0.95}\text{Ge}_{0.05}/\text{Si}$ samples. The the process is described in Appendix A. In $\text{Si}_{0.95}\text{Ge}_{0.05}/\text{Si}$ samples, the $\text{Si}_{0.95}\text{Ge}_{0.05}$ epilayer remains

under compressive strain. Thus, Si very close to the $\text{Si}_{0.95}\text{Ge}_{0.05}/\text{Si}$ interface remains under tensile strain. However, the tensile strain in Si is expected to remain confined very close to the $\text{Si}_{0.95}\text{Ge}_{0.05}/\text{Si}$ interface since the elastic constants of $\text{Si}_{1-x}\text{Ge}_x$ are lower than those in Si and the strain in the Si is expected to decay very rapidly as we move away from the interface. However, at the anneal temperatures considered in the experiments, significant amount of Ge interdiffusion can occur [40]-[41], [148]. The implantation damage created during He^+ implantation may further aid the interdiffusion of Ge. For the experimental conditions considered here we applied the Si-Ge interdiffusion model reported in ref. [40]. For the He^+ implantation dose and energy considered in our study we calculated the concentrations of vacancies and interstitials from Crystal TRIM simulation of FLOOPS-ISE. We took into account the dynamic annealing process of the damage created during ion implantation process and considered that 5.5% vacancies and interstitials remain after the ion implantation process is completed. This was chosen as the mid point of the range (1-10%) suggested by Knights *et al.* [50]. We used these profiles as the initial vacancy and interstitial profiles in the Si-Ge interdiffusion model. Figure 4.8 shows the Ge interdiffusion profile predicted for annealing done at 1050° for 30 min.

We notice that Ge in $\text{Si}_{0.95}\text{Ge}_{0.05}/\text{Si}$ samples can interdiffuse inside Si and reach the cavity layer. Ge reaching the cavity layer at sufficient concentrations can affect the void evolution process. One possibility relates to the weaker Si-Ge bond compared to the Si-Si bond. A reduced average bond strength in the cavity layer may enhance the surface diffusion of adatoms along the internal void surface and can thus result in larger voids. Another possibility can be the presence of a stress gradient due to the presence of Ge

concentration gradient in the sample. As the Ge interdiffusion process proceeds, the interface where the transition between compressive and tensile strain occurs also moves

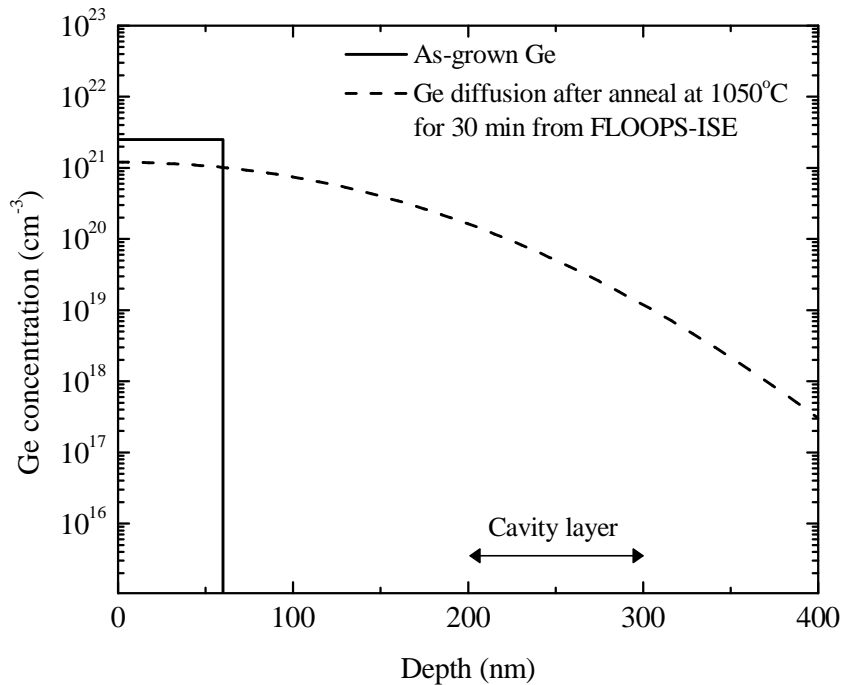


Figure 4.8. Ge interdiffusion after annealing for 30 min at 1050°C taking into account the damage created during 30 keV, $5 \times 10^{16} \text{ cm}^{-2}$ He⁺ implantation.

towards the bulk so that depending on the extent of interdiffusion the strain in the cavity layer may be either tensile or compressive. A stress gradient either tensile or compressive in nature can exert force on cavities and thus can result in enhanced cavity migration [149]. A stress gradient can also create non uniform vacancy concentration [150], which can result in a vacancy flow in Si, which can aid cavity migration. In short, Ge interdiffusion is likely to increase the rate of cavity migration either because of the modified bond strength, or a stress gradient, or both, and may therefore result in increased

void diameter in the $\text{Si}_{0.95}\text{Ge}_{0.05}/\text{Si}$ samples compared with the Si samples. Since void evolution occurs through a migration and coalescence process, any increase in void diameter will result in a decrease in void density, as we have observed in our $\text{Si}_{0.95}\text{Ge}_{0.05}/\text{Si}$ samples.

To test this hypothesis, we annealed $\text{Si}_{0.95}\text{Ge}_{0.05}/\text{Si}$ and $\text{Si}_{0.91}\text{Ge}_{0.09}/\text{Si}$ samples in RTA at 1060°C for 30 min in N_2 and we calculated the average void diameter and the average void density values for the samples. The calculated values are shown in Figure 4.7. The increase in Ge fraction in the $\text{Si}_{1-x}\text{Ge}_x$ epilayer was expected to result in an increased amount of Ge reaching the cavity layer, which thus enhances the bubble migration and coalescence process and increases the average void diameter. The results shown in Figure 4.7 confirm this. However, these results also indicate that void sizes as a result of an RTA are larger than those produced by furnace annealing. This is not surprising since He effusion would occur more rapidly in an RTA leading to larger voids and lower void densities. In Chapter 5 we provide a discussion on why faster He can cause this type of void evolution pattern.

Further study reveals another important difference between Si and $\text{Si}_{0.95}\text{Ge}_{0.05}/\text{Si}$ samples. Figures 4.9 and 4.10 show the distribution of void sizes for Si and $\text{Si}_{0.95}\text{Ge}_{0.05}/\text{Si}$ samples annealed at 1050°C and 1080°C . The shapes of the void size distributions of Si and $\text{Si}_{0.95}\text{Ge}_{0.05}/\text{Si}$ samples are quite different. While in $\text{Si}_{0.95}\text{Ge}_{0.05}/\text{Si}$ samples we find a distinct peak around the average void diameter in the void size distribution, in Si samples the void size distribution is almost uniform for quite a wide range of void sizes around the average void diameter. For all other temperatures, we observe similar type of void size

distribution for Si and Si_{0.95}Ge_{0.05}/Si samples as we have observed in Figures 4.9 and 4.10.

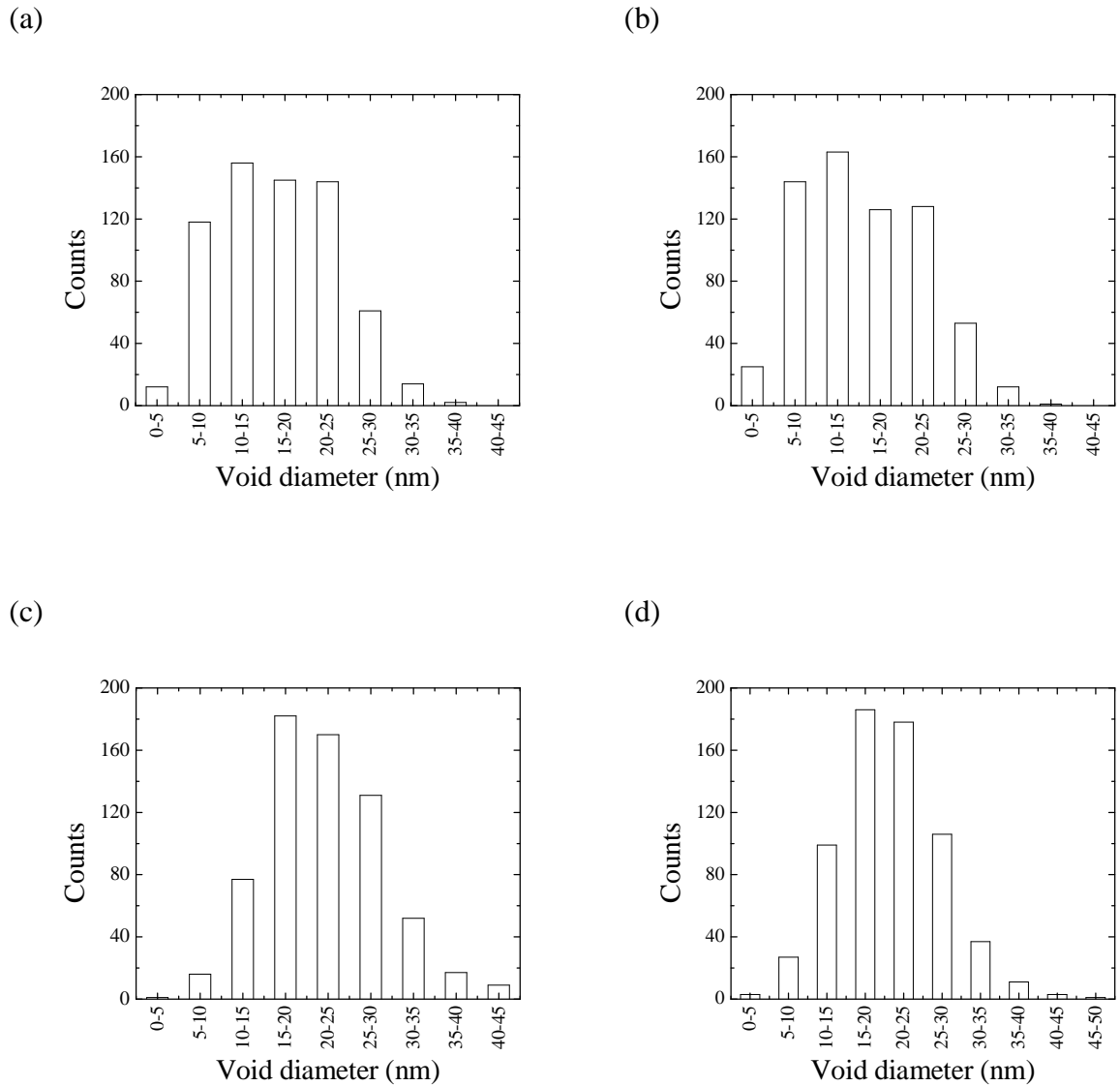


Figure 4.9. Void size distribution for annealing done in RTA at 1050°C for 15 min. Si samples annealed in (a) N₂ and (b) dry O₂. Si_{0.95}Ge_{0.05}/Si samples annealed in (c) N₂ and (d) dry O₂.

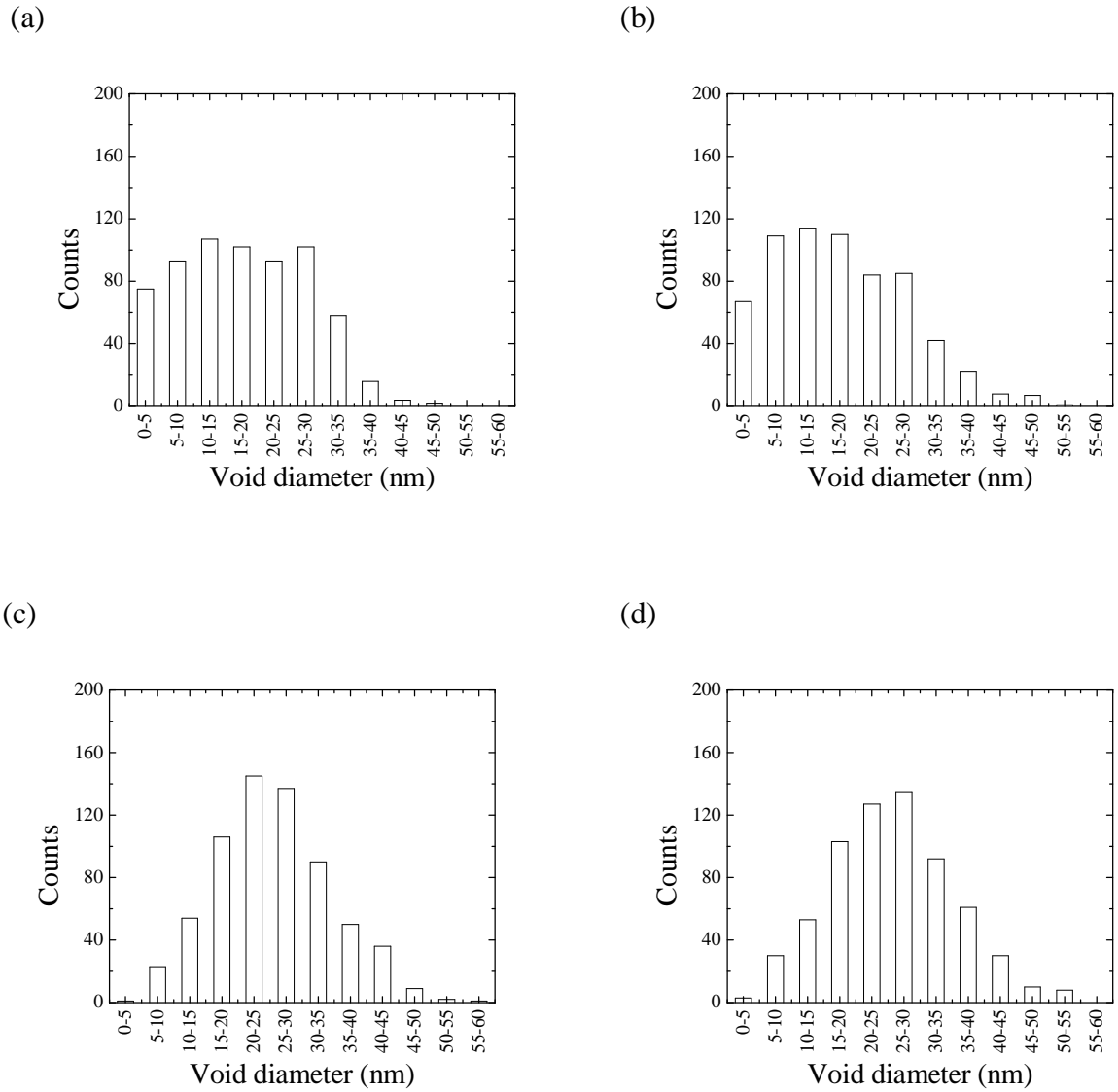


Figure 4.10. Void size distribution for annealing done in FA at 1080°C for 30 min. Si samples annealed in (a) N₂ and (b) dry O₂. Si_{0.95}Ge_{0.05}/Si samples annealed in (c) N₂ and (d) dry O₂.

Table 4.1. Standard deviation (SD) in nm for void size distribution

Temperature (°C)	Anneal type	Time (min)	SD (Si annealed in N ₂)	SD (Si annealed in dry O ₂)	SD (Si _{0.95} Ge _{0.05} /Si annealed in N ₂)	SD (Si _{0.95} Ge _{0.05} /Si annealed in dry O ₂)
960	FA	30	6.58	6.19	-	-
1050	RTA	15	6.78	7.00	6.88	6.65
1060	FA	30	7.42	7.13	6.81	6.51
1080	FA	30	10.04	10.11	9.06	9.19
1110	FA	30	10.80	10.83	11.80	11.86

Table 4.1 shows the calculated values of standard deviation of the void size distribution considering the actual size of all the voids measured from XTEM images. The standard deviation for samples annealed in N₂ and dry O₂ are quite similar, which we can expect from looking at the similar shapes of void size distributions for annealing done in N₂ and dry O₂. As the anneal temperature increases, larger sized voids are grown, and at the same time the width of the void size distribution increases, thus increasing the standard deviation. We do not attempt to compare the standard deviation values of Si and Si_{0.95}Ge_{0.05}/Si samples since the shape of the void size distribution in Si and Si_{0.95}Ge_{0.05}/Si samples are very different.

In conclusion, the presence of Si_{1-x}Ge_x epilayer on Si is capable of influencing the void evolution process in Si where voids are created by high dose He⁺ implantation and subsequent high temperature annealing. The presence of Si_{1-x}Ge_x epilayer increases the average void diameter and decreases the average void density when compared with the same in relaxed Si. We also find that the increase in Ge fraction in Si_{1-x}Ge_x epilayer can

increase the average void diameter and decrease the average void density. Due to the implantation damage created and the high temperature annealing, interdiffusion of Ge across $\text{Si}_{1-x}\text{Ge}_x/\text{Si}$ likely reaches the cavity layer. The weaker Si-Ge bond compared to Si-Si bond and the stress gradient introduced in the lattice due to the presence of Ge may increase the rate of cavity migration process, which is believed to govern the void evolution mechanism. The presence of Ge also results in void size distributions that are more selective than is the case in the absence of Ge. We also demonstrate that interstitial injection during oxidation does not appreciably affect void growth. This is likely because interstitial injection from the surface does not become the dominant source of free interstitials in the sample until later process times, by which time voids have grown to a large size compared with the available interstitial flux.

Chapter 5

A Mathematical Model for Void Evolution in Silicon

In this chapter, a mathematical model for void evolution in Si is proposed. The mathematical model is developed considering the physical mechanisms associated with the void evolution process. A physical justification of the proposed model is given and the parameters used in the simulation to match the simulated and experimental results are described. The model contains one empirically determined parameter that describes the rate of migration and coalescence of voids and a physical justification for this parameter is proposed. All other model parameters reflect physical quantities well documented in literature. The model is capable of matching a wide range of experimental data. The model efficiently highlights the physical mechanisms working behind the void evolution process.

5.1 Previous Attempts

A comprehensive attempt to model point defect clustering during ion implantation and subsequent annealing is reported in literature [151]-[153]. One of the cases where the model was applied was point defect clustering in Si by He⁺ implantation. In the proposed model, the only mobile species are He, vacancy, self-interstitial and interstitially

dissolved impurities. Defect clusters are formed by any possible combination of the above species by the processes of trapping and dissolution. Any combination of defect clusters is considered to remain immobile. Each of the mobile species and the defect clusters are represented with an individual continuity equation. To avoid solving equations for all the species, a Monte Carlo approach is applied to minimize the computational complexity. It was reported that the model is capable to simulate the critical dose required for void formation by He^+ implantation process. Below the critical dose, voids are not formed, whereas above the critical dose voids are formed after high temperature annealing is carried out. The simulations were done up to 827°C in refs. [151]-[152]. It was argued that there exists a competition between the outer surface and the stable vacancy clusters to capture vacancies. For implantation dose below the critical dose, the surface acts as a dominant sink for the vacancies, thus no void formation occurs after high temperature annealing is performed. On the other hand, when the implantation dose is set above the critical dose, stable vacancy clusters capture any dissociated vacancy and the high temperature annealing process forms voids. It was further mentioned that for cavities to form, the diffusion length of vacancy in the damage layer must be much smaller than the distance to the surface. These arguments for justifying the critical dose for the formation of cavities are puzzling and do not agree with the explanations given in literature describing the reason behind cavity formation above the critical dose, which we have discussed in Chapter 3. Further, the cavities were considered to remain immobile in the model. This is a major drawback of the model, since Evans [103] has effectively demonstrated that (at least in the high dose implant regime) the migration and

coalescence mechanism is the dominant process for cavity evolution for annealing up to 1000°C and Ostwald ripening (OR) process plays no role in the cavity evolution process.

The success of a mathematical model certainly depends on its capability to describe the experimental results accurately. The simulation results reported in refs. [151]-[152] showed that for annealing done above 527°C, both cavity diameter and cavity density remains constant up to 827°C. 827°C was the highest temperature considered in the simulation. The general trend reported in the literature is that with increasing anneal temperature the cavity diameter increases and the cavity density decreases. The simulations results reported in refs. [151]-[152] clearly do not follow this trend. Further, there is no published report showing any comparison between experimental and simulation results when the proposed model is applied for void evolution by He⁺ implantation in Si. To date this had been the most complete model describing void evolution in silicon. The deficiencies summarized above clearly indicate the need for a more effective model. Our approach is to begin with a model that has been successfully used to model average size and density of interstitial clusters ($\{311\}$ defects) [154] and then to adapt that to modeling void evolution by directly relating the mathematical model to the accepted description of the physical processes that govern void evolution. We emphasize a correspondence between mathematical formulation and physical description so that our model not only fits the data but yields insight into the void evolution process and its dependence on various experimental factors.

5.2 Cavity Migration and Coalescence Process

The cavity migration occurs by diffusion of atoms from the leading edge to the trailing edge of the cavity. There are mainly three possibilities by which the diffusion of atoms can occur and results the cavity migration process. These are: (1) surface diffusion, (2) volume diffusion and (3) vapour transport. Schematic representations of the processes are shown in Figure 5.1.

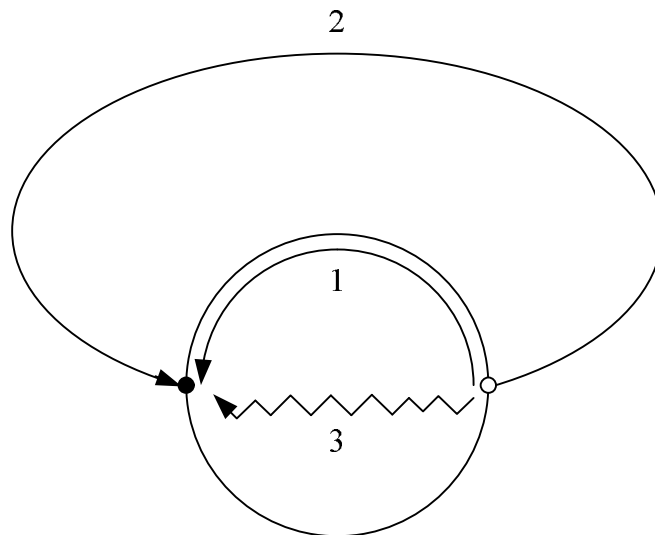


Figure 5.1. Schematic representation of cavity migration by (1) surface diffusion, (2) volume diffusion, and (3) vapour transport [155].

In a surface diffusion process the atoms diffuse around the interior surface of the cavities, in a volume diffusion process they diffuse through the crystal lattice, and in a vapour transport process they diffuse through the vapour phase inside the cavities. The review work by Nichols [117] showed that in the presence of a thermal gradient, if the volume diffusion process dominates, the cavity velocity (V_C) is independent of the cavity radius (r). If the vapour transport process is dominant, V_C is independent of r if the gas

pressure inside the cavity is constant. If the gas pressure inside the cavity is $\frac{2\gamma}{r}$, where, γ is the surface tension, V_C becomes proportional to r . Thus the cavity velocity increases with the increase in cavity radius. If the surface diffusion process is dominant, V_C becomes inversely proportional to r , thus smaller cavities move faster than larger cavities. For sub-micron sized cavities, it is commonly seen that the surface diffusion is the dominant mechanism. For bigger cavities, volume diffusion and vapour transport mechanisms start to play a role in the cavity migration process.

During the coalescence process, the volume of the cavities before and after the coalescence process is conserved. The total surface area thus decreases. Surface diffusion mechanism is the dominant process for this stage to occur. Nichols [117] has shown that this stage occurs for all cavities with a radius larger than 0.1 nm and thus occurs for all practical cases.

5.3 Helium Effusion Kinetics

He effusion from the cavities received considerable attention as well. He effusion from Si implanted with He^+ is capable of giving information on the interaction of He with the vacancy clusters and the role of He in the void formation process. We have discussed the nature of He effusion profiles from Si based on the He^+ implantation doses in Chapter 3. Besides qualitative description of He effusion, there have also been attempts to quantitatively model the He effusion process.

In the low dose regime, thermal desorption spectrometry (TDS) spectra can be described by first order kinetics, the intensity of the TDS spectra varies almost linearly

with the dose [91]. On the other hand, in high dose regime, TDS spectra do not vary linearly with the dose and cannot be described with the first order effusion kinetics [91]. In the first order gas release model, the rate of He release from cavities varies in proportion to the number of He atoms retained in the cavities. It has been reported that the first order gas release model is only capable of describing He retained in samples (from ERD measurements) for the initial short annealing time for isothermal anneal performed [156]. For TDS measurements, He effusion peak from high temperature is reported to be much broader than expected from the first order gas release kinetics. The possibility of describing the broader effusion peak at high temperature by considering emitting centers with varying activation energies has also been discarded [157]. Since He is an inert gas, it does not react with Si. Thus, the observed type of TDS at high temperature cannot be due to different bonding configuration of He with Si. Cerofolini *et al.* [157] also showed that the He effusion kinetics does not depend on the average He concentration in Si, rather depends on the local He concentration in the cavities.

In the modeling attempt of Fedorov [151], the He effusion model used is conceptually too simple. He desorption from Si was considered by first order effusion kinetics by considering constant activation energy for He effusion from the vacancy clusters. The activation energy for He effusion was considered as the binding energy of He with the vacancy cluster only, which is not the case in reality. To date, the most detailed study on He effusion mechanism from Si is reported by Cerofolini *et al.* [157]. In their study, it was considered that the activation energy for He effusion depends on the solution enthalpy and the migration energy of He in the lattice.

A systematic description of He effusion kinetics is described by Cerofolini *et al.* [91], [157]. From these studies we repeat here the important steps of formulating the mathematical equations for He effusion from Si.

It is believed that the high concentration of He inside the cavities works behind the force for He effusion. He effused from a cavity can be retrapped inside another cavity. Multiple trapping and effusion of He from cavities can occur, which can result in formation of quasi-equilibrium concentration of He in the cavity region. For He effusion length greater than the average separation between the cavities, it can be expected that a uniform concentration of interstitial He, C_ψ is achieved. This can certainly occur for a situation where He diffusion length is greater than the width of the cavity region. C_ψ can be calculated from the chemical potential of He interstitials, μ_ψ and the chemical potential of He in cavities, μ_o by applying the condition,

$$\mu_\psi = \mu_o \quad (5.1)$$

μ_ψ is expressed by [157],

$$\mu_\psi = \Delta H_\psi + k_B T \ln \left[\left(\frac{1 - e^{-h\nu_\psi / k_B T}}{e^{-h\nu_\psi / 2k_B T}} \right)^3 \frac{C_\psi / C_S}{1 - C_\psi / C_S} \right] \quad (5.2)$$

where,

ΔH_ψ is the He solution enthalpy in interstitial sites

k_B is the Boltzmann constant

h is the Planck constant

T is the temperature in Kelvin

ν_{ψ} is the vibration frequency of He in an interstitial site

C_s is the concentration of interstitial sites. $C_s = C_{si} \left(1 - \frac{N_o \nu_o}{l_o} \right)$; N_o is number of cavities per unit area, ν_o is the mean cavity volume, and l_o is the thickness of the cavity region.

It is considered that all the implanted He is captured inside the cavities. Cerofolini *et al.* [157] mentioned that this results in typical He concentration of around 10^{23} cm^{-3} for high dose He⁺ implantation done. With such a high He concentration, He inside the cavities is treated as ultra dense gas. In this case, strong He-He repulsion due to van der Waals interaction is in effect, which plays a significant role in He effusion kinetics and He inside the cavities cannot be described by an ideal gas or van der Waals gas. In van der Waals model for moderately dense gas, the concept of covolume is introduced. Covolume limits the particles to access certain portion of the space. van der Waals model considers the value of covolume to remain constant. For hyper dense gas, covolume is treated as a dynamic quantity, which varies with the concentration of He inside the cavities, C_o . Covolume, b for hyper dense gas situation can be calculated using [157],

$$\frac{1}{b} = \left[\frac{2}{3} \pi \left\{ \chi \ln \left(\frac{w}{1.5 k_B T} \right) \right\}^3 \right]^{-1} + \left\{ \frac{2}{3} \pi (k C_o^{-1/3} - \chi \ln \omega)^3 \right\}^{-1} \quad (5.3)$$

w and χ are suitable parameters used to describe He-He Buckingham potential given by [157].

$$u(r) = we^{-r/z} \quad (5.4)$$

Now, for hyper dense gas, the chemical potential of He in cavities, μ_o can be described by [157],

$$\mu_o = \Delta H_o + \frac{1}{2}U + k_B T \left[\ln \left(\frac{bC_o}{1-bC_o} \right) + \frac{bC_o}{1-bC_o} + \ln \left(\frac{\lambda_T^3}{b} \right) \right] \quad (5.5)$$

$$U = \omega u(kC_o^{-1/3}) \quad (5.6)$$

where,

ΔH_o is the energy needed to take a He atom inside cavity from vacuum

U is the repulsive energy due to the presence of neighbouring He atoms

λ_T is the thermal de Broglie wavelength; $\lambda_T = \frac{h}{\sqrt{2\pi mk_B T}}$

ω is the coordination number

k is a parameter related to the packing factor

Now, as shown in refs. [91] and [157], considering low density limit where

$C_\psi / C_s \ll 1$, the outgas He flux can be calculated considering, $J = -D_\psi(x) \frac{\partial C_\psi}{\partial x}$. D_ψ is

the diffusion coefficient of He in interstitial sites and can be expressed by [91],

$$D_\psi = D_{\psi,0} \exp \left(-\frac{\mathcal{E}_{\psi\psi}^*}{k_B T} \right) \quad (5.7)$$

where,

$D_{\psi,0}$ is the prefactor of the Arrhenius expression for the diffusion coefficient of He in interstitial sites

$\varepsilon_{\psi\psi}^*$ is the activation energy for He diffusion through interstitial sites

If it is considered that He diffusion length is greater than x_{O-} , which is the starting depth of cavity layer in Si, we get, $J = \frac{D_{\psi} C_{\psi}}{x_{O-}}$. The outgas He flux, J can then be calculated by applying the condition in Equation (5.1). The rate equation can then be determined applying the steady-state condition, $-\frac{d(V_O C_O)}{dt} = J$, where V_O is the total cavity volume per unit area. This results,

$$\frac{dC_O}{dt} = -\frac{D_{\psi,0} C_s \lambda_T^3}{V_O x_{O-}} \left(\frac{e^{-h\nu_{\psi}/2k_B T}}{1 - e^{-h\nu_{\psi}/k_B T}} \right)^3 \frac{C_O}{1 - bC_O} \exp\left(\frac{bC_O}{1 - bC_O}\right) \exp\left(-\frac{\Delta H_{\psi} - \Delta H_O - \frac{1}{2} \omega u (kC_O^{-1/3}) + \varepsilon_{\psi\psi}^*}{k_B T}\right) \quad (5.8)$$

Cerofolini *et al.* [157] applied Equation (5.8) to describe the He effusion kinetics from Si. They verified their proposed model by comparing the simulation results with the experimental TDS profiles for isochronal annealing done considering an increase in temperature with constant temperature ramp rate.

5.4 Mathematical Model

Our proposed model for void evolution describes the first two moments of the void distribution by describing the concentration of vacancies, which constitute the voids, C_{void} , and the density of voids, D_{void} . The former effectively describes the zeroth moment of the distribution by integrating the total number of vacancies captured by the voids. The latter describes the first moment of the distribution because, in combination with C_{void} it yields the average void diameter. We include additional equations to describe the concentration of vacancies in small vacancy clusters, C_{SV} , the behaviour of free interstitials and vacancies, and the He effusion. The approach of Law and Jones [154] who successfully modeled interstitial cluster dynamics in silicon, specifically the {311} defect was followed in this work. This model is further refined in the commercial process simulator FLOOPS-ISE [9]. However, the model used there is not readily applicable for modeling void evolution process in Si by high dose He⁺ implantation and subsequent high temperature annealing. Thus necessary modifications were made to develop the model equations to describe the void evolution mechanism.

As applied to vacancies, small vacancy clusters, and voids, the model assumptions are:

- All the reaction rates are diffusion limited. The capture rates of the reactions vary in proportion to the size of the vacancy clusters and voids.
- Smaller voids dissolve faster than larger voids.
- Small vacancy clusters as well as voids may capture free vacancies, a process which contributes to void growth.

- It is sufficient to consider small vacancy clusters of a specific size. During the formation of vacancy clusters, certain arrangements of vacancies are more stable than others. Among the small vacancy clusters, clusters with 6, 10 or 14 vacancies show the highest binding energy and thus are the most stable vacancy clusters [158]. The arrangements of vacancies in the cluster are such that the cluster is free from any dangling bonds. We consider small vacancy clusters to contain on average 10 vacancies in our model.
- Bulk recombination between free vacancies and interstitials is taken into consideration.
- Small vacancy clusters are initially filled with He; once He effuses out, small vacancy clusters are allowed to recombine with interstitials.
- Initially grown voids are filled with He, once He effuses out, voids are allowed to recombine with interstitials as well.

The model can be thus described by:

$$\frac{\partial C_{void}}{\partial t} = k_{void_v} D_{void} (C_V - C_V^*) + 11k_{sv} C_{sv} C_V - k_{void_i} D_{void} (C_I - C_I^*) \quad (5.9)$$

$$\frac{\partial D_{void}}{\partial t} = -k_1 D_{void} \frac{D_{void}}{C_{void}} + k_{sv} C_{sv} C_V \quad (5.10)$$

$$\frac{\partial C_{sv}}{\partial t} = k_{sv} C_{sv} (C_V - C_V^*) - 10k_{sv} C_{sv} C_V - k_{si} C_{sv} (C_I - C_I^*) \quad (5.11)$$

where,

C_{void} is the concentration of vacancies in voids

D_{void} is the density of voids

C_{SV} is the concentration of vacancies in small vacancy clusters

C_V is the concentration of vacancies

C_I is the concentration of interstitials

C_V^* is the equilibrium vacancy concentration

C_I^* is the equilibrium interstitial concentration

k_{SV} , k_{SI} , k_{void_V} , k_{void_I} are the diffusion limited reaction rates

k_1 is the fitting parameter

The diffusion limited reaction rates are given by,

$$k_{SV} = 4\pi \left(10^{1/3} r_0 + \frac{r_b}{2} \right) D_V \quad (5.12)$$

$$k_{SI} = 4\pi \left(10^{1/3} r_0 + \frac{r_b}{2} \right) D_I \quad (5.13)$$

$$k_{void_V} = 4\pi \left(n^{1/3} r_0 + \frac{r_b}{2} \right) D_V \quad (5.14)$$

$$k_{void_I} = 4\pi \left(n^{1/3} r_0 + \frac{r_b}{2} \right) D_I \quad (5.15)$$

where,

r_0 is the radius of a vacancy

D_v is the vacancy diffusivity

D_i is the interstitial diffusivity

r_b is the capture radius of bulk recombination between mono vacancy and mono interstitial

and,

n is the size of a void, $n = \frac{C_{void}}{D_{void}}$

The bulk recombination reaction rate is given is,

$$k_{bulk} = 4\pi \cdot r_b (D_v + D_i) \quad (5.16)$$

It can be assumed that the contribution of a single vacancy to the capture radius for bulk recombination is $\frac{r_b}{2}$.

In Equations (5.12) and (5.13), $10^{1/3} r_0 + \frac{r_b}{2}$ represents the capture radius of the small vacancy clusters which is formed with 10 vacancies. $10^{1/3} r_0$ is the radius of the small vacancy clusters. To this term $\frac{r_b}{2}$ is added considering this to be the contribution of a single vacancy to the capture radius. Extending the similar argument to Equations (5.14) and (5.15), the term $n^{1/3} r_0 + \frac{r_b}{2}$ represents the capture radius of a void.

In Equation (5.9) it is considered that individual voids can capture vacancies and grow. Since it is considered that small vacancy clusters consist of 10 vacancies (an average justified by our arguments above), an addition of a vacancy to the small vacancy clusters results in formation of a void, thus increasing the number of vacancies in voids. This also increases the density of voids as taken into account in Equation (5.10). At the same time the formation of voids decrease the concentration of small vacancy clusters in Equation (5.11). In Equation (5.10), the term D_{void} / C_{void} , is inverse to the size of the voids and thus takes into account that smaller voids dissolve faster than larger voids. It is also considered that the larger the number of voids, the faster the voids dissolves. Further, in Equation (5.11) it is considered that the small vacancy clusters can grow by capturing vacancies. The term, $k_{void-I} D_{void} (C_I - C_I^*)$ in Equation (5.9) represents the recombination of voids with interstitials. Similarly, the term, $k_{sv} C_{sv} (C_I - C_I^*)$ in Equation (5.11) represents the recombination of small vacancy clusters with interstitials. These recombination terms with interstitials are considered in the model only when He concentration becomes less than 1% of the concentration of vacancies in voids and small vacancy clusters.

The role of He in the proposed model is to stabilize small vacancy clusters and voids by not allowing small vacancy clusters and voids to recombine with interstitials. During the simulations it is considered that all the implanted He is initially accumulated inside the small vacancy clusters. When voids are formed, voids are initially filled with He. He effusion during the annealing process is calculated by Equation (5.8). Though Cerofolini *et al.* [157] applied Equation (5.8) to match experimental TDS spectra with a

constant temperature ramp, since the equation is derived considering the detailed aspects of the properties of He inside the cavities, it can be expected that, the same equation is capable to describe He effusion during annealing done in isothermal condition.

5.5 Simulation Approach, Results and Discussions

5.5.1 Experimental Results

We compared our simulation results with a wide range of experimental results for He⁺ implanted Si and limited our consideration to studies that quantified the evolution of the void distribution so as to allow quantitative comparison with our model predictions. Experimental results reported in refs. [11], [92], [99], [156] provide a wide range of implant and anneal conditions. We also compared the simulation results with our experimental results described in Chapter 4.

Raineri *et al.* [99] implanted CZ Si wafers with He⁺ ions at 40 and 300 keV with doses of 1×10^{16} , 5×10^{16} and 1×10^{17} cm⁻² and formed voids by annealing in a low pressure (10^{-6} Torr) furnace at temperatures in the range 800-1200°C. The authors reported the void diameter and the void density as a function of anneal temperature for annealing done for 1 hour. Void diameter and void density as a function of anneal time at 800°C and 1000°C were also reported for implantation done with dose of 5×10^{16} cm⁻² at 40 keV. Roqueta *et al.* [92] and Kaschny *et al.* [156] implanted Si with 40 keV, 5×10^{16} cm⁻² He⁺ ions and reported void diameter upon annealing the samples at 800°C. Kaschny *et al.* annealed their CZ Si sample in Ar for 10 minutes in RTA, whereas Roqueta *et al.* annealed their FZ Si samples in N₂ for 10 sec in RTA and 50 min in FA. Follstaedt *et al.*

[11] reported void diameter for FZ Si implanted with 30 keV, $1 \times 10^{17} \text{ cm}^{-2}$ He^+ ions annealed in the range 700-1000°C for 30 min. They also did one experiment using a lower dose of $2 \times 10^{16} \text{ cm}^{-2}$ He^+ implanted with an energy of 30 keV and annealed for 30 min at 700°C. Their experimental result for this data point is anomalous in that they report a larger void diameter for these conditions than for the $1 \times 10^{17} \text{ cm}^{-2}$ dose with a 700°C anneal. This is contradictory to all other available data which indicate that the decrease in dose leads to smaller void diameters. We have thus ignored this data point in our modeling. The same authors also did one experiment with a 10 hour anneal. At these long anneal times void growth is expected to saturate. This is an effect that we have not included in our model and hence we did not compare our model against the 10 hour experiment. The data we have considered are summarized in Table 5.1.

5.5.2 Initial Conditions

The implantation of He^+ in Si produces interstitials and vacancies. The as-implanted vacancy and interstitial profiles were extracted using the Monte Carlo based ion implantation simulator Crystal TRIM available in FLOOPS-ISE [9]. It is known that most of the interstitials and vacancies thus created recombine during the implant step - this is termed dynamic annealing. We assumed that only 5.5% of the damage remains after the implant step. This value was chosen as the midpoint of the range (1-10%) suggested by Knights *et al.* [50].

For the interstitials, the case is relatively simple. The profile of interstitials calculated as above is considered as the initial profile of free interstitials, C_I . For vacancies, the situation is more complex as the vacancies could be free mono vacancies,

Table 5.1: Experimental data available from literature

Author [ref]	Substrate type	Implant energy (keV)	Implant dose (cm^{-2})	Anneal temperature ($^{\circ}\text{C}$)	Anneal time	Anneal ambient and pressure
Raineri <i>et al.</i> [99] – Isochronal data	CZ Si	40, 300	1×10^{16} , 5×10^{16} , 1×10^{17}	800 , 1000, 1200	60 min	Inert, 10^{-6} Torr
Raineri <i>et al.</i> [99] – Isothermal data	CZ Si	40	5×10^{16}	800 , 1000	15 - 120 min	Inert, 10^{-6} Torr
Follstaedt <i>et al.</i> [11]	FZ Si	30	1×10^{17}	700, 800, 900 , 1000	30 min	Inert, atmospheric pressure
Roqueta <i>et al.</i> [92]	FZ Si	40	5×10^{16}	800	10 sec, 50 min	N_2 , atmospheric pressure
Kaschny <i>et al.</i> [156]	CZ Si	40	5×10^{16}	800	10 min	Ar, atmospheric pressure

vacancies captured in small vacancy clusters, or vacancies in voids. Given the expected void evolution mechanisms described in Chapters 3, we do not expect any voids initially. Hence we initialized C_{void} and D_{void} to very low constants in the sample (we did not set them to zero simply to avoid numerical difficulties). As for small vacancy clusters, these are only expected to form when the damage cascade overlap is relatively high. This

happens above a certain implant dose, the threshold dose, which varies with implant energy, dose rate, and implant temperature. For cases where vacancy clusters are expected to form, we arbitrarily set 5% of the vacancy profile to be in clusters, with the remaining 95% of the vacancies as free mono vacancies. Where clusters were not expected, the entire vacancy profile was attributed to mono vacancies. Thus we determine the initial profiles of C_V and C_{SV} . This is a recognized limit in our model - we have made no attempt to quantitatively model the formation of small vacancy clusters during implant. Our model only addresses post implant void evolution.

For the He concentration, we calculated the initial value of C_O from as-implanted He profile from Crystal TRIM by considering that all the He is confined in the cavity layer.

5.5.3 Model Parameters

As mentioned previously, the constant k_I in Equation (5.10) was used as a “free” fitting parameter. We discuss the significance of this parameter separately. The other parameters in the model all have reasonably well known values from the literature, which we describe in this section.

We used $r_b = 0.5$ nm in our simulations following ref. [159] and used $r_0 = 0.1684$ nm taking the volume of a single vacancy as 2×10^{-23} cm³ [121]. For point defects in silicon the $D_X C_X^*$ product ($X = I, V$) is known with high precision. However, the partition of that product into a diffusivity (D_X) and solubility (C_X^*) is far from agreed, with reported values in the literature spanning several orders of magnitude. For D_I and C_I^* ,

we used the default values in FLOOPS-ISE. For D_V and C_V^* , we maintained the $D_V C_V^*$ product that is well specified in the literature. However, it is well known that modeling diffusional processes such as the one considered here is sensitive to the specific partitioning of this product. We found that optimal fits to our data obtained with D_V set to 0.7 of the default value in FLOOPS-ISE. Given the sensitivity of diffusional models to this value and the reported variation in the literature spanning several orders of magnitude, a factor of 0.7 is effectively negligible. With these numbers we completely specify the reaction rates given by Equations (5.12)-(5.15).

While applying the model for dry O_2 anneal data for our experimental results we use the default interstitial injection flux from FLOOPS-ISE but used a higher surface recombination velocity than the default. We increased the default value of surface recombination velocity in FLOOPS-ISE by a constant factor. This is reasonable since this is the expected behaviour for interstitial injection under conditions of high implant damage as we have in our experiments [160].

When applying the He effusion kinetics described by Equation (5.8), we used the parameter values considered in ref. [157]. The values used in the simulations are, $v_\psi = 2 \times 10^{13} \text{ sec}^{-1}$, $D_{\psi,0} = 5.25 \times 10^{-3} \text{ cm}^2 \text{ sec}^{-1}$, $\omega = 12$, $k = 1.122$, $\Delta H_\psi - \Delta H_O + \varepsilon_{\psi\psi}^* = 1.83 \text{ eV}$, $w = 3000 \text{ eV}$, $\chi = 0.192 \text{ \AA}$. We calculated the values of x_{O^-} and l_O from the He^+ implantation profiles from Crystal TRIM. l_O is considered to extend from the TRIM values for depth of the maximum vacancy concentration to the depth of the maximum He concentration. We calculated the values of N_O and v_O from the TEM images taken for

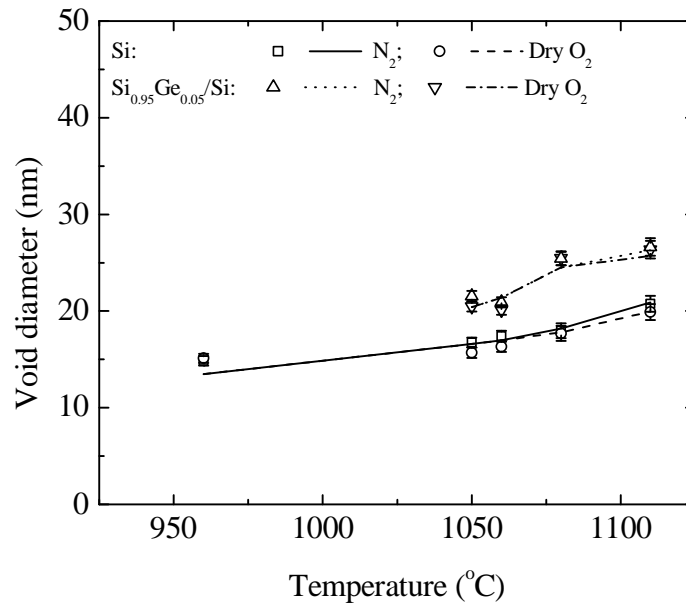
our experimental results described in Chapter 4. Our experiments have He^+ implantation dose of $5 \times 10^{16} \text{ cm}^{-2}$. Since we did not have access to the TEM images for the previously published results in the literature, we approximated the values of N_o and v_o for the previously published results in the literature for implantation doses of $5 \times 10^{16} \text{ cm}^{-2}$ and $1 \times 10^{17} \text{ cm}^{-2}$ with the calculated values from our experimental studies for implantation dose of $5 \times 10^{16} \text{ cm}^{-2}$. For previously published results for He^+ implantation dose of $1 \times 10^{16} \text{ cm}^{-2}$, we used the values reported in refs. [91] and [157]. We implemented the He effusion kinetics given by Equation (5.8) and the model equations given by Equations (5.9)-(5.11) using the commercially available process simulator FLOOPS-ISE.

$C_{\text{void}}/D_{\text{void}}$ gives the average number of vacancies per void and thus represents the average size of the void. The volume of each vacancy is $2 \times 10^{-23} \text{ cm}^3$ [121], from which we calculated average void volume. Considering each void to be spherical in shape, we calculated the average diameter of each void. The void density, D_{void} , is directly obtained by solving Equation (5.10).

5.5.4 Simulation Results

Figures 5.2-5.7 show comparisons between our model and experimental results. In the first four figures both void diameter and void density were reported. In Figure 5.6 and Figure 5.7 we consider studies where only void diameter was reported. Figure 5.2 shows our own data, Figures 5.3-5.4 show Raineri's isochronal anneals for 40 keV and 300 keV implants respectively, whereas Figure 5.5 shows their isothermal anneals [99]. Finally, Figure 5.6 shows the data reported by Follstaedt *et al.* [11], and Figure 5.7 shows the data reported by Roqueta *et al.* [92] and Kaschny *et al.* [156].

(a)



(b)

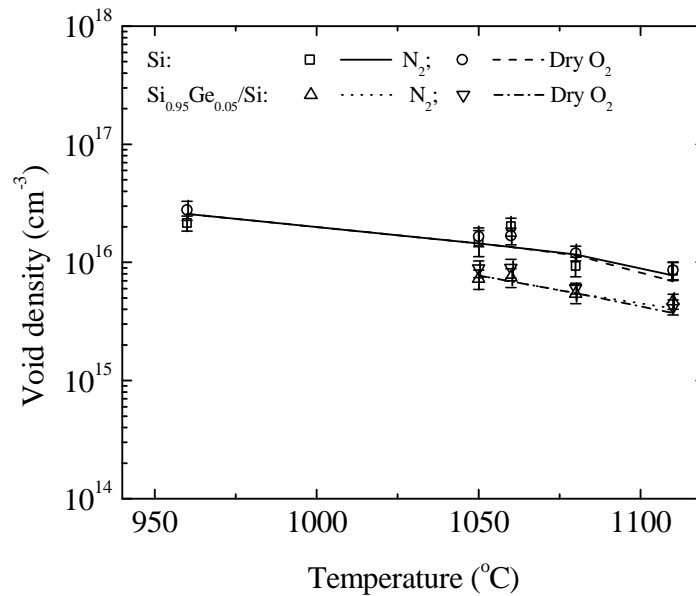
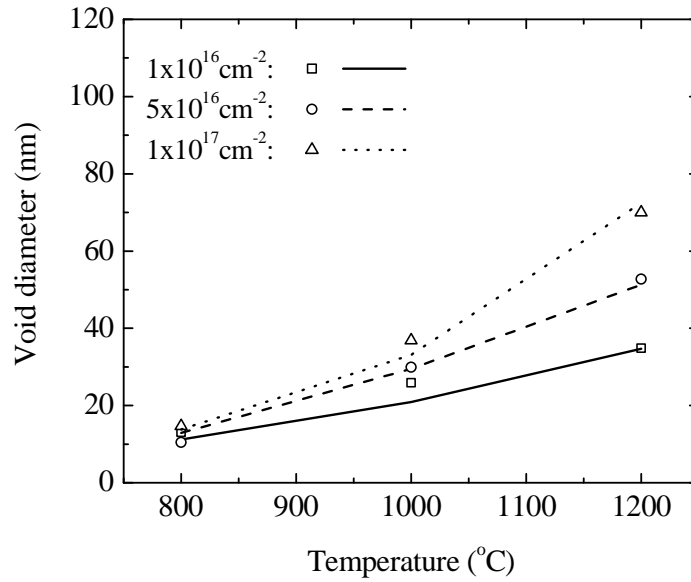


Figure 5.2. (a) void diameter and (b) void density as a function of anneal temperature for our experiments. Samples were implanted with 30 keV, $5 \times 10^{16} \text{ cm}^{-2}$ He^+ . Symbols refer to experimental data, lines refer to simulation.

(a)



(b)

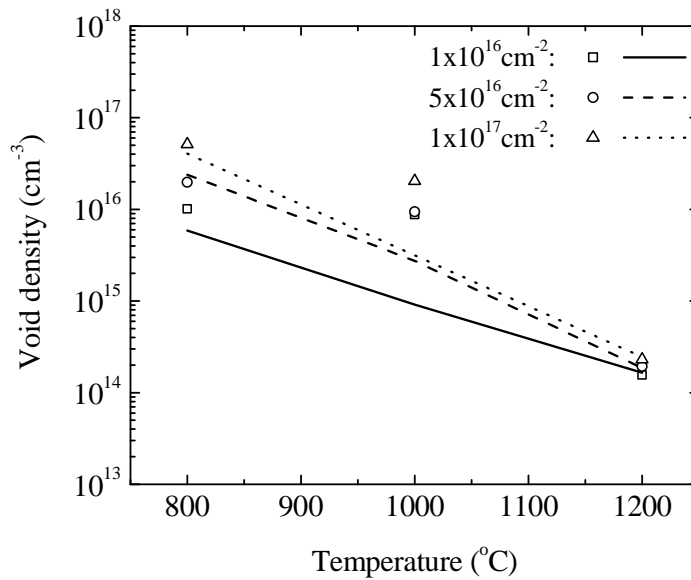
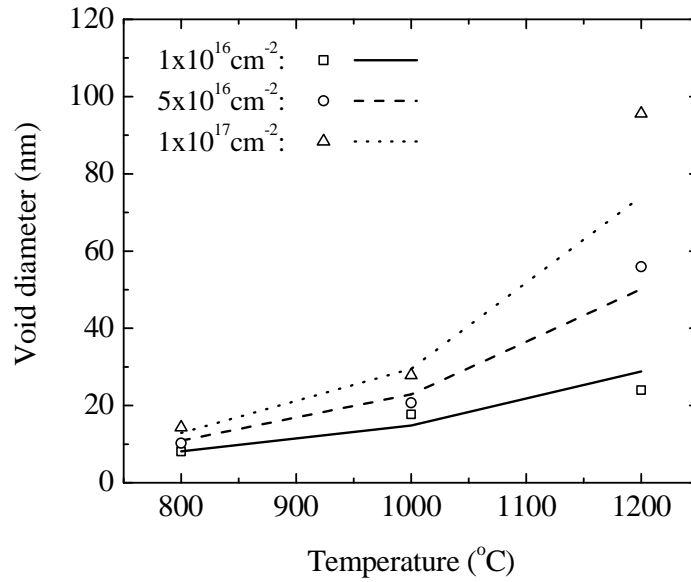


Figure 5.3. (a) void diameter and (b) void density as a function of anneal temperature. Si samples were implanted with different doses of He⁺ at 40 keV. Experimental data were reported by Raineri *et al.* [99]. Symbols refer to experimental data, lines refer to simulation.

(a)



(b)

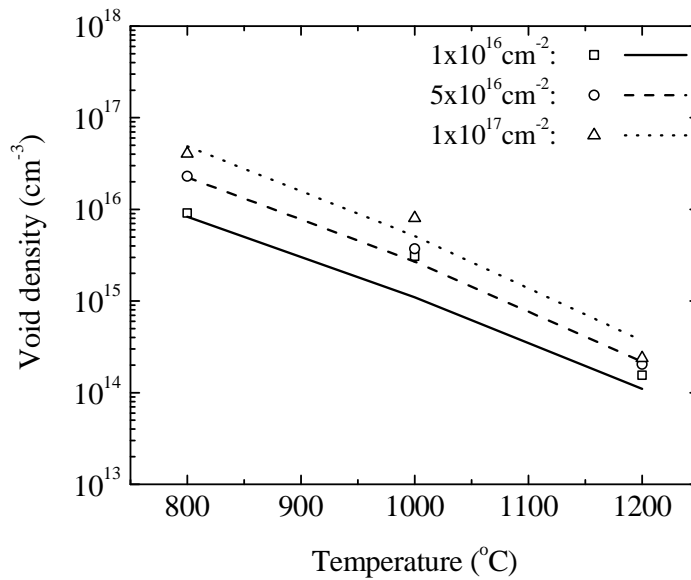
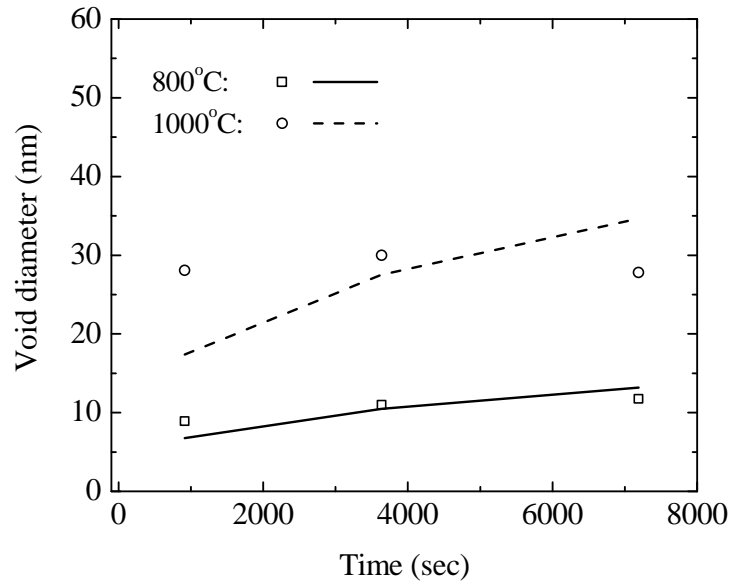


Figure 5.4. (a) void diameter and (b) void density as a function of anneal temperature. Si samples were implanted with different doses of He⁺ at 300 keV. Experimental data were reported by Raineri *et al.* [99]. Symbols refer to experimental data, lines refer to simulation.

(a)



(b)

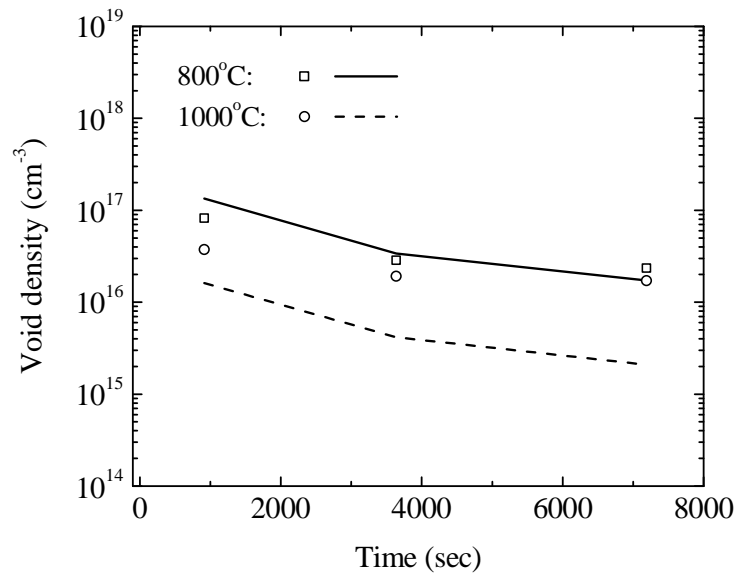


Figure 5.5. (a) void diameter and (b) void density as a function of anneal time. Si samples were implanted with 40 keV, $5 \times 10^{16} \text{ cm}^{-2} \text{ He}^+$. Experimental data were reported by Raineri *et al.* [99]. Symbols refer to experimental data, lines refer to simulation.

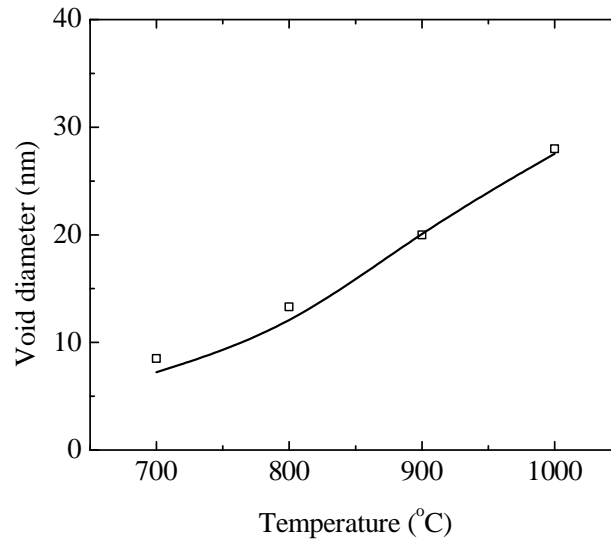


Figure 5.6. Void diameter as a function of anneal temperature. Si samples were implanted with 30 keV, $1 \times 10^{17} \text{ cm}^{-2} \text{ He}^+$. Experimental data were reported by Follstaedt *et al.* [11]. Symbols refer to experimental data, line refers to simulation.

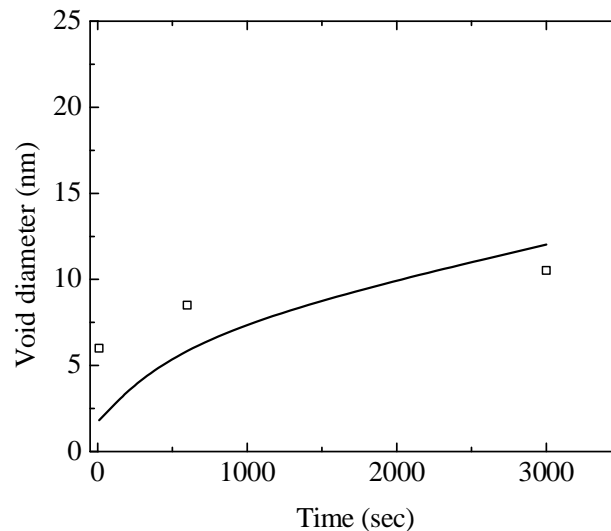


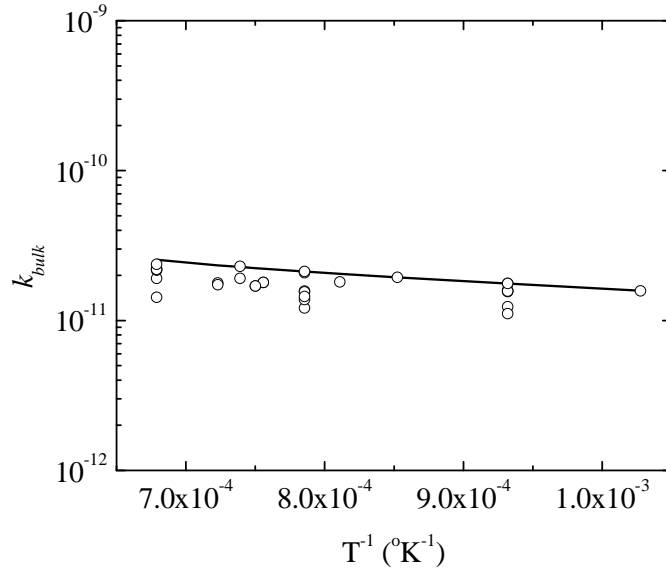
Figure 5.7. Void diameter as a function of anneal time at 800°C. Si samples were implanted with 40 keV, $5 \times 10^{16} \text{ cm}^{-2} \text{ He}^+$ ions. Experimental data were reported by Roqueta *et al.* [92] and Kaschny *et al.* [156]. Symbols refer to experimental data, line refers to simulation.

For the most part our simulations agree very well with the experimental data. One minor anomaly is observed in the experimental data of Raineri *et al.* [99] at 1000°C. In all cases at this temperature their reported void densities are larger than what would be predicted based on their reported void diameters. This is most clearly visible in Figure 5.3 where for the conditions given at all anneal temperatures, the void diameters shown in Figure 5.3(a) grow from 800°C to 1000°C but the void densities shown in Figure 5.3(b) remain constant. Regardless of the growth dynamics of the voids we would expect growth in diameter to come at the expense of void density. Not surprisingly, our model does not match these anomalous results.

We used k_I as a free parameter in our model. For each anneal temperature the reaction rates given by Equations (5.12)-(5.15) were calculated. In the simulations, the exact values of k_{SI} , k_{void_V} and k_{void_I} were used. For each anneal temperature and implantation condition, the values of k_{SV} and k_{bulk} ; and the free parameter k_I were set to simultaneously obtain a good match between the simulated and experimental values of void diameter and void density. The values of k_{bulk} and k_{SV} used in the simulations are shown in Figure 5.8 (a) and (b). These values are very close to the actual values of the diffusion limited reaction rates [9] suggesting diffusing limited reaction rate to be the dominant process for these reactions.

It is apparent that the free parameter k_I in our simulation is related to the physical mechanisms involved in the migration and coalescence process of cavities. The unit of k_I is sec^{-1} and to our understanding it represents the rate of migration and coalescence process of the cavities. We should note that given our simulation procedure, the value of

(a)



(b)

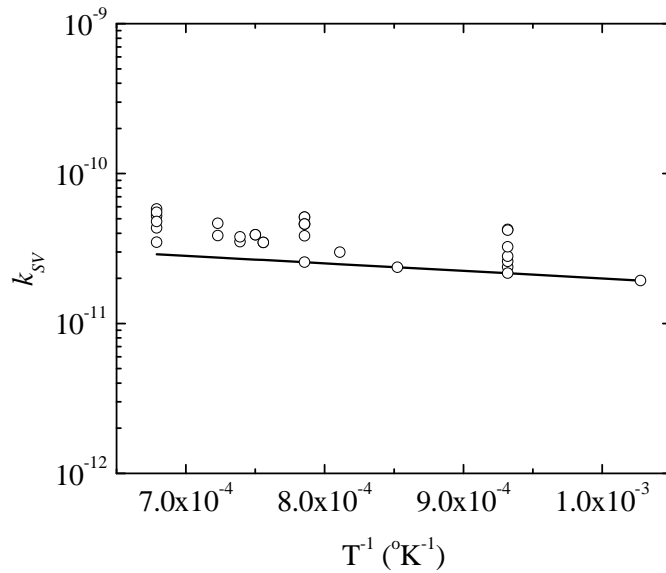


Figure 5.8. Values of (a) k_{bulk} and (b) k_{SV} used in the simulations. Lines refer to the theoretical trend, symbols refer to the values used in the simulations.

k_I is an average value over the anneal time. The actual rate of migration and coalescence would increase initially as cavities are formed and then begin to decrease as the cavities grow. For the entire cavity to diffuse in a given direction there has to be a net transfer of adatoms along the inner surface of the cavity. The likelihood of such a net transfer decreases drastically once the cavity diameter is of the order of the mean free path of the adatoms. (This is likely the cause of saturation in cavity growth, but as noted earlier we have not included this in our model). Hence any conclusions we draw regarding k_I are only applicable for anneal durations on the order of a few hours, which is the regime that has been modeled in our studies and those that we have taken into account.

Figure 5.9 shows the values of k_I used in the simulations to get a good match between simulated and experimental values. There are several features that we can notice. The spread of the values of k_I is quite large. However, for each implantation condition, k_I follows an Arrhenius behaviour, suggesting k_I is related to a thermally activated process. It has been suggested in literature that for sub-micron cavities, migration and coalescence process is dominated by the surface diffusion mechanism [117]. Thus, we expect that the activation energy of k_I should represent the activation energy of surface diffusion process in Si. In the temperature range 700-1200°C, the reported activation energy for surface diffusion process varies in the range 1.2-2.68 eV [161]. The extracted activation energy of k_I for the values used in the simulations varies in the range 1.15-2.06 eV. The range of extracted energies thus fits in the range of activation energies reported in literature.

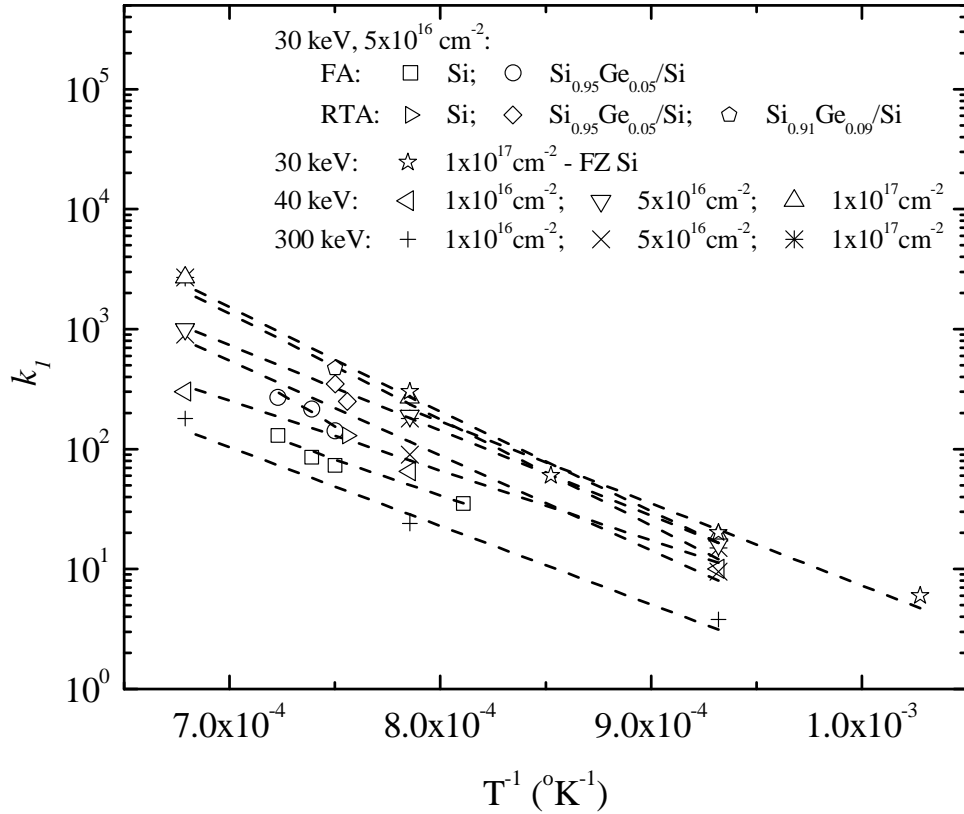


Figure 5.9. Variation of k_l as a function of inverse temperature. Symbols are the values used in the simulations, lines represent the Arrhenius fits.

Once k_l is understood to be a rate parameter for the migration and coalescence process governed by the adatom surface diffusivity, and calculated as a time average over the anneal duration, the trends in Figure 5.9 can be interpreted in a consistent manner.

The value of k_l increases linearly with the dose as shown in Figure 5.10. As the dose increases, there is more damage created in the lattice, and the amount of initial small vacancy clusters increases. The increase in the number of small vacancy clusters results in

faster coalescence of the small vacancy clusters, thus producing larger voids as observed by the experimental results reported by Raineri *et al.* [99]. Faster coalescence means increase in the rate of migration and coalescence process and thus we notice an increase in k_I with the dose.

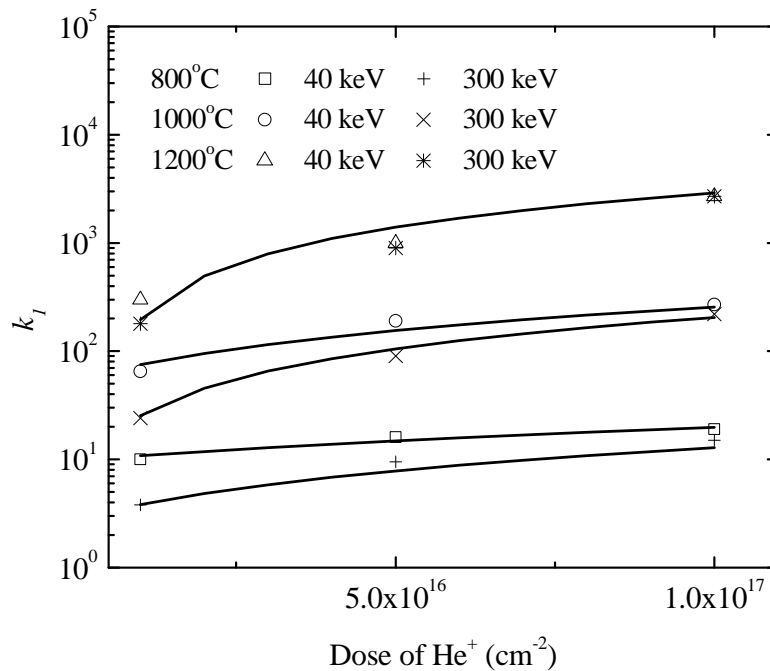


Figure 5.10. Variation of k_I as a function of dose. Symbols are the values used in the simulations, lines represent the linear fits.

The values of k_I also depend on implantation energy. Increase in implantation energy increases the straggle, which results in decrease in damage at the projected range of implantation. We can expect that this will result in decrease in the amount of small vacancy clusters produced during He⁺ implantation. The decrease in the amount of small vacancy clusters will result in increased time for the migration of the small vacancy clusters to coalesce and form larger voids. This results in a decrease in the rate of the

migration and coalescence process. Further, increase in implantation energy can result in suppressed effusion of He from cavities. It has been shown by Perryman and Goodhew [162] that the presence of He in cavities hinders the surface diffusion process, and thus lowers the rate of migration and coalescence mechanism. In presence of gas inside the cavities, during the surface diffusion process, an adatom at the surface may not be able to jump to a neighboring site as the site may have already been occupied by a gas atom. Mikhlin [163] has shown that for an adatom to diffuse, a certain volume around the adatom must be free of gas atoms. The slower He effusion thus reduces the rate of migration and coalescence mechanism. The average void diameter thus decreases with the increase in implantation energy and we notice decrease of the value of k_I .

The value of k_I is also dependent on pressure. Raineri *et al.* [99] annealed their samples in a low pressure (10^{-6} Torr) furnace. The low atmospheric pressure results in faster He effusion from the bubbles in Si during high temperature annealing. As discussed in the preceding paragraph, this increases the rate of migration and coalescence mechanism and results in higher average void diameter when compared with our own experiments where we used atmospheric pressure. We thus observe a higher value of k_I for simulating their results compared with ours.

Now looking at the values of k_I for our experimental results during annealing done in FA, we find that the values of k_I are higher for $\text{Si}_{0.95}\text{Ge}_{0.05}/\text{Si}$ samples when compared with the values in Si samples. Our $\text{Si}_{0.95}\text{Ge}_{0.05}/\text{Si}$ samples contained a 60 nm $\text{Si}_{0.95}\text{Ge}_{0.05}$ epilayer on Si. $\text{Si}_{0.95}\text{Ge}_{0.05}$ epilayer remained under compressive strain so that the Si was under tensile strain in the region close to the $\text{Si}_{0.95}\text{Ge}_{0.05}$ and Si interface. From

Crystal TRIM simulation, it is found that the maximum vacancy damage occurs at a depth of about 250 nm from the surface, i.e, is about 190 nm from the $\text{Si}_{0.95}\text{Ge}_{0.05}/\text{Si}$ interface. Hence it is unlikely that the tensile strain in Si due to the presence of the epilayer will reach to this depth. As we have discussed in Chapter 4, due to high temperature annealing and the presence of considerable implantation damage, it is expected that Ge will diffuse into the Si (or more precisely the Si and Ge interdiffuse). The resulting stress gradient and the weaker Si-Ge bond strength compared to Si-Si bond are expected to cause faster surface diffusion in the cavities and thus increase the rate of cavity migration. Any such process will thus result in increase in average void diameter and we find an increase in k_I for $\text{Si}_{0.95}\text{Ge}_{0.05}/\text{Si}$ samples in our simulations. In our RTA experiments we find an even higher rate of migration and coalescence. The underlying reason is very similar to the effect of lower pressure. The higher temperature ramp rate for the RTA causes faster He effusion and an earlier onset of the migration and coalescence process.

The last observation we make is the value of k_I for 30 keV, $1 \times 10^{17} \text{ cm}^{-2} \text{ He}^+$ implantation condition for simulating the results of Follstaedt *et al.* [11]. The values of k_I for this case are comparable with the values of k_I for 40 keV, $1 \times 10^{17} \text{ cm}^{-2} \text{ He}^+$ implantation data of Raineri *et al.* [99] despite the anneals by Follstaedt *et al.* being conducted at atmospheric pressure. Follstaedt *et al.* used FZ Si samples, which are known to have lower concentrations of O and C impurities than CZ Si. Evans *et al.* [118] reported that the presence of O can interact with cavities and can reduce the rate of migration and coalescence process. Thus lower O content may increase the rate of migration and coalescence process.

The above discussion demonstrates both the strength and the limitation of this model. The k_I parameter clearly reflects a physical quantity, the rate of migration and coalescence of cavities. Thus its behaviour may be estimated according to how process conditions are likely to affect the migration and coalescence process: it is increased by higher damage concentration (which can result from higher implant dose, higher implant dose rate, or lower implant energy), faster He effusion (due to lower pressure during anneal or a higher anneal ramp rate), and factors increasing surface diffusivity of adatoms, including lower impurities (as in FZ samples) or higher Ge concentration. The limitation is that this parameter captures the impact of all these factors in a way for which we have yet to account theoretically. Nonetheless, the experimental space that we have covered gives an empirical measure of k_I covering a very wide range of experimental conditions and useful for predictive simulation.

Chapter 6

Boron Diffusion in Si and $\text{Si}_{0.95}\text{Ge}_{0.05}$ - capped Si and Correlation with Void Evolution

We have seen in Chapter 4 and Chapter 5 that the presence of $\text{Si}_{1-x}\text{Ge}_x$ epilayer on Si can influence the void evolution in Si when ion implantation has been done with 30 keV, $5 \times 10^{16} \text{ cm}^{-2} \text{ He}^+$. With the shrinkage in device size, it has become necessary to form shallower junctions to ensure proper device operations. This warrants to study the dopant diffusion behaviour more carefully with varying experimental conditions. $\text{Si}_{1-x}\text{Ge}_x$ is now routinely incorporated in CMOS processing steps. Since the presence of $\text{Si}_{1-x}\text{Ge}_x$ epilayer on Si influences void evolution process in Si, it will be thus interesting to study whether the presence of $\text{Si}_{1-x}\text{Ge}_x$ epilayer on Si can influence the dopant diffusion process in Si during high temperature annealing. In this chapter, the role of the presence of $\text{Si}_{0.95}\text{Ge}_{0.05}$ epilayer on B diffusion process in Si is reported. First, a review on B diffusion in $\text{Si}_{1-x}\text{Ge}_x$ and in Si with $\text{Si}_{1-x}\text{Ge}_x$ layers present in proximity is reported. Next, the experimental studies carried out in this study are reported and possible hypotheses to describe B diffusion patterns are discussed. The proposed hypotheses are then correlated with the void evolution mechanism in $\text{Si}_{1-x}\text{Ge}_x/\text{Si}$ samples described in Chapter 4.

6.1 Background

The incorporation of SiGe in conventional Si based CMOS processing steps is one of the pathways to meet the device shrinkage requirement and is used in fabrication of CMOS devices [3]. When SiGe is incorporated in device structures, strain is introduced due to the lattice mismatch between Si and SiGe. The amount of strain introduced is dependent on the Ge fraction in SiGe, the higher is the Ge fraction, the higher is the strain. With the continuous shrinkage in device dimensions, local strain can be large enough and can be present in the active area of the device structure. The conventional CMOS processing steps involve growth of oxide and nitride layers, which can introduce significant amount of strain in Si close to the interface. Further, shallow trench isolation or local oxidation to isolate the devices can also introduce strain in the device structure. Strain can play an important role in determining the device characteristics. For example, one method to enhance the carrier mobility in the MOSFET channel is to introduce tensile strain in the channel by growing the Si channel on relaxed SiGe [164]. The presence of Ge and the strain introduced can affect the processing related phenomena, for example, dopant diffusion. The study of dopant diffusion is thus an active and essential research direction. B is the most commonly used p-type dopant. B diffusion is enhanced by interstitial injection and retarded by vacancy injection process, the processes which indicate that B diffusion process occurs by I-assisted mechanism [44], [165]-[168]. B being a light dopant has a very high diffusivity and thus controlling the p-type layer width with B as a dopant has received much research attention. The study of B diffusion in presence of Ge and strain is no exception. The presence of Ge and strain can alter the

equilibrium concentrations of point defects in Si. The chemical effect due solely to Ge concentration is to increase equilibrium concentrations of both vacancies and interstitials due to weaker Si-Ge bonds [10]. By contrast, strain affects vacancies and interstitials in opposite ways. Tensile strain decreases the equilibrium concentration of vacancies and increases the equilibrium concentration of interstitials. Compressive strain has the opposite effect on equilibrium point defect concentrations [10], [169]. Strain can also influence the formation of extended defects [170]. Changes in equilibrium point defect concentrations can influence the behaviour of dopant diffusion in Si. Since the presence of Ge can alter the point defect concentration and can introduce strain in the sample, interdiffusion of Si and Ge during high temperature annealing may also influence the dopant diffusion process.

There are several reports available in literature that study the role of the presence of Ge on B diffusion process in Si. It has been reported that in both strained and relaxed SiGe alloys, B diffusion decreases with the presence of up to 40% Ge in Si [171]-[180]. Studies are reported which attempt to investigate the reason behind retarded B diffusion in presence of Ge. The effects those have been suggested are Ge-B cluster formation, increase in migration barrier of B, bandgap narrowing, strain effect, and change in formation energies of point defects and dopant defect pairs. There is however no general agreement in literature on which mechanism works behind the retarded B diffusion in presence of Ge in Si.

Radic *et al.* [179] reported retarded B diffusion mechanism in Si in presence of low concentration of Ge (~3%). The authors argued for Ge-B cluster formation being

responsible for the retarded B diffusion and proposed a physically based model for B diffusion in presence of Ge. Besides forming Ge-B cluster, it was considered that BI and GeBI clusters are formed. However, the concentration of GeBI cluster was considered not to be significant when compared with the concentration of Ge-B cluster. The authors were successful to match experimental B SIMS profiles with their proposed physically based mathematical model by taking into account the Ge-B cluster formation. The study by Peterström and Svensson [180] also argued for the attraction between B and Ge atoms causing the retardation of B diffusion observed during Si implanted with approximately 10^{15} cm^{-2} Ge ions. We performed ion implantation simulation using the process simulator FLOOPS-ISE for the Ge implantation condition reported in ref. [180]. The peak Ge concentration from the simulation is $1 \times 10^{20} \text{ cm}^{-3}$, representing 0.2% Ge in Si. The presence of this small fraction of Ge is thus capable to retard B diffusion. Kuo *et al.* [175] also supported the idea of Ge-B cluster formation. Since Ge and B introduce strain in Si lattice that compensates each other, the authors argued that Ge-B cluster formation is a favourable process to occur, which leads to retarded B diffusion.

However, there are studies which argue for other mechanisms leading to the retarded B diffusion in $\text{Si}_{1-x}\text{Ge}_x$. First principle calculation by Bang *et al.* [181] reported that the binding energy between Ge and B atoms is very small, thus Ge atoms cannot trap B atoms. Thus B retarded diffusion in presence of Ge cannot be due to Ge-B cluster formation. Rather, the authors argued that the presence of Ge results in increase in B migration barrier. B migration barrier increases with the increase in the number of Ge atoms. This leads to reduction in B diffusivity in $\text{Si}_{1-x}\text{Ge}_x$ alloys. Similar results are

reported by Wang *et al.* [182] based on their *ab initio* calculations. Wang *et al.* [182] also suggested that interstitial migration barrier increases in presence of Ge, thus the number of interstitials available to contribute to B diffusion decreases. Also, interstitial Ge faces difficulties to kick out substitutional B to create interstitial B and thus retards B diffusivity.

Due to the lattice mismatch between Si and $\text{Si}_{1-x}\text{Ge}_x$, it is possible to introduce either tensile or compressive strain in the structure. For examples, if Si is grown on top of a relaxed $\text{Si}_{1-x}\text{Ge}_x$ substrate, Si will be under tensile strain. On the other hand, if $\text{Si}_{1-x}\text{Ge}_x$ is grown on relaxed Si substrate, $\text{Si}_{1-x}\text{Ge}_x$ will be under compressive strain. It is also possible to grow $\text{Si}_{1-x}\text{Ge}_x$ on a relaxed $\text{Si}_{1-y}\text{Ge}_y$ substrate, the type of strain introduced to $\text{Si}_{1-x}\text{Ge}_x$ layer will depend on the Ge fractions x and y considered. There are few reported studies which focus on exploring the role of strain on B diffusion process. The theoretical study of Lin *et al.* [183] reported that the tensile strain in Si tends to reduce both the formation and the migration energies of B-Si complexes for all the charge states. This results in enhanced B diffusion under the presence of tensile strain in Si considering B diffuses entirely by interstitial assisted mechanism. Zangenberg *et al.* [24] observed enhanced B diffusion by a factor of ~ 2 in tensile strained Si compared to that of unstrained Si. Tensile strain in Si was introduced by growing Si on $\text{Si}_{0.94}\text{Ge}_{0.06}$ substrate by molecular beam epitaxy (MBE) process. The samples were annealed in an open furnace without any gas flow for 1 hour in the temperature range 800-900°C. To ensure no point defect injection occurs, the surfaces of the samples were capped by radio frequency sputtered SiO_2 and Si_2N_3 layers. Further, B diffusion in compressive strained

$\text{Si}_{1-x}\text{Ge}_x$ ($x=0.12, 0.24$) and in tensile strained $\text{Si}_{1-x}\text{Ge}_x$ ($x=0.12$) was reported. It was reported that tensile strain and compressive strain respectively increases and decreases B diffusivity. Zangenberg *et al.* [24] also reported B diffusion in relaxed $\text{Si}_{1-x}\text{Ge}_x$ ($x=0.01, 0.12, 0.24$). Interestingly, the authors reported that B diffusion coefficient in relaxed $\text{Si}_{1-x}\text{Ge}_x$ samples to be insensitive to Ge concentration. Zangenberg *et al.* however did not discard the Ge-B clustering model proposed by others and mentioned that the increase in the diffusion of interstitial diffusers with the increase in Ge content can counter the effect of Ge-B clustering process, thus making B diffusion to be insensitive to Ge content.

There have also been experimental results indicating retarded B diffusion in tensile strained Si. In a study by Kuo *et al.* [174], samples were grown by chemical vapour deposition (CVD) process. Tensile strain in Si was introduced by growing Si on relaxed $\text{Si}_{1-x}\text{Ge}_x$ ($x=0.105$ and 0.195) substrate. The strained Si layer was capped with a $\text{Si}_{1-x}\text{Ge}_x$ layer having the same Ge fraction of the substrate. The strained Si layer was doped with *in situ* B during CVD growth. The samples were furnace annealed under purified Ar flow for 4 hours at 800°C . The resulting B diffusion in tensile strained Si was retarded when compared to unstrained Si. Zangenberg *et al.* [24] pointed out that the annealing was done without any protective capping layer over $\text{Si}_{1-x}\text{Ge}_x$, which might have resulted in point defect injection leading to retarded B diffusion. However, the anneal ambient used in Kuo *et al.* study was purified Ar. We do not expect that the $\text{Si}_{1-x}\text{Ge}_x$ capping layer would react with purified Ar and the injection of point defects seems unlikely. There are a few studies reporting a correlation between hydrostatic pressure and biaxial stress on dopant diffusion mechanism [169], [184]-[185]. None of these reports

would explain the retarded B diffusion in tensile strained Si reported by Kuo *et al.* To our understanding, the annealing conditions both in Zangenberg *et al.* and Kuo *et al.* studies were such that no significant amount of interdiffusion of Si and Ge occurred across the $\text{Si}_{1-x}\text{Ge}_x/\text{Si}$ interface and there were no interactions between Ge and B. Kuo *et al.* [174] also reported B diffusion in $\text{Si}_{1-x}\text{Ge}_x$ ($x = 0.10, 0.20$). $\text{Si}_{1-x}\text{Ge}_x$ layer in their structure was put under strain (either tensile or compressive). Kuo *et al.* reported that B diffusion depends only on Ge fraction and does not depend on strain present in $\text{Si}_{1-x}\text{Ge}_x$ layer. Kim *et al.* [187] formed tensile strained Si over $\text{Si}_{0.8}\text{Ge}_{0.2}$. The tensile Si was exposed to the anneal ambient. B was introduced in Si by ion implantation. Spike RTA annealing at 940°C resulted in retarded B diffusion in tensile strained Si when compared with the B diffusion in unstrained Si. The anneal ambient and the implantation energy and dose were however not reported.

These contradictory results together with the industrial importance of B doping in SiGe technology make the study of B diffusion in the Si-SiGe system of considerable interest. What is known of B diffusion in Si irrespective of the gaps in the data cited above also makes this an attractive system to probe point defect properties and interactions. It may therefore prove useful to correlate our data and model for void evolution with measurements of B diffusion to gain further insight into the mechanisms governing the void behaviour in the different samples. In this chapter, we report B diffusion in Si and in Si samples with a thin $\text{Si}_{0.95}\text{Ge}_{0.05}$ epilayer on top of Si. B was introduced by ion implantation and annealing was done in N_2 and dry O_2 . We attempt to

explain the results and attempt to make a correlation between the B diffusion data and the void evolution characteristics observed in similar samples in Chapter 4.

6.2 Experimental Details and Discussions

B⁺ implantations were done in {100} Si and in {100} Si capped with a 60 nm thin Si_{0.95}Ge_{0.05} epilayer (Si_{0.95}Ge_{0.05}/Si). The implantation was done at room temperature for a dose of 1×10^{13} cm⁻² at 60 keV. The beam was fixed at 7° off axis to minimize channelling during the implantation process. According to the Monte Carlo based ion implantation simulator SRIM [188], the B projected range is 204 nm with a straggle of 70 nm for the implantation conditions used. The implantation energy was selected so that the peak of the as-implanted B profile is formed inside Si for Si_{0.95}Ge_{0.05}/Si sample. The implantation dose was selected such that the material remains intrinsic at the anneal temperatures considered so that the diffusion is expected to be concentration independent.

We then annealed the samples at 1090°C in a rapid thermal annealer (RTA) for 15 min in N₂ to anneal out implantation damage and activate the implanted B. We then conducted a second anneal step in a furnace annealer (FA) at 970°C for 1 hour in N₂ or dry O₂. N₂ is considered to be an inert ambient as Si does not react with N₂ for annealing done up to 1150°C [65]. B concentration profiles were extracted by secondary ion mass spectroscopy (SIMS). Figure 6.1 shows the final B diffusion profiles after depth and concentration calibrations were done.

From Figure 6.1 we can observe that in Si samples, B diffusion is enhanced during annealing in dry O₂ compared with annealing done in N₂. This is nothing more than the

well established oxidation enhanced diffusion (OED) of B in Si resulting from interstitial injection during oxidation. When we compare the B diffusion profiles in $\text{Si}_{0.95}\text{Ge}_{0.05}/\text{Si}$ samples with the B diffusion profiles in Si, we notice two distinct differences. First, regardless of ambient, B diffusion is retarded in the $\text{Si}_{0.95}\text{Ge}_{0.05}/\text{Si}$ samples compared with the Si samples. Second, the enhancement in B diffusion during dry O_2 annealing compared with N_2 annealing in the $\text{Si}_{0.95}\text{Ge}_{0.05}/\text{Si}$ sample is less than the corresponding enhancement for the Si sample.

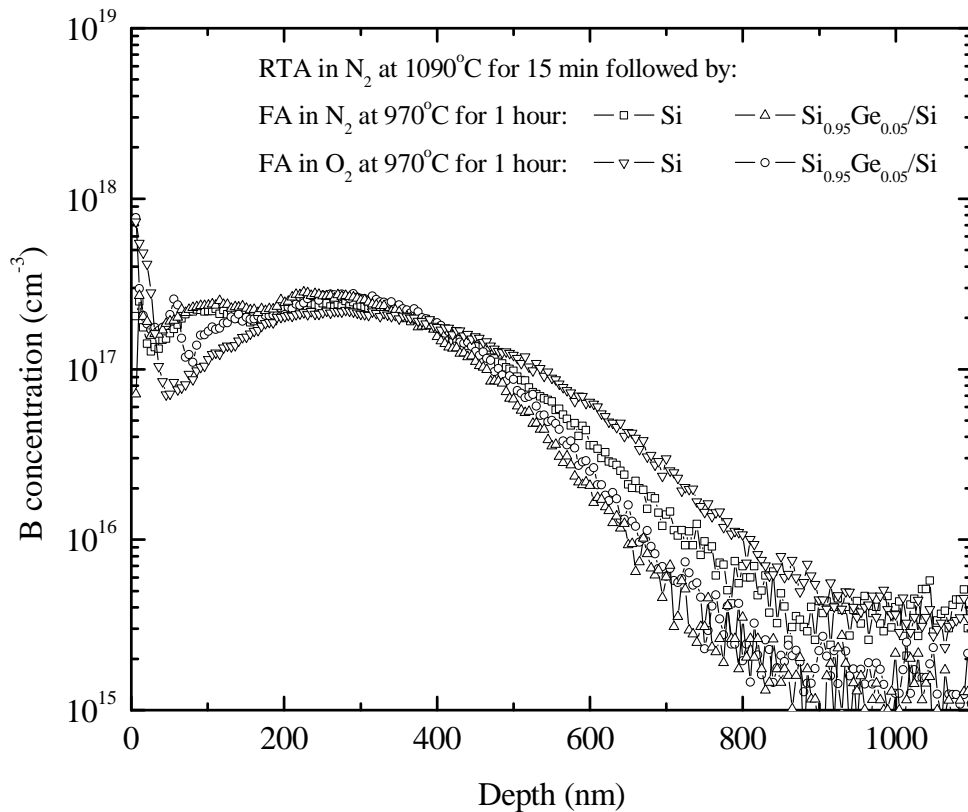


Figure 6.1. B SIMS profiles in Si and $\text{Si}_{0.95}\text{Ge}_{0.05}/\text{Si}$ samples annealed at 1090°C in RTA in N_2 for 15 min followed by FA done at 970°C for 1 hour in N_2 or dry O_2 .

We also implanted another set of $\text{Si}_{0.95}\text{Ge}_{0.05}/\text{Si}$ and Si wafers with 60 keV , $1 \times 10^{13} \text{ cm}^{-2} \text{ B}^+$ and annealed in RTA at 1000°C for 15 min in N_2 followed by annealing in RTA at 1050°C for 30 min in N_2 or dry O_2 . Figure 6.2 shows B SIMS profiles in the samples after depth and concentration calibration.

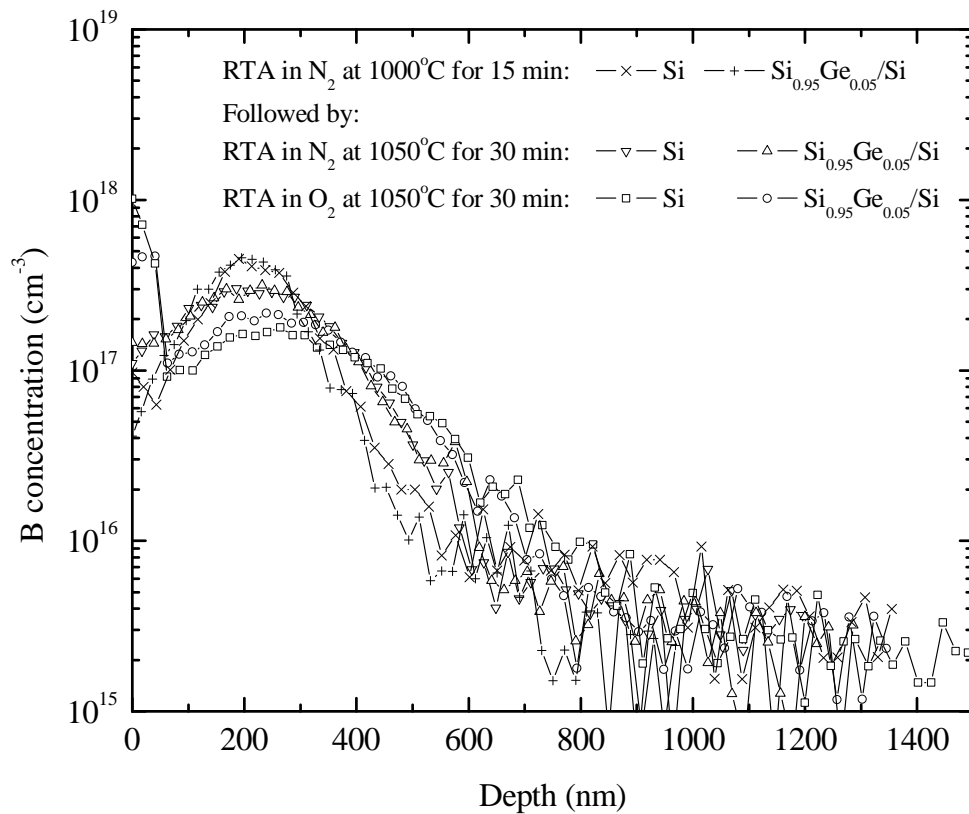


Figure 6.2. B SIMS profiles in Si and $\text{Si}_{0.95}\text{Ge}_{0.05}/\text{Si}$ samples annealed at 1000°C in RTA in N_2 for 15 min followed by RTA done at 1050°C for 30 min in N_2 or dry O_2 .

The diffusion behaviour in these samples is different from Figure 6.1. B diffusion profiles in $\text{Si}_{0.95}\text{Ge}_{0.05}/\text{Si}$ and Si samples after annealing done at 1050°C for 30 min in N_2 are similar. We also notice similar B diffusion profiles in $\text{Si}_{0.95}\text{Ge}_{0.05}/\text{Si}$ and Si samples after annealing done at 1050°C for 30 min in dry O_2 . B diffusion profiles in $\text{Si}_{0.95}\text{Ge}_{0.05}/\text{Si}$ and Si samples after the initial annealing was done at 1000°C for 15 min in N_2 were also extracted and we find that these two profiles are quite similar as well.

There are thus three experimental observations for B diffusion:

1. OED is observed for all cases. Given a particular sample structure and particular anneal conditions, annealing in dry O_2 results in greater diffusion than annealing in N_2 .
2. OED enhancement in $\text{Si}_{0.95}\text{Ge}_{0.05}/\text{Si}$ sample is less compared to Si sample for dry O_2 annealing done at 970°C for 1 hour. This annealing was a follow-up anneal step of the initial 1090°C RTA in N_2 for 15 min. We observed similar OED in Si and $\text{Si}_{0.95}\text{Ge}_{0.05}/\text{Si}$ samples for dry O_2 annealing done at 1050°C for 30 min. This stage was a follow-up of the initial annealing done at 1000°C in N_2 for 15 min.
3. Regardless of ambient, diffusion in the $\text{Si}_{0.95}\text{Ge}_{0.05}/\text{Si}$ structure is retarded in comparison to diffusion in Si for the case of the 1090°C RTA but not for the case of the 1000°C RTA.

The presence of $\text{Si}_{1-x}\text{Ge}_x$ as an epilayer can modify diffusion behaviour either due to strain or due to the presence of Ge. The latter could either modify surface behaviour or bulk behaviour.

The first possibility is the introduction of strain. The $\text{Si}_{1-x}\text{Ge}_x$ epilayer will be under compressive strain and the Si substrate close to interface will be under tensile strain. However, this cannot adequately explain any of the observed phenomena. Strain in the $\text{Si}_{1-x}\text{Ge}_x$ system is given by:

$$s = \left(1 - \frac{a_{\text{Ge}}}{a_{\text{Si}}}\right)x = \pm 0.042x \quad (6.1)$$

where the positive sign is for tensile strain and the negative sign is for compressive strain. Cowern *et al.* [189] modeled dopant diffusivity under strain using the relation:

$$D_{\text{strain}} = D_i \exp(-Q'_i s / kT) + D_v \exp(-Q'_v s / kT) \quad (6.2)$$

where, D_{strain} is the dopant diffusivity in strained material, D_i and D_v respectively are the interstitial and vacancy assisted dopant diffusivities in unstrained material, $Q'_i < 0$ and $Q'_v > 0$ are the changes in activation energy of (respectively) interstitial and vacancy mediated diffusion due to the presence of strain, s , k is Boltzmann constant and T is the anneal temperature in Kelvin. Finally, the equilibrium interstitial concentration is expected to increase under tensile strain. Given this understanding of the role of strain we conclude that it cannot explain the observed phenomena for a number of reasons. First, studies of strain in Si under nitride and oxide thin films show that the strain decays very rapidly into the substrate so that it is unlikely to affect the B peak, which is 144 nm under the interface. Secondly, even if the strain were extended into the substrate to that depth (e.g. due to diffusion of Ge) the expected magnitude of these effects would not be

sufficient to explain the observed phenomena. In particular the magnitude of Q' would not be sufficient to produce opposing trends due to the change in anneal temperature from 1000°C to 1090°C. Finally, the trend is actually the opposite of what is expected. The presence of OED in all cases indicates that for all our samples and anneal conditions, B is still primarily an interstitial diffuser. For interstitial diffusers $Q'_i < 0$ and $s > 0$ means that diffusion would be enhanced. For example, Kringhøj *et al.* [190] observed that diffusion of Sb, a vacancy diffuser in Si, is retarded under tensile strain.

The second possibility is the effect of Ge on surface phenomena. Napolitani *et al.* [147] have suggested that interstitial injection during dry oxidation is suppressed under $\text{Si}_{1-x}\text{Ge}_x$. We observed reduced enhancement of B diffusion in presence of $\text{Si}_{0.95}\text{Ge}_{0.05}$ epilayer when dry O_2 annealing was done at 970°C and is consistent with the suppressed interstitial injection phenomena reported by Napolitani *et al.* [147]. However, this cannot explain any of the other observed trends and cannot explain why the suppression has no effect for the case of the 1050°C RTA. A different surface effect is nitridation. Silicon at high temperature can react with N_2 to form a nitride film and inject vacancies. Assuming that this happens at an even lower temperature with $\text{Si}_{1-x}\text{Ge}_x$ could explain the retarded diffusion in the $\text{Si}_{0.95}\text{Ge}_{0.05}/\text{Si}$ structure under a nitriding anneal, but it is inconsistent with retarded diffusion in the $\text{Si}_{0.95}\text{Ge}_{0.05}/\text{Si}$ structure under oxidizing anneal, which is what is observed after the 970°C FA. It is also not possible to explain the observed trends by combining the effect of vacancy injection under inert anneal with suppressed interstitial injection under oxidizing anneal because such an explanation would predict that oxidizing ambient diffusion in a $\text{Si}_{0.95}\text{Ge}_{0.05}/\text{Si}$ sample should be enhanced to a certain degree

compared with an inert anneal in Si, which is contrary to what we observe. Finally, XTEM and EDX measurements of comparable samples used in our void studies showed no nitride film formed. We therefore dismiss the notion of low temperature vacancy injection under the N₂ ambient.

The remaining hypothesis is modification of bulk behaviour due to the presence of Ge. It is well documented that B diffusion is retarded in the presence of Ge. Our initial samples have the B peak 144 nm below the SiGe layer. So we must now take into account Si-Ge interdiffusion.

A mathematical model for Si-Ge interdiffusion is reported in ref. [40], which has been applied to wide range of experimentally reported Ge interdiffusion data. The model takes into account the vacancy exchange mechanism for Si-Ge interdiffusion to occur for anneal temperature below 1050°C. For anneal temperature above 1050°C, the model takes into account both vacancy exchange mechanism and interstitial assisted mechanism for Si-Ge interdiffusion to occur. We applied this model taking into account the experimental conditions considered in B diffusion experiments in this study. From FLOOPS-ISE simulations we calculated the as-implanted vacancy and interstitial profiles. While calculating the as-implanted vacancy and interstitial profiles, we took into account the dynamic annealing of as-implanted point defects and considered that 5.5% vacancies and interstitials remain in the sample after performing the ion implantation process. We used these profiles of vacancies and interstitials as the initial profiles for vacancies and interstitials in the Si-Ge interdiffusion model. The simulations were done for annealing at 1000°C and 1090°C for 15 min. The simulation results are shown in Figure 6.3.

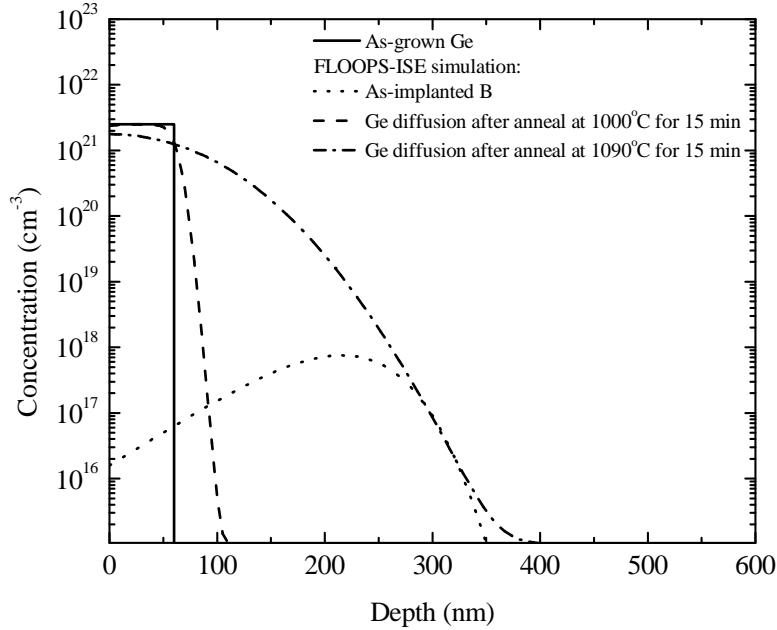


Figure 6.3. FLOOPS-ISE simulation of Ge interdiffusion after annealing for 15 min at 1000°C and 1090°C taking into account the damage created during 60 keV, $1 \times 10^{13} \text{ cm}^{-2} \text{ B}^+$ implantation.

From Figure 6.3 we find that Ge diffusion into Si is much higher for annealing done at 1090°C for 15 min when compared to Ge diffusion at 1000°C for 15 min. When annealing is done for 1090°C for 15 min, we notice that the tail of Ge interdiffusion profile reaches the as-implanted B layer which does not happen for annealing done at 1000°C for 15 min. The possible interaction between Ge and B can be a good explanation for the retarded B diffusion in $\text{Si}_{0.95}\text{Ge}_{0.05}/\text{Si}$ structure for the case of 1090°C RTA. Since Ge diffusion is much less for 1000°C RTA, we do not expect any interaction between Ge and B to occur and thus we observe similar B diffusion profiles in Si and $\text{Si}_{0.95}\text{Ge}_{0.05}/\text{Si}$ structure.

We can in fact correlate the B diffusion pattern with the void evolution experimental results discussed in Chapter 4. Our experiments to form voids in $\text{Si}_{0.95}\text{Ge}_{0.05}/\text{Si}$ samples were conducted in the temperature range of 1050-1110°C. We have shown in Figure 4.8 in Chapter 4 that Ge can interdiffuse into void layer and we believe that the presence of Ge and the stress gradient resulted in increase in average void diameter and decrease in average void density in $\text{Si}_{0.95}\text{Ge}_{0.05}/\text{Si}$ samples compared to the same in Si samples. For RTA annealing done at 1090°C we notice retardation in B diffusion occurs, which we believe is due to the Ge interdiffusion into B layer and the resulting interaction of between Ge and B. Thus, the ability of Ge to interdiffuse to void layer/B layer at the anneal temperatures considered resulted in the change in the experimental observations in $\text{Si}_{0.95}\text{Ge}_{0.05}/\text{Si}$ samples both in void evolution and B diffusion studies.

Next, Figure 6.4 shows the simulated Ge interdiffusion profile for annealing done at 1000°C for 30 min. In the simulation we considered as-implanted vacancy and interstitial profiles calculated from FLOOPS-ISE simulations for He^+ implantation conditions used in our void evolution study. We considered 5.5% vacancy and interstitials remain after the dynamic annealing process of the point defects.

If we look at Figure 4.7 (a) in Chapter 4 which shows a trend line on the variation of the average void diameter in $\text{Si}_{0.95}\text{Ge}_{0.05}/\text{Si}$ samples, the extrapolation of the trend line to lower temperature suggests that we should not see any difference in the average void diameter and void density in Si and $\text{Si}_{0.95}\text{Ge}_{0.05}/\text{Si}$ samples for anneal temperatures close to 1000°C. This behaviour is consistent with the hypothesis that it is the presence of Ge

that alters the void evolution process and from Figure 6.4 we find that Ge does not reach the cavity layer for annealing done at 1000°C for 30 min. We also did not notice any difference between B diffusion profiles between Si and Si_{0.95}Ge_{0.05}/Si samples in Figure 6.2 when initial RTA was done at 1000°C for 15 min and we have argued that the absence of interaction between Ge and B resulted in getting similar B diffusion profiles in Si and Si_{0.95}Ge_{0.05}/Si sample. The above discussions thus further show that there is a clear correlation between the results obtained in void evolution and B diffusion studies in Si_{0.95}Ge_{0.05}/Si samples.

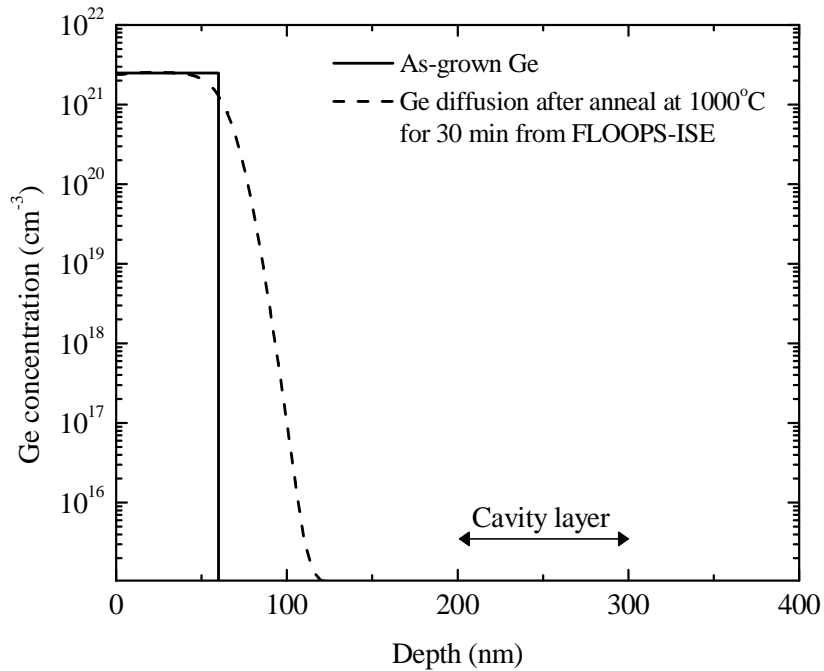


Figure 6.4. Ge interdiffusion after annealing for 30 min at 1000°C taking into account the damage created during 30 keV, $5 \times 10^{16} \text{ cm}^{-2}$ He⁺ implantation.

We observed different B diffusion behaviour under oxidizing ambient in the two experiments. SiGe oxidation kinetics can lead to the differences we notice. LeGoues *et al.* [142] reported formation of Ge-rich layer during dry oxidizing annealing of $\text{Si}_{0.85}\text{Ge}_{0.15}$ at 800 and 1000°C. The authors mentioned that the presence of Ge can relieve the stress created in the grown oxide layer, and thus can suppress injection of interstitials. Napolitano *et al.* [147] also proposed this as the mechanism responsible for the suppression of interstitial injection during the oxidation of SiGe. LeGoues' results suggest the formation of a Ge-rich layer for our experimental conditions where the samples were annealed in dry O_2 at 970°C for 1 hour, and hence a suppressed injection of interstitials in those samples. In contrast, Zhang *et al.* [191] characterized wet oxidation of $\text{Si}_{0.5}\text{Ge}_{0.5}$ at 1000°C and found that annealing done up to 10 min results in mixed oxide formation and no Ge-rich layer. Longer anneals produce pure SiO_2 and a Ge-rich layer. For our case, when dry O_2 annealing is done at 1050°C for a duration of 30 min (lower time duration compared to samples annealed at 970°C) and considering the lower Ge fraction present in our $\text{Si}_{1-x}\text{Ge}_x/\text{Si}$ samples compared with Zhang's results, we would expect no Ge-rich layer and no suppression of interstitial injection. These results would then consistently explain the difference between our two sets of samples.

In conclusion, we observe that for the experimental conditions considered in this study, annealing temperature can play a role in determining the experimental behaviour of B diffusion and void evolution mechanism in $\text{Si}_{0.95}\text{Ge}_{0.05}/\text{Si}$ samples. Annealing done at temperatures of 1050°C and above results in Ge from the $\text{Si}_{0.95}\text{Ge}_{0.05}$ epilayer in $\text{Si}_{0.95}\text{Ge}_{0.05}/\text{Si}$ samples to diffuse inside Si and reach void layer/B layer. The interaction of

Ge with void or with B results in the change in the experimental results observed in $\text{Si}_{0.95}\text{Ge}_{0.05}/\text{Si}$ samples. Annealing done at 1000°C for 15 min is not sufficient for Ge to diffuse into B layer, thus we did not observe any difference between the B diffusion profiles in Si and $\text{Si}_{0.95}\text{Ge}_{0.05}/\text{Si}$ samples. We expect void evolution for annealing done at 1000°C or at lower temperatures to be unaffected due to the presence of the $\text{Si}_{0.95}\text{Ge}_{0.05}$ epilayer in $\text{Si}_{0.95}\text{Ge}_{0.05}/\text{Si}$ samples.

Chapter 7

Conclusions

In this study a physically based mathematical model for void evolution during high dose helium ion implantation and subsequent annealing was proposed. The model correlates well with the underlying physical mechanisms that govern the void evolution process. The model was applied to the experimental results of void evolution observed in this study as well as to previously published experimental results of void diameter and void density available in literature. From our experimental results we noticed that the presence of $\text{Si}_{1-x}\text{Ge}_x$ epilayer can affect the void evolution process in Si. Further, annealing samples in N_2 or dry O_2 does not show any affect on the calculated values of average void diameter and average void density. We also carried out B diffusion studies in Si with $\text{Si}_{0.95}\text{Ge}_{0.05}$ epilayer present and used these studies as a probe to justify the role of $\text{Si}_{1-x}\text{Ge}_x$ epilayer on the void evolution process in Si.

7.1 Contributions

We studied the role of the presence of $\text{Si}_{1-x}\text{Ge}_x$ ($x = 0.05, 0.09$) epilayer on the void evolution process in Si. It was interesting to find that the $\text{Si}_{1-x}\text{Ge}_x$ epilayer plays a role on the void evolution process, as we attempted to form voids inside Si. We noticed a systematic affect of the presence of the $\text{Si}_{1-x}\text{Ge}_x$ epilayer. For all of our cases, in presence

of $\text{Si}_{1-x}\text{Ge}_x$ epilayer, our experimental results show increase in average void diameter and decrease in average void density when compared to the same in Si samples without any $\text{Si}_{1-x}\text{Ge}_x$ epilayer present. The diffusion of Ge from $\text{Si}_{1-x}\text{Ge}_x$ epilayer towards the cavity layer in $\text{Si}_{1-x}\text{Ge}_x/\text{Si}$ samples resulted in the change in the rate of migration and coalescence process of cavities and resulted in increase in average void diameter and decrease in average void density.

We studied the role of anneal ambient (N_2 and dry O_2) on the void evolution mechanism. As expected the change in anneal ambient did not show significant effect on the void evolution process.

To better understand the role of the $\text{Si}_{1-x}\text{Ge}_x$ epilayer on the void evolution process, we designed the B diffusion experiments in $\text{Si}_{0.95}\text{Ge}_{0.05}/\text{Si}$ samples. For annealing done above 1050°C we find that the presence of $\text{Si}_{0.95}\text{Ge}_{0.05}$ epilayer affects the B diffusion profiles. This finding is consistent with the role of $\text{Si}_{1-x}\text{Ge}_x$ epilayer on void evolution mechanism and further strengthens the arguments presented on void evolution process in $\text{Si}_{1-x}\text{Ge}_x/\text{Si}$ samples. The results of void evolution and B diffusion in $\text{Si}_{1-x}\text{Ge}_x/\text{Si}$ samples are correlated in the way that in both cases Ge interdiffuses from $\text{Si}_{1-x}\text{Ge}_x$ epilayer to Si and causes change in the behaviour of void evolution and B diffusion processes. B diffusion data also allows us to correlate the SiGe oxidation kinetics with the interstitials injected from surface during dry O_2 anneals.

We proposed a mathematical model to describe average void diameter and average void density in Si and $\text{Si}_{1-x}\text{Ge}_x/\text{Si}$ samples. We applied the model to our experimental results and to the experimental results available in literature. The simulated

results from the model are consistent with the experimental results for both isothermal and isochronal anneals. There is only one fitting parameter in the model and the fitting parameter represents the rate of migration and coalescence of cavities. The model facilitates understanding of the underlying physical mechanisms that govern the void evolution process through this fitting parameter. The activation energies of the fitting parameters from the simulated results are consistent with the activation energy of surface diffusivity of Si, the process which governs the migration and coalescence of cavities. The fitting parameter correlates well with the process conditions e.g., implantation energy and dose, anneal temperature, atmospheric pressure, anneal ramp rate, impurity level in silicon, the presence of Ge in the lattice, which affect the rate of migration and coalescence of cavities and thus affect the cavity evolution process.

The results obtained in this study were included in three journal papers. Two papers have been submitted for publication and the manuscript of the third paper is currently under preparation.

7.2 Suggestions for Future Work

In this study we have shown that the presence of a $\text{Si}_{1-x}\text{Ge}_x$ epilayer on Si influences the void evolution mechanism and can increase the average void diameter and decrease the average void density. While studying the role of the $\text{Si}_{1-x}\text{Ge}_x$ epilayer we focused on $\text{Si}_{1-x}\text{Ge}_x$ epilayer having 5% Ge. There was just one experiment done where the samples contained 5% and 9% Ge in the $\text{Si}_{1-x}\text{Ge}_x$ epilayer. The samples were annealed in RTA at 1060°C for 30 min in N_2 . Samples with 9% Ge in $\text{Si}_{1-x}\text{Ge}_x$ epilayer resulted in increase in void diameter and decrease in void density when compared with the values in

samples with 5% Ge in $\text{Si}_{1-x}\text{Ge}_x$ epilayer. In future, experiments in varying anneal temperatures with varying Ge concentration in the $\text{Si}_{1-x}\text{Ge}_x$ epilayer should be done to study how the variation in Ge fraction in $\text{Si}_{1-x}\text{Ge}_x$ epilayer can affect the void evolution process.

In our experimental work, He^+ implantation energy was set to 30 keV. Since we believe that Ge interdiffusion from $\text{Si}_{1-x}\text{Ge}_x$ epilayer into Si plays a role in the void evolution process, it can be expected that any change in the He^+ implantation energy will affect the void evolution process as well. Experiments can thus be carried out to study how the change in He^+ implantation condition may affect the void evolution in $\text{Si}_{1-x}\text{Ge}_x/\text{Si}$ samples. Another interesting study can be to attempt forming voids in $\text{Si}_{1-x}\text{Ge}_x$ and study the void evolution process.

He effusion kinetics from cavities can influence the cavity evolution process. He effusion in RTA can differ from that in FA. Roqueta *et al.* [92] reported that in RTA, He effusion is two times faster than in FA for the same He implantation dose. We also noticed from our experimental studies of void evolution that the average void diameter for annealing done in RTA can be higher than the average void diameter during annealing done in FA. The anneal ramp rate can particularly affect the void evolution process. In literature, we do not find any comprehensive study that compares the role of the type of furnace used in the void evolution mechanism. A comparative study can be done in future. The role of the change in the anneal ramp rate in RTA can influence the He effusion process and thus can be an attractive direction of experimental studies.

Finally, the model presented in this work can be extended to any new experimental results of void formation. In this study we focused on developing a model that describes the void evolution process due to annealing done at high temperature. We did not focus on how small vacancy clusters are formed during the ion implantation process. In future, attempts can be taken to develop a mathematical model to predict the evolution of small vacancy clusters during the He⁺ implantation process and can be tied with the mathematical model for void evolution proposed in this study.

References

- [1] G. E. Moore, *Electronics* **38** (1965).
- [2] J. D. Plummer, M. D. Deal, and P. B. Griffin, *Silicon VLSI Technology Fundamentals, Practice and Modeling* (Prentice Hall, Upper Saddle River, NJ, 2000).
- [3] International Technology Roadmap for Semiconductors (2001), <http://public.itrs.net>; access date June 6, 2010.
- [4] S. C. Jain, A. H. Harker, and R. A. Cowley, *Philos. Mag. A* **75**, 1461 (1997).
- [5] V. T. Bublik, S. S. Gorelik, A. A. Zaitsev, and A. Y. Polakov, *Phys. Stat. Sol. B* **65**, K79 (1974).
- [6] D. J. Paul, *Semicon. Sci. Technol.* **19**, R75 (2004).
- [7] M. V. Fischetti and S. E. Laux, *J. Appl. Phys.* **80**, 2234 (1996).
- [8] J. D. Cressler and G. Niu, *Silicon-Germanium Heterojunction Bipolar Transistors* (Artech House, Boston, MA, 2003).
- [9] FLOOPS-ISE Manual, Release 9.5, Integrated Systems Engineering.
- [10] A. Pakfar, *Mat. Sci. Engr. B* **89**, 225 (2002).
- [11] D. M. Follstaedt, S. M. Myers, G. A. Petersen, and J. W. Medernach, *J. Electron. Mater.* **25**, 151 (1996).
- [12] S. M. Myers, D. M. Bishop, D. M. Follstaedt, H. J. Stein, and W. R. Wampler, *Mater. Res. Soc. Symp. Proc.* **283**, 549 (1993).
- [13] G. A. Petersen, S. M. Myers, and D. M. Follstaedt, *Nucl. Instr. Meth. Phys. Res. B* **127-128**, 301 (1997).
- [14] F. Schiettekatte, C. Wintgens, and S. Roorda, *Appl. Phys. Lett.* **74**, 1857 (1999).

- [15] V. Raineri and S. U. Campisano, *Appl. Phys. Lett.* **69**, 1783 (1996).
- [16] V. Raineri and S. U. Campisano, *Nucl. Instr. Meth. Phys. Res. B* **120**, 56 (1996).
- [17] X. -Q. Feng and Y. Huang, *Int. J. Solids Struct.* **41**, 4299 (2004).
- [18] V. Raineri, *Mat. Sci. Engg. B* **73**, 47 (2000).
- [19] C. C. Griffioen, J. H. Evans, P. C. de Jong, and A. van Veen, *Nucl. Instr. Meth. Phys. Res. B* **27**, 417 (1987).
- [20] O. Qasaimeh, P. Bhattacharya, and E. T. Croke, *IEEE Photon. Technol. Lett.* **10**, 807(1998).
- [21] C. Engel, P. Baumgartner, M. Holzmann, J. F. Nützel, and G. Abstreiter, *Thin Solid Films* **294**, 347 (1997).
- [22] M. A. Rabie, Y. M. Haddara, and J. Carette, *J. Appl. Phys.* **98**, 074904(2005).
- [23] S. Rizk, Y. M. Haddara, and A. Sibaja-Hernandez, *J. Vac. Sci. Technol. B* **24**, 1365 (2006).
- [24] N. R. Zangenberg, J. Fage-Pedersen, J. L. Hansen, and A. N. Larsen, *J. Appl. Phys.* **94**, 3883(2003).
- [25] J. M. Bonar, A. F. W. Willoughby, A. H. Dan, B. M. McGregor, W. Lerch, D. Loeffelmacher, G. A. Cooke, and M. G. Dowsett, *J. Mater. Sci.: Mater. Electron.* **12**, 219 (2001).
- [26] Z. Di, M. Zhang, W. Liu, M. Zhu, C. Lin, and P. K. Chu, *Mater. Sci. Eng. B* **124–125**, 153 (2005).
- [27] C. C. Wang, Y. M. Sheu, S. Liu, R. Duffy, A. Heringa, N. E. B. Cowern, and P. B. Griffin, *Mater. Sci. Eng. B* **124–125**, 39 (2005).

- [28] M. Glück, A. Schüppen, M. Rösler, W. Heinrich, J. Hersener, U. König, O. Yam, C. Cytermann, and M. Eizenberg, *Thin Solid Films* **270**, 549(1995).
- [29] F. K. LeGoues, R. Rosenberg, T. Nguyen, F. Himpsel, and B. S. Meyerson, *J. Appl. Phys.* **65**, 1724(1989).
- [30] J. D. Cressler, D. L. Harame, J. H. Comfort, J. M. C. Stork, B. S. Meyerson, and T. E. Tice, *Dig. Tech. Pap.- IEEE Int. Solid-State Circuits Conf.* 1994, p 24.
- [31] L. J. van Ijzendoorn, G. F. A. van de Walle, A. A. van Gorkum, A. M. L. Theunissen, R. A. van den Heuvel, and J. H. Barrett, *Nucl. Inst. Meth. Phys. Res. B* **50**, 127 (1990).
- [32] H. Sunamura, S. Fukatsu, N. Usami, and Y. Shiraki, *Jpn. J. Appl. Phys.* **33**, 2344 (1994).
- [33] P. Zaumseil, U. Jagdhold, and D. Krüger, *J. Appl. Phys.* **76**, 2191(1994).
- [34] M. Griglione, T. J. Anderson, Y. M. Haddara, M. E. Law, K. S. Jones, and A. van den Bogaard, *J. Appl. Phys.* **88**, 1366 (2000).
- [35] M. Griglione, T. J. Anderson, M. E. Law, K. S. Jones, A. van den Bogaard, and M. P. Lambers, *J. Appl. Phys.* **89**, 2904 (2001).
- [36] B. Holländer, R. Butz, and S. Mantl, *Phys. Rev. B* **46**, 6975 (1992).
- [37] D. B. Aubertine and P. C. McIntyre, *J. Appl. Phys.* **97**, 013531 (2005).
- [38] N. Ozguven and P. C. McIntyre, *Appl. Phys. Lett.* **92**, 181907 (2008).
- [39] S. M. Prokes, O. J. Glembocki, and D. J. Godbey, *Appl. Phys. Lett.* **60**, 1087 (1992).
- [40] M. Hasanuzzaman and Y. M. Haddara, *J. Mater. Sci.: Mater. Electron.* **19**, 569 (2008).

- [41] M. Hasanuzzaman, Y. M. Haddara, and A. P. Knights, *J. Appl. Phys.* **105**, 043504 (2009).
- [42] M. Lannoo and J. Bourgoin, *Point Defects in Semiconductors I* (Springer-Verlag, New York, 1981).
- [43] S. Wolf and R. N. Tauber, *Silicon Processing for the VLSI Era Volume 1 – Process Technology* (Lattice Press, Sunset Beach, 1986).
- [44] P. M. Fahey, P. B. Griffin, and J. D. Plummer, *Rev. Mod. Phys.* **61**, 289 (1989).
- [45] K. H. Nicholas, *J. Phys. D* **9**, 393 (1976).
- [46] L. A. Miller, D. K. Brice, A. K. Prinja, and S. T. Picraux, *Radiat. Eff. Defects. Solids* **129**, 127 (1994).
- [47] L. Pelaz, L. A. Marqués, and J. Barbolla, *J. Appl. Phys.* **96**, 5947 (2004).
- [48] M. -J. Caturla, T. Diaz de la Rubia, L. A. Marqués, and G. H. Gilmer, *Phys. Rev. B* **54**, 16683 (1996).
- [49] J. S. Williams and J. M. Poate (Eds.), *Ion Implantation and Beam Processing* (Academic Press, Sydney, 1984).
- [50] A. P. Knights, F. Malik, and P. G. Coleman, *Appl. Phys. Lett.* **75**, 466 (1999).
- [51] B. G. Svensson, C. Jagadish, and J. S. Williams, *Phys. Rev. Lett.* **71**, 1860 (1993).
- [52] K. K. Larsen, V. Privitera, S. Coffa, F. Priolo, S. U. Campisano, and A. Camera, *Phys. Rev. Lett.* **76**, 1493 (1994).
- [53] G. D. Watkins and J. W. Corbett, *Phys. Rev.* **138**, A543 (1965).
- [54] E. Albertazzi, M. Bianconi, G. Lulli, R. Nipoti, A. Carnera, and C. Cellini, *Nucl. Instr. Meth. Phys. Res. B* **112**, 152 (1996).

- [55] F. H. Eisen and B. Welch, *Rad. Eff.* **7**, 143 (1971).
- [56] J. W. Cobett, J. Karins, and T. Y. Tan, *Nucl. Instr. Meth. Phys. Res. B* **182-183**, 457 (1981).
- [57] H. J. Stein, F. L. Vook, and J. A. Borders, *Appl. Phys. Lett.* **14**, 328 (1969).
- [58] W. Jung and H. S. Nwell, *Phys. Rev.* **132**, 648 (1963).
- [59] S. Solmi, F. Baruffaldi, and R. Canteri, *J. Appl. Phys.* **69**, 2135 (1991).
- [60] D. J. Eaglesham, P. A. Stolk, H. -J. Gossmann, and J. M. Poate, *Appl. Phys. Lett.* **65**, 2305 (1994).
- [61] K. H. Nicholas, *Solid State Electron.* **9**, 35 (1966).
- [62] G. Masetti, S. Solmi, and G. Soncini, *Solid State Electron.* **16**, 1419 (1973).
- [63] D. A. Antoniadis, A. G. Gonzalez, and R. W. Dutton, *J. Electrochem. Soc.* **125**, 813 (1978).
- [64] C. Hill, in H. R. Huff and R. J. Jriegler (Eds.), *Semiconductor Silicon*, 1981, p. 500.
- [65] R. Francis and P. S. Dobson, *J. Appl. Phys.* **50**, 280 (1979).
- [66] T. Y. Tan and B. J. Ginsberg, *Appl. Phys. Lett.* **42**, 448 (1983).
- [67] S. M. Hu, *J. Appl. Phys.* **45**, 1567 (1974).
- [68] S. T. Dunham and J. D. Plummer, *J. Appl. Phys.* **59**, 2551 (1986).
- [69] P. S. Dobson, *Philos. Mag.* **24**, 567 (1971).
- [70] S. Mizuo and H. Higuchi, *J. Electrochem. Soc.* **130**, 1942 (1983).
- [71] S. Mizuo, T. Kusaka, A. Shintani, M. Nanba, and H. Higuchi, *J. Appl. Phys.* **54**, 3860 (1983).
- [72] P. M. Fahey, R. W. Dutton, and M. Moslehi, *Appl. Phys. Lett.* **43**, 683 (1983).

- [73] P. M. Fahey, G. Barbuscia, M. Moslehi, and R. W. Dutton, *Appl. Phys. Lett.* **46**, 784 (1985).
- [74] T. K. Mogi, M. O. Thompson, H. -J. Gossmann, J. M. Poate, and H. S. Luftman, *Appl. Phys. Lett.* **69**, 1273 (1996).
- [75] M. S. A. Karunaratne, A. F. W. Willoughby, J. M. Bonar, J. Zhang, and P. Ashburn, *J. Appl. Phys.* **97**, 113531 (2005).
- [76] S. Mizuo and H. Higuchi, *Jpn. J. Appl. Phys.* **21**, 281 (1982).
- [77] K. Osada, Y. Zaitso, S. Matsumoto, M. Yoshida, E. Arai, and T. Abe, *J. Electrochem. Soc.* **142**, 202 (1995).
- [78] M. M. Moslehi and K. C. Sarawat, *IEEE Trans. Elec. Dev.* **32**, 106 (1985).
- [79] S. T. Ahn, H. W. Kennel, J. D. Plummer, and W. A. Tiller, *Appl. Phys. Lett.* **53**, 1593 (1988).
- [80] S. T. Ahn, H. W. Kennel, J. D. Plummer, and W. A. Tiller, *J. Appl. Phys.* **64**, 4914 (1988).
- [81] M. Hasanuzzaman and Y. M. Haddara, *J. Mater. Sci.: Mater. Electron.* **19**, 323 (2008).
- [82] E. Oliviero, S. Peripolli, P. F. P. Fichtner, and L. Amaral, *Mat. Sci. Engg. B* **112**, 111 (2004).
- [83] S. Peripolli, E. Oliviero, P. F. P. Fichtner, M. A. Z Vasconcellos, and L. Amaral, *Nucl. Instr. Meth. Phys. Res. B* **242**, 494 (2006).

- [84] S. Peripolli, L. Amaral, E. Oliviero, M. L. David, M. F. Beaufort, J. F. Barbot, L. Pichon, M. Drouet, P. F. P. Fichtner, and S. E. Donnelly, *Nucl. Instr. Meth. Phys. Res. B* **249**, 193 (2006).
- [85] C. A. Cima, H. Boudinov, J. P. de Souza, Y. Suprun-Belevich, and P. F. P. Fichtner, *J. Appl. Phys.* **88**, 1771 (2000).
- [86] D. Babonneau, S. Peripolli, M. -F. Beauffort, J. -F. Barbot, and J. -P. Simon, *Appl. Cryst.* **40**, s350 (2007).
- [87] M. Wittmer, J. Roth, P. Revesz, and J. W. Mayer, *J. Appl. Phys.* **49**, 5207 (1978).
- [88] A. G. Cullis, T. E. Seidel, and R. L. Meek, *J. Appl. Phys.* **49**, 5188 (1978).
- [89] M. Alatalo, M. J. Puska, and R. M. Nieminen, *Phys. Rev. B* **46**, 12806 (1992).
- [90] S. K. Estreicher, J. Weber, A. Derecskei-Kovacs, and D. S. Marynick, *Phys. Rev. B* **55**, 5037 (1997).
- [91] G. F. Cerofolini, F. Corni, S. Frabboni, C. Nobili, G. Ottaviani, and R. Tonini, *Mat. Sci. Engg* **27**, 1 (2000).
- [92] F. Roqueta, A. Grob, J. J. Grob, R. Jérisian, J. P. Stoquert, and L. Ventura, *Nucl. Instr. Meth. Phys. Res. B* **147**, 298 (1999).
- [93] D. J. Eaglesham, P. A. Stolk, H. -J. Gossmann, T. E. Haynes, and J. M. Poate, *Nucl. Instr. Meth. Phys. Res. B* **106**, 191 (1995).
- [94] J. L. Benton, S. Libertino, P. Kringoi, D. J. Eaglesham, J. M. Poate, and S. Coffa, *J. Appl. Phys.* **82**, 120 (1997).
- [95] V. Raineri, A. Battaglia, and E. Rimini, *Nucl. Instr. Meth. Phys. Res. B* **96**, 249 (1995).

- [96] V. Raineri, G. Fallica, and S. Libertino, *J. Appl. Phys.* **79**, 9012 (1996).
- [97] V. Raineri, S. Coffa, E. Szilágyi, J. Gyulai, and E. Rimini, *Phys. Rev. B* **61**, 937 (2000).
- [98] W. Fukarek and J. R. Kaschny, *J. Appl. Phys.* **86**, 4160 (1999).
- [99] V. Raineri, P. G. Fallica, G. Percolla, A. Battaglia, M. Barbagallo, and S. U. Campisano, *J. Appl. Phys.* **78**, 3727 (1995).
- [100] T. W. Simpson and I. V. Mitchell, *Appl. Phys. Lett.* **86**, 241907 (2005).
- [101] S. Frabboni, F. Corni, C. Nobili, R. Tonini, and G. Ottaviani, *Phys. Rev. B* **69**, 165209 (2004).
- [102] S. Godey, T. Sauvage, E. Ntsoenzok, H. Erramli, M. F. Beaufort, J. F. Barbot, and B. Leroy, *J. Appl. Phys.* **87**, 2158 (2000).
- [103] J. H. Evans, *Nucl. Instr. Meth. Phys. Res. B* **196**, 125 (2002).
- [104] J. R. Kaschny, P. F. P. Fichtner, A. Muecklich, U. Kreissig, R. A. Yankov, Koegler, A. B. Danilin, and W. Skorupa, *Mat. Res. Soc. Symp. Proc.* **469**, 451 (1997).
- [105] P. F. P. Fichtner, J. R. Kaschny, R. A. Yankov, A. Muecklich, U. Kreißig, and W. Skorupa, *Appl. Phys. Lett.* **70**, 732 (1997).
- [106] P. F. P. Fichtner, J. R. Kaschny, A. Kling, H. Trinkaus, R. A. Yankov, A. Muecklich, W. Skorupa, F. C. Zawislak, L. Amaral, M. F. da Silva, and J. C. Soares, *Nucl. Instr. Meth. Phys. Res. B* **136-138**, 460 (1998).
- [107] P. F. P. Fichtner, J. R. Kaschny, M. Behar, R. A. Yankov, A. Muecklich, and W. Skorupa, *Nucl. Instr. Meth. Phys. Res. B* **148**, 329 (1999).
- [108] M. W. Finis, A. van Veen, and L. M. Caspers, *Radiat. Eff.* **78**, 121 (1983).

- [109] P. F. P. Fichtner, A. Peeva, M. Behar, G. de M. Azevedo, R. L. Maltez, R. Koegler, and W. Skorupa, *Nucl. Instr. Meth. Phys. Res. B* **161-163**, 1038 (2000).
- [110] B. Pivac, O. Milat, P. Dubček, S. Bernstorff, F. Corni, C. Nobili, and R. Tonini, *Phys. Stat. Sol. A* **198**, 29 (2003).
- [111] R. Tonini, F. Corni, S. Frabboni, G. Ottaviani, and G. F. Cerofolini, *J. Appl. Phys.* **84**, 4802 (1998).
- [112] R. Krause-Rehberg, H.S. Leipner, *Positron Annihilation in Semiconductors: Defect Studies* (Springer, New York, 1999).
- [113] R. A. Hakvoort, A. van Veen, P. E. Mijnders, and H. Schutt, *Appl. Surf. Sci.* **85**, 271 (1995).
- [114] R. S. Brusa, G. P. Karwasz, N. Tiengo, A. Zecca, F. Corni, R. Tonini, and G. Ottaviani, *Phys. Rev. B* **61**, 10154 (2000).
- [115] F. Corni, C. Nobili, G. Ottaviani, R. Tonini, G. Calzolari, G. F. Cerofolini, and G. Queirolo, *Phys. Rev. B* **56**, 7331 (1997).
- [116] F. Corni, G. Calzolari, S. Frabboni, C. Nobili, G. Ottaviani, R. Tonini, G. F. Cerofolini, D. Leone, M. Servidori, R. S. Brusa, G. P. Karwasz, N. Tiengo, and A. Zecca, *J. Appl. Phys.* **85**, 1401 (1999).
- [117] F. A. Nichols, *J. Nucl. Mater.* **30**, 143 (1969).
- [118] J. H. Evans, A. van Veen, and C. C. Griffioen, *Nucl. Instr. Meth. Phys. Res. B* **28**, 360 (1987).
- [119] S. E. Donnelly, V. M. Vishnyakov, R. C. Birtcher, and G. Carter, *Nucl. Instr. Meth. Phys. Res. B* **175-177**, 132 (2001).

- [120] V. M. Vishnyakov, S. E. Donnelly, G. Carter, R. C. Birtcher, and L. Haworth, *Solid State Phenom.* **82-84**, 267 (2002).
- [121] V. Raineri, M. Saggio, and E. Rimini, *J. Mater. Res.* **15**, 1449 (2000).
- [122] G. W. Greenwood, A. J. E. Foremann, and D. E. Rimmer, *J. Nucl. Mater.* **4**, 305 (1959).
- [123] S. Chandrasekhar, *Rev. Mod. Phys.* **15**, 1 (1943).
- [124] M. F. Beaufort, E. Oliviero, H. Garem, S. Godey, E. Ntsoenzok, C. Blanchard, and J. F. Barbot, *Phil. Mag. B* **80**, 1975 (2000).
- [125] E. Oliviero, M. F. Beaufort, and J. F. Barbot, *J. Appl. Phys.* **89**, 5332 (2001).
- [126] E. Oliviero, M. F. Beaufort, and J. F. Barbot, *J. Appl. Phys.* **90**, 1718 (2001).
- [127] M. L. David, M. F. Beaufort, and J. F. Barbot, *J. Appl. Phys.* **93**, 1438 (2003).
- [128] E. Oliviero, M. L. David, M. F. Beaufort, J. F. Barbot, and A. van Veen, *Appl. Phys. Lett.* **81**, 4201 (2002).
- [129] M. L. David, A. Ratchenkova, E. Oliviero, M. F. Denanot, M. F. Beaufort, A. Declémy, C. Blanchard, N. N. Gerasimenko, and J. F. Barbot, *Nucl. Instr. Meth. Phys. Res. B* **198**, 83 (2002).
- [130] D. L. da Silva, P. F. P. Fichtner, A. Peeva, M. Behar, R. Koegler, and W. Skorupa, *Nucl. Instr. Meth. Phys. Res. B* **175-177**, 335 (2001).
- [131] D. L. da Silva, P. F. P. Fichtner, M. Behar, A. Peeva, R. Koegler, and W. Skorupa, *Nucl. Instr. Meth. Phys. Res. B* **190**, 756 (2002).
- [132] D. L. da Silva, M. J. Mörschbacher, P. F. P. Fichtner, E. Oliviero, and M. Behar, *Nucl. Instr. Meth. Phys. Res. B* **219-220**, 713 (2004).

- [133] H. Trinkaus, in S. E. Donnelly and J. H. Evans (Eds.), Proc. NATO Adv. Res. Workshop on Fundamental Aspects of Inert Gases in Solids, Plenum, NY, 1991, p. 369.
- [134] V. Raineri and M. Saggio, Appl. Phys. Lett. **71**, 1673 (1997).
- [135] A. Misiuk, J. Bak-Misiuk, I. V. Antonova, V. Raineri, A. Romano-Rodriguez, A. Bachrouri, H. B. Surma, J. Ratajczak, J. Katcki, J. Adamczewska, and E. P. Neustroev, Comp. Mat. Sci. **21**, 515 (2001).
- [136] A. Misiuk, J. Bak-Misiuk, M. Kaniewska, K. S. Zhuravlev, V. Raineri, and I. V. Antonova, Mater. Phys. Mech. **5**, 31 (2002).
- [137] J. Bak-Misiuk, A. Misiuk, A. Shalimov, B. Surma, V. G. Zavodinsky, A. A. Gnidenko, B. Lament-Bialek, and A. Wnuk, J. Alloys Compd. **401**, 231 (2005).
- [138] M. K. Weldon, V. E. Marsico, Y. J. Chabal, A. Agarwal, D. J. Eaglesham, J. Sapjeta, W. L. Brown, D. C. Jacobson, Y. Caudano, S. B. Christman, and E. E. Chaban, J. Vac. Sci. Technol. B **15**, 1065 (1997).
- [139] W. S. Liu, G. Bai, M. -A. Nicolet, C. H. Chern, V. Arbet, and K. L. Wang, Mater. Res. Soc. Symp. Proc. **220**, 259 (1991).
- [140] W. S. Liu, E. W. Lee, M. A. Nicolet, V. Arbet-Engels, K. L. Wang, N. M. Abuhadba, and C. R. Aita, J. Appl. Phys. **71**, 4015 (1992).
- [141] S. J. Kilpatrick, R. J. Jaccodine, and P. E. Thompson, J. Appl. Phys. **81**, 8018 (1997).
- [142] F. K. LeGoues, R. Rosenberg, and B. S. Meyerson, Appl. Phys. Lett. **54**, 644 (1989).
- [143] D. Fathy, O. W. Holland, and C. W. White, Appl. Phys. Lett. **51**, 1337 (1987).

- [144] E. C. Frey, N. R. Parikh, M. L. Swanson, M. Z. Numan, and W. K. Chu, *Proc. Mater. Res. Soc. Symp.* **105**, 277 (1988).
- [145] D. C. Paine, C. Caragianis, and A. F. Schwartzman, *J. Appl. Phys.* **70**, 5076 (1991).
- [146] D. A. Abdulmalik, P. G. Coleman, H. Z. Su, Y. M. Haddara, and A. P. Knights, *J. Mater. Sci.: Mater. Electron.* **18**, 753 (2007).
- [147] E. Napolitani, M. Di Marino, D. De Salvador, A. Carnera, M. Spadafora, S. Mirabella, A. Terrasi, and S. Scalese, *J. Appl. Phys.* **97**, 036106 (2005).
- [148] M. D. Griglione, PhD Thesis, University of Florida, 1999.
- [149] M. V. Speight, *J. Nucl. Mater.* **58**, 55 (1975).
- [150] D. R. Olander, *J. Nucl. Mater.* **92**, 163 (1980).
- [151] V. A. Fedorov, PhD Thesis, Delft University, The Netherlands (2000).
- [152] A. V. Fedorov and A van Veen, *Comp. Mat. Sci.* **9**, 309 (1998).
- [153] A. V. Fedorov, A. van Veen, and J. Th. De Hosson, *Mat. Res. Soc. Symp. Proc.* **439**, 383 (1997).
- [154] M. E. Law and K. S. Jones, *Int. Elec. Dev. Meet. 2000 Tech. Dig.*, pp. 511-514.
- [155] P. J. Goodhew and S. K. Tyler, *Proc. R. Soc. Lond. A, Math. Phys. Sci.* **377**, 151 (1981).
- [156] J. R. Kaschny, P. F. P. Fichtner, A. Muecklich, U. Kreissig, R. A. Yankov, and W. Skorupa, *Nucl. Instr. Meth. Phys. Res. B* **136-138**, 583 (1998).
- [157] G. F. Cerofolini, G. Calzolari, F. Corni, S. Frabboni, C. Nobili, G. Ottaviani, and R. Tonini, *Phys. Rev. B* **61**, 10183 (2000).
- [158] A. La Magna, S. Coffa, and L. Colombo, *Phys. Rev. Lett.* **82**, 1720 (1999).

- [159] J. L. Ngau, P. B. Griffin, and J. D. Plummer, *J. Appl. Phys.* **90**, 1768 (2001).
- [160] M. E. Law, Y. M. Haddara, and K. S. Jones, *J. Appl. Phys.* **84**, 3555 (1998).
- [161] A. S. Dalton, D. Llera-Hurlburt, and E. G. Seebauer, *Surf. Sci.* **494**, L761-L766 (2001).
- [162] L. J. Perryman and P. J. Goodhew, *Acta Metall.* **36**, 2685 (1988).
- [163] E. Y. Mikhlin, *Phys. Stat. Sol. A* **56**, 763 (1979).
- [164] P. M. Mooney, *Electrochem. Soc. Interface* **14**, 36 (2005).
- [165] T. Y. Tan and U. Gösele, *Appl. Phys. Lett.* **40**, 616 (1982).
- [166] A. Antoniadis and I. Moskowitz, *J. Appl. Phys.* **53**, 6788 (1982).
- [167] U. Gösele and H. Strunk, *Appl. Phys.* **20**, 263 (1979).
- [168] T. Y. Tan, U. Gösele, and F. F. Morehead, *Appl. Phys. A* **31**, 108 (1983).
- [169] M. J. Aziz, *Appl. Phys. Lett.* **70**, 2810 (1997).
- [170] S. Chaudhry and M. E. Law, *J. Appl. Phys.* **82**, 1138 (1997).
- [171] A. D. N. Paine, M. Morookz, A. F. W. Willoughby, J. M. Bonar, P. Phyllips, M. G. Dowsett, and G. Cooke, *Mater. Sci. Forum* **196–201**, 345 (1995).
- [172] S. Uppal, A. F. W. Willoughby, J. M. Bonar, A. G. R. Evans, N. E. B. Cowern, R. Morris, and M. G. Dowsett, *Physica B* **308–310**, 525 (2001).
- [173] R. F. Lever, J. M. Bonar, and A. F. W. Willoughby, *J. Appl. Phys.* **83**, 1988 (1998).
- [174] P. Kuo, J. L. Hoyt, J. F. Gibbons, J. E. Turner, and D. Lefforge, *Appl. Phys. Lett.* **66**, 580 (1995).
- [175] P. Kuo, J. L. Hoyt, J. F. Gibbons, J. E. Turner, R. D. Jacowitz, and T. L. Kamins, *Appl. Phys. Lett.* **62**, 612 (1993).

- [176] P. Kuo, J. L. Hoyt, J. F. Gibbons, J. E. Turner, R. D. Jacowitz, and D. Lefforge, *Mater. Res. Soc. Symp. Proc.* **379**, 373 (1995).
- [177] N. R. Zangenberg, J. Fage-Pedersen, J. Lundsgaard Hansen, and A. Nylandsted Larsen, *Defect Diffus. Forum* **194–199**, 703 (2001).
- [178] W. T. Fang, P. B. Griffin, and J. D. Plummer, *Mater. Res. Soc. Symp. Proc.* **379**, 379 (1995).
- [179] L. Radic, A. F. Saavedra, K. S. Jones, and M. E. Law, *J. Vac. Sci. Technol. B* **24**, 478 (2006).
- [180] S. Peterström and B. G. Svensson, *J. Appl. Phys.* **71**, 1215 (1992).
- [181] J. Bang, J. Kang, W. -J. Lee, and K. J. Chang, *Phys. Rev. B* **76**, 064118 (2007).
- [182] L. Wang, P. Clancy, and C. S. Murthy, *Phys. Rev. B* **70**, 165206 (2004).
- [183] L. Lin, T. Kirichenko, B. R. Sahu, G. S. Hwang, and S. K. Banerjee, *Phys. Rev. B* **72**, 205206 (2005).
- [184] M. J. Aziz, *Mat. Sci. Semicond. Proc.* **4**, 397 (2001).
- [185] M. J. Aziz, *Proc. 2003 IEEE Int. Conf. on Simulation of Semiconductor Processes and Devices*, Boston, MA, pp 137-42.
- [186] Y. Zhao, M. J. Aziz, H. -J. Gossmann, S. Mitha, and D. Schiferl, *Appl. Phys. Lett.* **74**, 31 (1999).
- [187] Y. -K Kim, K. -Sun Yoon, J. -S. Kim, and T. Won, *Jpn. J. Appl. Phys.* **46**, 2519 (2007).
- [188] <http://www.srim.org>; access date December 6, 2010.

[189] N. E. B. Cowern, P. C. Zalm, P. van der Sluis, D. J. Gravesteijn, and W. B. de Boer, *Phys. Rev. Lett.* **72**, 2585 (1994).

[190] P. Kringhøj, A. N. Larsen, and S. Y. Shirayey, *Phys. Rev. Lett.* **76**, 3372 (1996).

[191] J. P. Zhang, P. L. F. Hemment, S. M. Newstead, A. R. Powell, T. E. Whall, and E. H. C. Parker, *Thin Solid Films* **222**, 141 (1992).

[192] R. Peck, C. Olsen, and J. L. Devore, *Introduction to Statistics and Data Analysis* (Fourth Ed. 2012, Brooks/Cole, USA)

Appendix A

Statistical Analysis of Numerical Data

A.1 Statistical parameters

Frequency distribution is an efficient method in summarizing and interpreting numerical data. The shape of the frequency distribution gives an overall sense on the data set. One particular property of frequency distribute of data set is the number of peaks in the distribution, which is known a “mode”. A “unimodal” distribution is referred as a symmetric distribution if one half of the distribution is symmetric to the other half. A unimodal distribution that is not symmetric is known as “skewed” distribution. A distribution is referred as “positively skewed” if the upper tail of the distribution is stretched out more than the lower tail of the distribution. The opposite happens for a “negatively skewed” distribution. A symmetric, bell shaped distribution is commonly referred as “normal distribution”. The variability of data set is described in terms of different parameters which we describe next.

Mean, \bar{X} refers to the arithmetic average of the data set, the sum of the values in the data set divided by the total number of data. Mean value of a data set can be considered as the most representative value for the entire data set.

$$\bar{X} = \frac{\sum_{i=1}^N X_i}{N} \quad (\text{A.1})$$

where, X_i refers to individual values and N is the total number of data.

Standard deviation, S is a measure of the variability in the data set. A large value of S indicates large variability in the data set.

$$S = \sqrt{\frac{\sum_{i=1}^N (X_i - \bar{X})^2}{N-1}} \quad (\text{A.2})$$

The combination of mean and standard deviation can give an idea on how values in a data set are distributed and the relative position of a particular value in a data set.

Another important parameter associated is the sampling distribution of the calculated mean value. If the data set is normally distributed, the distribution of the mean value calculated from samples will be normally distributed. Even if the distribution of data set is not normal, the mean value from sample set is normally distributed if the number of samples considered is at least 30 [192]. The standard error can be calculated using the following formula.

$$\text{Standard error (SE)} = \frac{S}{\sqrt{N}} \quad (\text{A.3})$$

Once standard error is calculated, the mean values can be considered to range from mean-SE to mean+SE. The larger is the sample size, the lower is the value of standard error, which means that the error involved in the calculated mean is smaller. The value of standard error is often multiplied with 1.96 to set a 95% confidence level.

A.2 Hypothesis Test for Comparing Mean Values of Two Data Sets

When the sample size is large (>30) or the data set follows normal distribution, two sample t test can be used to compare mean values of two different data sets. The two data sets considered must be independent of each other and are randomly selected. Following is the summary of the two sample t test to compare two data sets.

$$\text{Test statistic, } t = \frac{\bar{X}_1 - \bar{X}_2 - H_0}{\sqrt{\frac{S_1^2}{N_1} + \frac{S_2^2}{N_2}}} \quad (\text{A.4})$$

where, subscripts 1 and 2 refer to parameters corresponding to two samples, $H_0 = \mu_1 - \mu_2 =$ hypothesized value. μ_1 and μ_2 are the actual mean values of the data sets considered.

and,

$$df = \frac{(V_1 + V_2)^2}{\frac{V_1^2}{N_1 - 1} + \frac{V_2^2}{N_2 - 1}} \quad (\text{A.5})$$

$$\text{where, } V_1 = \frac{S_1^2}{N_1} \text{ and } V_2 = \frac{S_2^2}{N_2}$$

The calculated value of df is truncated to the nearest integer.

Next P value is calculated from the area under t curve considering the value of df and hypothesis conclusion is taken comparing P value with the significance level set. If

the calculated P value is less than the set significance level, the hypothesis considered is rejected and the alternate hypothesis is accepted. For the case where the calculated value of P is greater than the significance level, the considered hypothesis is accepted.

A.2.1 Application to Experimental Results in Chapter 4

We applied two sample t test with unequal variances to check whether the difference in the mean values of void diameter those we observed between Si and Si_{0.95}Ge_{0.05}/Si samples are indeed validated by the hypothesis test. Following are the results of the hypothesis test suggesting that the calculated average void diameter between Si and Si_{0.95}Ge_{0.05}/Si samples are different.

t-Test: Two-Sample Assuming Unequal Variances	α	0.01					
Unequal Sample Sizes							
	<i>Data1</i>	<i>Data2</i>					
Mean	16.73691	21.5721					
Variance	46.01184	47.41868					
Observations	652	653					
Hypothesized Mean Difference	0						
df	1303						
t Stat	-12.778						
P(T<=t) one-tail	0.000		Reject Null Hypothesis because p < 0.01 (Means are Different)				
T Critical one-tail	2.329						
P(T<=t) two-tail	0.000		Reject Null Hypothesis because p < 0.01 (Means are Different)				
T Critical Two-tail	2.580						

Figure A.1. Two sample t test output for Si and Si_{0.95}Ge_{0.05}/Si samples RTA annealed at 1050°C for 15 min.

t-Test: Two-Sample Assuming Unequal Variances	α	0.01					
Unequal Sample Sizes							
	<i>Data1</i>	<i>Data2</i>					
Mean	17.97701	25.43191					
Variance	100.756	82.22179					
Observations	652	654					
Hypothesized Mean Difference	0						
df	1290						
t Stat	-14.082						
P(T<=t) one-tail	0.000		Reject Null Hypothesis because $p < 0.01$ (Means are Different)				
T Critical one-tail	2.329						
P(T<=t) two-tail	0.000		Reject Null Hypothesis because $p < 0.01$ (Means are Different)				
T Critical Two-tail	2.580						

Figure A.2. Two sample t test output for Si and Si_{0.95}Ge_{0.05}/Si samples FA annealed at 1080°C for 30 min.

t-Test: Two-Sample Assuming Unequal Variances	α	0.01					
Unequal Sample Sizes							
	<i>Data1</i>	<i>Data2</i>					
Mean	20.75416	26.64036					
Variance	116.618	139.3354					
Observations	659	656					
Hypothesized Mean Difference	0						
df	1302						
t Stat	-9.433						
P(T<=t) one-tail	0.000		Reject Null Hypothesis because $p < 0.01$ (Means are Different)				
T Critical one-tail	2.329						
P(T<=t) two-tail	0.000		Reject Null Hypothesis because $p < 0.01$ (Means are Different)				
T Critical Two-tail	2.580						

Figure A.3. Two sample t test output for Si and Si_{0.95}Ge_{0.05}/Si samples FA annealed at 1110°C for 30 min.

Appendix B

B.1 FLOOPS-ISE Simulation Code for Void Modeling

```
### Void modeling simulation code for annealing done for 30 min at 1060C for 30 keV,  
#### 5e16 He+ implantation
```

```
pdbSetSwitch Silicon Dopant DiffModel Pair  
pdbSetSwitch Gas_Silicon Vac BoundaryCondition Natural  
pdbSetSwitch Gas_Silicon Int BoundaryCondition Natural  
pdbSet Gas_Silicon Vac Ksurf 1  
pdbSet Gas_Silicon Int Ksurf 1  
  
line x loc=0.0 tag=surf spac=0.005  
line x loc=1.5 spac=0.005  
line x loc=2 spac=1  
line x loc=500 tag=back  
region Silicon xlo=surf xhi=back  
init  
  
solution name=Dvoid !negative !damp solve add  
solution name=Cvoid !negative !damp solve add  
solution name=Isize !negative !damp solve add  
solution name=diameter !negative !damp solve add  
solution name=Csv !negative !damp solve add  
solution name=covolume !negative !damp solve add  
solution name=heconc !negative !damp solve add  
solution name=x !negative !damp solve add  
  
profile name=heconc inf=/home/mhzaman/void/he_5e16_30kev.txt  
profile name=Vac inf=/home/mhzaman/void/vac_5e16_30kev.txt  
profile name=Int inf=/home/mhzaman/void/int_5e16_30kev.txt  
profile name=Csv inf=/home/mhzaman/void/sv_5e16_30kev.txt  
profile name=Cvoid inf=/home/mhzaman/void/initial_cvoid.txt  
profile name=Dvoid inf=/home/mhzaman/void/initial_dvoid.txt  
  
#### Parameters for He effusion kinetics ####  
set T 1060  
set new_int 2e13  
set l_int 1.62e-8  
set Csi 5e22  
set l_cavity 5e-6
```

```

set v_cavity 3e-6
set h 4.135667e-15
set kB 8.617343e-5
set x_cavity 2.5e-5
set Cs [expr double($Csi*(1-($v_cavity/$l_cavity)))]
set h1 6.62606896e-34
set kB1 1.3806504e-23
set m_he 6.645e-27
set lamda_T [expr double(100*$h1/sqrt(2*3.14*$m_he*$kB1*($T+273)))]
set A [expr
double(($new_int*$l_int*$l_int*$Cs*($lamda_T*$lamda_T*$lamda_T))\
/($v_cavity*$x_cavity))]
set B [expr double(exp(-$h*$new_int/(2*$kB*($T+273)))/(1-\
exp(-$h*$new_int/($kB*($T+273)))))]
set kai 1.92e-9
set w 12
set k 1.122
set w1 3000
set e [expr double(exp((-1.83/($kB*($T+273)))))]
set c 1.1327e-24

```

Parameters for void modeling

```

pdbSet Silicon Vac Cstar 5.68424e11
set eqvoid 5.68424e11
set eqsv 5.68424e11
set ksv 3.900e-11
set size 10
set size1 11
set Dvac 3.4642e-5
set Dint 9.32849e-7
set ksi 7.18365e-13
set four_pi 12.566

```

Fitting parameter of the void model

```

set k1 7.3e1

```

Setting the equations for He effusion kinetics

```

pdbSetString Silicon covolume Equation "covolume-\
1/((1/$c)+(1/((2/3)*3.14*($k*(heconc^(-1/3))- $kai*2.4849)^3)))"
pdbSetString Silicon x Equation "x-heconc/(1-covolume*heconc)"
pdbSetString Silicon heconc Equation\
"ddt(heconc)+$A*$B^3*x*exp(x*covolume)*$e*exp(6*($w1*\
exp(-$k*(heconc^(-1/3))/ $kai))/( $kB*($T+273)))"

```

```

set i_he 0
set j_sv 0
set k_void 0
set he_val_test 0
set he_time 0
set terminate_loop 0
set p 0
set tsum 0
set timeprev(0) 0
set totaltime 0
set prevtotaltime 0
set l 0

#### Void modeling equations
pdbSetString Silicon Isize Equation "Isize-Dvoid/Cvoid"
pdbSetString Silicon Dvoid Equation\
    "ddt(Dvoid)+$k1*Dvoid*Isize-$ksv*Csv*Vac"
pdbSetString Silicon diameter Equation\
    "diameter-2*(((3/4)*(Cvoid/Dvoid)*2e-23)/3.14)^(1/3)"
set time_step 1e-6
set new_time_step 1e-6

#### Check equation conditions####
while {$p<=60} {
incr p

set loop_cond 0
select z=heconc
set aslist [lindex [slice x=0] 0]
while {$loop_cond==0} {
    set c_he [lindex $aslist $i_he]
    incr i_he 2
    set d_he [lindex $aslist $i_he]
    if {($c_he <= 0.25) && ($d_he >=0.25)} {
        incr i_he
        set e_he [lindex $aslist $i_he]
        set loop_cond -1
    }
}
set i_he 0
set loop_cond 0

select z=Csv

```

```

set alist1 [lindex [slice x=0] 0]
while {$loop_cond==0} {
    set c_sv [lindex $alist1 $j_sv]
    incr j_sv 2
    set d_sv [lindex $alist1 $j_sv]
    if {($c_sv <= 0.25) && ($d_sv >=0.25)} {
        incr j_sv
        set e_sv [lindex $alist1 $j_sv]
        set loop_cond -1
    }
}
set j_sv 0
set loop_cond 0

select z=Cvoid
set alist2 [lindex [slice x=0] 0]
while {$loop_cond==0} {
    set c_void [lindex $alist2 $k_void]
    incr k_void 2
    set d_void [lindex $alist2 $k_void]
    if {($c_void <= 0.25) && ($d_void >=0.25)} {
        incr k_void
        set e_void [lindex $alist2 $k_void]
        set loop_cond -1
    }
}
set k_void 0
set loop_cond 0

if {$e_he<=0.01*$e_void && $e_he<=0.01*$e_sv} {
    pdbSetString Silicon Cvoid Equation "ddt(Cvoid)-\
    $Dvac*($four_pi)*(((1/Isz)^1/3)*(1.684e-8))+0.25e-7)*Dvoid*(Vac-EqVac)-\
    $size1*$ksv*Csv*Vac+$Dint*($four_pi)*(((1/Isz)^1/3)*(1.684e-8))+0.25e-\
    7)*Dvoid*(Int-EqInt)"
    pdbSetString Silicon Csv Equation "ddt(Csv)-$ksv*Csv*(Vac-\
    $eqsv)+$size*$ksv*Csv*Vac+$ksi*Csv*(Int-EqInt)"

    pdbSetString Silicon Int EquationProc IntDefectBulk
    proc IntDefectBulk {mat sol} {
        set pdbMat [pdbName $mat]
        set Dint 9.32849e-7
        set four_pi 12.566
        set ksi 7.18365e-13
        set kbulk 1.7000e-11
    }
}

```

```

        pdbSetString $pdbMat $sol Equation "ddt($sol)-\
$Dint*EqInt*grad($sol/EqInt)+$kbulk*($sol*Vac-\
EqInt*EqVac)+$Dint*($four_pi)*(((1/Isiz)^1/3)*(1.684e-8))+0.25e-7)*Dvoid*($sol-\
EqInt)+$ksi*Csv*($sol-EqInt)"
    }
} elseif {$e_he<=0.01*$e_void && $e_he>0.01*$e_sv} {
    pdbSetString Silicon Cvoid Equation "ddt(Cvoid)-\
$Dvac*($four_pi)*(((1/Isiz)^1/3)*(1.684e-8))+0.25e-7)*Dvoid*(Vac-EqVac)-\
$size1*$ksv*Csv*Vac+$Dint*($four_pi)*(((1/Isiz)^1/3)*(1.684e-8))+\
0.25e-7)*Dvoid*(Int-EqInt)"
    pdbSetString Silicon Csv Equation "ddt(Csv)-$ksv*Csv*(Vac-\
$eqsv)+$size*$ksv*Csv*Vac"

    pdbSetString Silicon Int EquationProc IntDefectBulk
    proc IntDefectBulk {mat sol} {
        set pdbMat [pdbName $mat]
        set Dint 9.32849e-7
        set four_pi 12.566
        set ksi 7.18365e-13
        set kbulk 1.7000e-11
        pdbSetString $pdbMat $sol Equation "ddt($sol)-\
$Dint*EqInt*grad($sol/EqInt)+$kbulk*($sol*Vac-\
EqInt*EqVac)+$Dint*($four_pi)*(((1/Isiz)^1/3)*(1.684e-8))+0.25e-7)*Dvoid*($sol-\
EqInt)"
    }
} elseif {$e_he>0.01*$e_void && $e_he<=0.01*$e_sv} {
    pdbSetString Silicon Cvoid Equation "ddt(Cvoid)-\
$Dvac*($four_pi)*(((1/Isiz)^1/3)*(1.684e-8))+0.25e-7)*Dvoid*(Vac-EqVac)-\
$size1*$ksv*Csv*Vac"
    pdbSetString Silicon Csv Equation "ddt(Csv)-$ksv*Csv*(Vac-\
$eqsv)+$size*$ksv*Csv*Vac+$ksi*Csv*(Int-EqInt)"

    pdbSetString Silicon Int EquationProc IntDefectBulk
    proc IntDefectBulk {mat sol} {
        set pdbMat [pdbName $mat]
        set Dint 9.32849e-7
        set four_pi 12.566
        set ksi 7.18365e-13
        set kbulk 1.7000e-11
        pdbSetString $pdbMat $sol Equation "ddt($sol)-\
$Dint*EqInt*grad($sol/EqInt)+$kbulk*($sol*Vac-EqInt*EqVac)+$ksi*Csv\
*($sol-EqInt)"
    }
} else {

```

```

    pdbSetString Silicon Cvoid Equation "ddt(Cvoid)-\
$Dvac*($four_pi)*(((1/Isiz)^{(1/3)}*(1.684e-8))+0.25e-7)*Dvoid*(Vac-EqVac)-\
$size1*$ksv*Csv*Vac"
    pdbSetString Silicon Csv Equation "ddt(Csv)-$ksv*Csv*(Vac-\
$eqsv)+$size*$ksv*Csv*Vac"

    pdbSetString Silicon Int EquationProc IntDefectBulk
    proc IntDefectBulk {mat sol} {
    set pdbMat [pdbName $mat]
    set Dint 9.32849e-7
    set four_pi 12.566
    set ksi 7.18365e-13
    set kbulk 1.7000e-11
    pdbSetString $pdbMat $sol Equation "ddt($sol)-\
$Dint*EqInt*grad($sol/EqInt)+$kbulk*($sol*Vac-EqInt*EqVac)"
    }
    }

    pdbSetString Silicon Vac EquationProc VacDefectBulk
    proc VacDefectBulk {mat sol} {
    set pdbMat [pdbName $mat]
    set Dvac 3.4642e-5
    set four_pi 12.566
    set ksv 3.000e-11
    set kbulk 1.7000e-11
    pdbSetString $pdbMat $sol Equation "ddt($sol)-\
$Dvac*EqVac*grad($sol/EqVac)+$kbulk*($sol*Int-\
EqVac*EqInt)+$Dvac*($four_pi)*(((1/Isiz)^{(1/3)}*(1.684e-8))+0.25e-7)*Dvoid*($sol-\
EqVac)+$ksv*Csv*$sol+$ksv*Csv*($sol-EqVac)"
    }

diffuse time=$time_step<s> temp=1060<C> movie = {
set tstep [expr $time-$timeprev($!)]
set tsumstep [expr $tstep+$tsum]
set tsum $tsumstep
set totaltime [expr $prevtotaltime+$tsumstep]

if {($he_val_test == 0) && ($e_he <= 0.01*$e_void)} {
    set he_time $totaltime
    incr he_val_test
}

incr l
set timeprev($!) $time
}

```

```

if {$he_val_test>0 || $terminate_loop==1} {
set p 100
set remain_time [expr {1800-$totaltime}]
}

if {$p<=60} {
set new_time_step [expr 2*$time_step]
set step_check [expr 1800-$totaltime]

if {$step_check>=$new_time_step} {
set time_step $new_time_step
} else {
set time_step $step_check
set last_time_step $step_check
set terminate_loop 1
}
}
set l 0
set timeprev($l) 0

set prevtotaltime $totaltime
set tsum 0
}

set other_loop 1
while {$other_loop<=1 && $terminate_loop==0} {
incr other_loop

pdbSetString Silicon Cvoid Equation "ddt(Cvoid)-\
$Dvac*($four_pi)*(((1/Isiz)^1/3)*(1.684e-8))+0.25e-7)*Dvoid*(Vac-$eqvoid)-\
$size1*$ksv*Csv*Vac+$Dint*($four_pi)*(((1/Isiz)^1/3)*(1.684e-8))+\
0.25e-7)*Dvoid*(Int-EqInt)"
pdbSetString Silicon Csv Equation "ddt(Csv)-$ksv*Csv*(Vac-\
$eqsv)+$size*$ksv*Csv*Vac"

    pdbSetString Silicon Int EquationProc IntDefectBulk
    proc IntDefectBulk {mat sol} {
    set pdbMat [pdbName $mat]
    set Dint 9.32849e-7
    set four_pi 12.566
    set ksi 7.18365e-13
    set kbulk 1.7000e-11
    pdbSetString $pdbMat $sol Equation "ddt($sol)-\
    $Dint*EqInt*grad($sol/EqInt)+$kbulk*($sol*Vac-\

```

```
EqInt*EqVac)+$Dint*($four_pi)*(((1/Isz)^1/3)*(1.684e-8))+0.25e-7)*Dvoid*($sol-\
EqInt)"
}
```

```

pdbSetString Silicon Vac EquationProc VacDefectBulk
proc VacDefectBulk {mat sol} {
  set pdbMat [pdbName $mat]
  set Dvac 3.4642e-5
  set four_pi 12.566
  set eqvoid 5.68424e11
  set ksv 3.000e-11
  set kbulk 1.7000e-11
  pdbSetString $pdbMat $sol Equation "ddt($sol)-\
$Dvac*EqVac*grad($sol/EqVac)+$kbulk*($sol*Int-\
EqVac*EqInt)+$Dvac*($four_pi)*(((1/Isz)^1/3)*(1.684e-8))+0.25e-7)*Dvoid*($sol-\
EqVac)+$ksv*Csv*$sol+$ksv*Csv*($sol-EqVac)"
}
```

```
diffuse time=$remain_time<s> temp=1060<C> movie = {
  set tstep [expr $time-$timeprev($l)]
  set tsumstep [expr $tstep+$tsum]
  set tsum $tsumstep
  set totaltime [expr $prevtotaltime+$tsumstep]
  incr l
  set timeprev($l) $time
}
```

```
set l 0
set timeprev($l) 0
set prevtotaltime $totaltime
set tsum 0
}
sel z=log10(diameter)
plot.1d label=diameter !cle color=green symb=+ max=2
```

```
sel z=log10(Dvoid)
plot.1d label=Dvoid !cle color=black symb=+ max=2
```